INTERPLAY OF ATTRACTIVE INTERACTIONS AND TRAP ANISOTROPY IN BOSE-EINSTEIN CONDENSATES

A DISSERTATION
SUBMITTED TO THE DEPARTMENT OF APPLIED PHYSICS
AND THE COMMITTEE ON GRADUATE STUDIES
OF STANFORD UNIVERSITY
IN PARTIAL FULFILLMENT OF THE REQUIREMENTS
FOR THE DEGREE OF
DOCTOR OF PHILOSOPHY

Nicholas Cizek
August 2010

This dissertation is online at: http://purl.stanford.edu/wk393sg1472

I certify that I have read this dissertation and that, in my opinion, it is fully adequate in scope and quality as a dissertation for the degree of Doctor of Philosophy.

Mark Kasevich, Primary Adviser

I certify that I have read this dissertation and that, in my opinion, it is fully adequate in scope and quality as a dissertation for the degree of Doctor of Philosophy.

David Goldhaber-Gordon

I certify that I have read this dissertation and that, in my opinion, it is fully adequate in scope and quality as a dissertation for the degree of Doctor of Philosophy.

Hideo Mabuchi

Approved for the Stanford University Committee on Graduate Studies.

Patricia J. Gumport, Vice Provost Graduate Education

This signature page was generated electronically upon submission of this dissertation in electronic format. An original signed hard copy of the signature page is on file in University Archives.

Abstract

We evaporatively cool attractively interacting bosonic ^{7}Li in a quasi-one dimensional (quasi-1D) trap to well below the non-interacting particle condensation temperature for our trap but do not observe conventional Bose-Einstein condensation (BEC). Rather than the macroscopic occupation of a single quantum state, for our coldest clouds we observe densities far above the minimum required for quantum degeneracy and widths many times greater than the non-interacting and Gross-Pitaevskii (GP) predictions. We quantify the discrepancies, which together indicate the formation of clouds with multiply macroscopically occupied trap states.

We hypothesize that the specific combination of a quasi-1D anisotropic trap and attractively interacting atoms might provide for many-body states that reside in manifolds of nearly degenerate states, which could inhibit conventional BEC. This idea is probed theoretically using the two-body interaction Hamiltonian to extend the single-mode many-body mean-field GP formalism to allow for atom scattering between two single-particle trap modes. We find that many odd-relative parity energy-adjacent single-particle state pairs exhibit sizable degenerate many-body eigenenergy fractions for atom numbers below the critical atom number at which attraction-induced collapse occurs. The sensitivity to state pair relative parity and our variational width analyses indicate, however, that one and two single-particle state models are ultimately insufficient for these systems.

Mechanism-independent, such bright short coherence length matter-wave sources, analogous to superluminescent diodes, could prove useful in actualizing portable atom-based sensors.

Acknowledgements

Up first, thank you to my advisor, Mark Kasevich. His ability to consider complicated systems and quickly extract the most relevant and important pieces of information, whether regarding a piece of equipment, a measurement of ours, or another researcher's result, is uncanny. His aptitude for asking the hard questions that one is happy later to have answered privately rather than publicly, as well as his guidance in finding solutions, have shaped the entirety of this work. I am fortunate to have had the opportunity to learn from him for six years and I sincerely hope that some of this has rubbed off.

I have had the privilege of having an excellent experimentalist and terrific friend, Mike Minar, as my lab partner almost since I first joined Mark's research group. I have learned and grown considerably working with him in running our experiment and coming to understand our results, while managing to fit in considerable fun as well. Olaf Mandel, the postdoc on our experiment during the first three years of my work on this experiment, Mingchang Liu, the graduate student who handed off the experiment to Mike and I, Daniel Doering, a visiting diploma student, and Patrick Medley, the post-doc who recently joined to take over the experiment, have each contributed insight and effort toward this research. To the remainder of the Kasevich group post-docs, graduate students, and staff members, as well as the Applied Physics Department staff, thank you for six years of helpful answers and camaraderie.

Professors Alexander Fetter and Robert Laughlin have provided generous advice toward developing the theoretical ideas in this thesis, as well as thinking about new ways to understand our experimental data.

The Fannie and John Hertz Foundation provided me with mentoring, stimulating companions, and a generously funded five year fellowship that enabled me to pursue a high risk

and extremely interesting research project.

To all of my friends here at Stanford, thank you for making graduate school a much more enjoyable experience than it otherwise would have been.

To my family, Chuck, Gail, and Sara by birth, and to the Burns family who arrived through marriage, thank you for your guidance and support through the past six years of ups and downs. Lastly, I thank my talented and beautiful wife, Jennifer Burns, for her nurturing, decisiveness, and love.

Contents

List of Figures

Chapter 1

Introduction

1.1 Significance of laboratory Bose-Einstein condensation

The 1995 experimental realization of Bose-Einstein condensation (BEC) in dilute atomic gases [1, 2, 3], for which the Nobel prize was awarded in 2001, was a major achievement in laboratory physics for several distinct reasons. First, at a high level, BEC corresponds to the macroscopic occupation of a quantum mechanical state, in this case a coherent matter-wave. Such matter-wave lasers herald the use of cold atoms in novel high precision sensing applications, paralleling the technology development path of optical lasers. Next, laboratory BEC production validated Satyendra Nath Bose and Albert Einstein's fundamentally grounded BEC prediction, which had remained outstanding for the previous 70 years, following its 1925 publication [4, 5]. Lastly, and perhaps most significantly, it established an experimental beachhead from which considerable further research has proceeded.

1.1.1 Macroscopically occupied quantum states and their applications

The importance of BEC as a macroscopically occupied quantum mechanical state may be appreciated via analogy with three previously discovered examples. The first is superconductivity, in which electrons flow without electrical resistance through certain materials

at temperatures below those materials' corresponding superconducting transition temperatures. The second is superfluidity, in which certain fluids flow without viscosity at temperatures below their corresponding lambda temperatures. The third example, on which this dissertation will draw strong parallels, is the laser beam, in which every photon is indistinguishable with every other: same frequency and phase, same pointing vector, same polarization. It is precisely this property of indistinguishable phase-coherent photons that makes laser beam light more useful than light bulb light, which instead is characterized by a thermal blackbody distribution of frequencies, phases, pointing vectors, and polarizations. In analogy to laser beam photons, atoms in a BEC are similarly indistinguishable and phase-coherent, and can truly be thought of as matter-wave lasers. In all four systems, macroscopic occupation of a quantum mechanical state refers to a significant fraction of the particles identically having the same quantum mechanical description.

Continuing with the laser analogy, just as the first laser applications were in precision measurement, particularly for spectroscopy, the current focus of cold atom technology development, at 15 years old still relatively new, is also primarily for precision measurement. Unlike photons, atoms have mass and magnetic moments, enabling ensembles of identical phase coherent atoms to make superb sensors for observables related to these properties, including accelerometers and gyroscopes for inertial navigation, gravitometers and gravity gradiometers for identifying and characterizing gravitational anomalies, and magnetometers for magnetic field sensing. Expanding on gravity sensing, for example, such functionality has defense applications like detecting underground tunnels, landmines, or improvised explosive devices; homeland security applications such as scanning shipping containers for radioactive materials which often have high density; industrial applications in locating geological formations associated with energy and mineral deposits, e.g. kimberlite pipes for diamond prospecting; and civillian applications like surveying aquifers to monitor water resources, caves for compressed air energy storage, and fault lines for a better understanding of earthquakes. More intriguingly, now 50 years since their initial discovery, laser applications have extended far beyond precision measurement to data storage, telecommunications, manufacturing, and medicine, and it is likely that coherent matter-waves will have similar unanticipated uses 50 years after their discovery.

1.1.2 Validating a fundamental 70 year old prediction

BEC theory for non-interacting particles

More fundamentally, the experimental verification of Bose and Einstein's original prediction of BEC in systems of identical bosons at sufficiently low temperature was crucial because the theoretical bases upon which it stands are extremely elementary. The first is the statistical mechanical postulate of equal a priori probability, that in equilibrium an isolated system is equally likely to reside in any of its accessible states. Application to a small system in contact with a thermal reservoir leads to the Boltzmann distribution, [6] which says that in an ensemble of particles at temperature T, the number of particles occupying state i, with energy E_i, is proportional to its Boltzmann factor:

$$N(E_i) \sim \exp\left(-\frac{E_i}{k_{\mathrm{B}}T}\right). \tag{1.1}$$

Here k_{B} is Boltzmann's constant, and the overall proportionality constant is found by normalizing the sum over all possible states to N_{a}, the total particle number. The second foundation of the BEC prediction is the quantum mechanical idea that identical particles are truly indistinguishable such that the predictions of physical law must remain the same if any two or more such particles are interchanged. In other words, physical law must be invariant under identical particle exchange. Quantum mechanically there are two ways this may occur, corresponding to two types of fundamental particles, bosons and fermions. The focus of this dissertation is bosons, which are symmetric under particle exchange. Fermions, antisymmetric under particle exchange, are not relevant to this work and will not be discussed hereafter. Combining these two disparate ideas, the particle exchange symmetry limits the total number of many-body states available to the ensemble of particles to only those that obey this property, resulting in what are known as Bose-Einstein (BE) statistics [6]. For N_{a} non-interacting particles, BE statistics are completely defined by the equation

$$N(E_i) = \frac{1}{\exp\left(\frac{E_i-\mu}{k_B T}\right) - 1}, \tag{1.2}$$

where μ, the chemical potential, is determined by particle number conservation,

$$\sum_i N(E_i) = N_\mathrm{a}. \tag{1.3}$$

Taken to its logical conclusions, BE statistics predict that there exists a condensation temperature, T_c, below which the single-particle ground state becomes macroscopically occupied. Any cooling below T_c is achieved by further populating this ground state, and the particles macroscopically occupying it are collectively called a Bose-Einstein condensate (BEC). Roughly speaking, T_c is reached when the temperature drops far enough that the phase space density, or number of particles occupying the most-occupied mode,

$$\zeta = \rho_\mathrm{pk}\lambda_\mathrm{dB}^3 \tag{1.4}$$

is $\sim O(1)$. Here

$$\lambda_\mathrm{dB} = \left(\frac{2\pi\hbar^2}{mk_\mathrm{B}T}\right)^{1/2} \tag{1.5}$$

is the thermal de Broglie wavelength, or characteristic quantum mechanical wavepacket size, of particles with mass m at temperature T, $\hbar$ is Planck's constant divided by 2π, and ρ_pk is the peak number density of the boson ensemble. ρ_pk is equivalently the reciprocal of the cube of the interparticle spacing at the densest point in the cloud, so that the T_c phase space density condition can be mapped onto the requirement that, for BEC to occur, the quantum mechanical wavepacket size must be greater than the tightest interparticle spacing so that these particles/wavepackets overlap and become indistinguishable. As a more concrete example, for N_a atoms in a 3D isotropic harmonic potential with trapping frequency ω, the number density at T is given by

$$\rho_\mathrm{pk} = N_\mathrm{a}\left(\frac{m\omega^2}{2\pi k_\mathrm{B}T}\right)^{3/2}. \tag{1.6}$$

Moreover, in such a potential, T_c is given more precisely by $\zeta \approx 2.61$, the value of the

Riemann zeta function evaluated at 3. Putting these together and solving produces

$$T_{\mathrm{c}} \approx \frac{\hbar\omega}{k_{\mathrm{B}}}\left(\frac{N_{\mathrm{a}}}{2.61}\right)^{1/3}, \tag{1.7}$$

so that T_{c} is proportional to the oscillator mode energy splitting expressed as a temperature, $\hbar\omega/k_{\mathrm{B}}$, and depends on the cube root of N_{a}.

BEC theory for interacting particles

Moving beyond noninteracting or single particle systems, the effects of interparticle interactions are typically accounted for with the mean-field Gross-Pitaevskii equation (GPE) [7], expressed in its per particle energy functional form as

$$\frac{E[\phi_0^{\otimes N_{\mathrm{a}}}]}{N_{\mathrm{a}}} = \int \mathrm{d}^3 r \left[\frac{\hbar^2}{2m}|\vec{\nabla}\phi_0|^2 + V_{trap}|\phi_0|^2 + (N_{\mathrm{a}}-1)\frac{1}{2}g_{3\mathrm{D}}|\phi_0|^4\right]. \tag{1.8}$$

Here ϕ_0 is the wavefunction of the BEC. It is normalized so that $\int \mathrm{d}^3 r\,|\phi_0|^2 = 1$, making $\rho(\vec{r}) = N_{\mathrm{a}}\left|\phi_0(\vec{r})\right|^2$ the number density. The first term corresponds to the kinetic energy and is minimized by a smooth uniform ϕ_0. The second term corresponds to the trap potential energy, where V_{trap} is the trap potential energy as a function of position and for BEC experiments is typically a harmonic potential $\sim \omega^2 r^2$. Independent of the specific form of V_{trap}, this term energetically favors ϕ_0 peaked at the minima of V_{trap}. The final term is the interaction energy and has an extra factor of $N_{\mathrm{a}}\left|\phi_0(\vec{r})\right|^2$, making it nonlinear. $g_{3\mathrm{D}} = 4\pi\hbar^2 a/m$ is the 3D interaction coupling coefficient, where a, the particle-particle scattering length, can be positive or negative. When $a, g_{3\mathrm{D}} > 0$ this term is minimized with ϕ_0 uniform and flat, corresponding to repulsive interactions. For $a, g_{3\mathrm{D}} < 0$ this term is minimized when ϕ_0 is tightly localized with a high density in a small volume, corresponding to attractive interactions. In this form, derived from the two-body interaction Hamiltonian in Sec. 3.1.1, the GPE is readily used for predicting properties of interacting particle BECs. Typically this is done by forming a ϕ_0 ansatz with one or more variational parameters, evaluating the integrals to turn the energy functional into an energy function of the variational parameters, then minimizing the energy with respect to these variational parameters; the values of the variational parameters at the energy minimum are the properties predicted for the BEC

wavefunction.

For example, Eq. (1.8) has been used to predict that attractively interacting bosons in a harmonic potential have a critical atom number, N_c, above which the interactions are so strong that the BEC self-collapses. For a 3D isotropic harmonic potential this is given by $N_c = \eta\sigma_0/|a|$ where $\sigma_0 = \sqrt{\hbar/(m\omega)}$ is the characteristic length of the harmonic trap, and $\eta \approx 0.46$ [8, 9, 10]. For a long skinny cigar-shaped quasi-1D harmonic potential with oscillator frequencies given by $\omega_x = \omega_y \equiv \omega_r \gg \omega_z$, as in our experiment,

$$N_c = \eta\frac{\sigma_{r,0}}{|a|} \tag{1.9}$$

where $\sigma_{r,0} = \sqrt{\hbar/(m\omega_r)}$ is specifically the radial oscillator length and $\eta = 3^{-1/4} \approx 0.78$ [10]. These predictions have been confirmed experimentally in both 3D and quasi-1D cases [11, 12, 13]. For the experiments comprising the first half of this thesis, $N_c \approx 330$. For the theory in the second half of this thesis, performed with a slightly different ω_r as explained in Sec. 2.1.1, $N_c \approx 360$.

Because BE statistics are so fundamentally predicated, on statistical mechanics and symmetry under particle exchange, the process of condensation is inherently robust. One cools bosonic atoms, typically in a magneto-optical trap and then evaporatively, to $T \gtrsim T_c$, with classical thermal Maxwell-Boltzmann single-mode gaussian distributions adequately describing the density profiles. For $T < T_c$ these single mode fits to the density profiles are no longer adequate and bimodal distributions of the thermal cloud plus the BEC must be used. Further cooling is marked by the condensate mode increasing in size while the thermal background continues shrinking. Interactions have historically been well accounted for by the GPE, which predicts changes in the BEC size depending on the interaction strength and sign, but no changes in whether or not BEC occurs, nor dramatic changes in the value of T_c. This holds for cooling repulsively interacting atoms in 3D and quasi-1D isotropic harmonic potentials into BECs, as shown visually in Fig. 1.1(a), and also for then flipping the interactions of the already quantum degenerate atoms to attractive using a Feshbach resonance [11, 12, 13]. Even in the case of an attractively interacting BEC in a 3D harmonic potential at N_a just below N_c, the BEC compresses, but the fact that it forms at $T \lesssim T_c$, and grows to no larger than $N_a < N_c$ without collapsing, remains true [3].

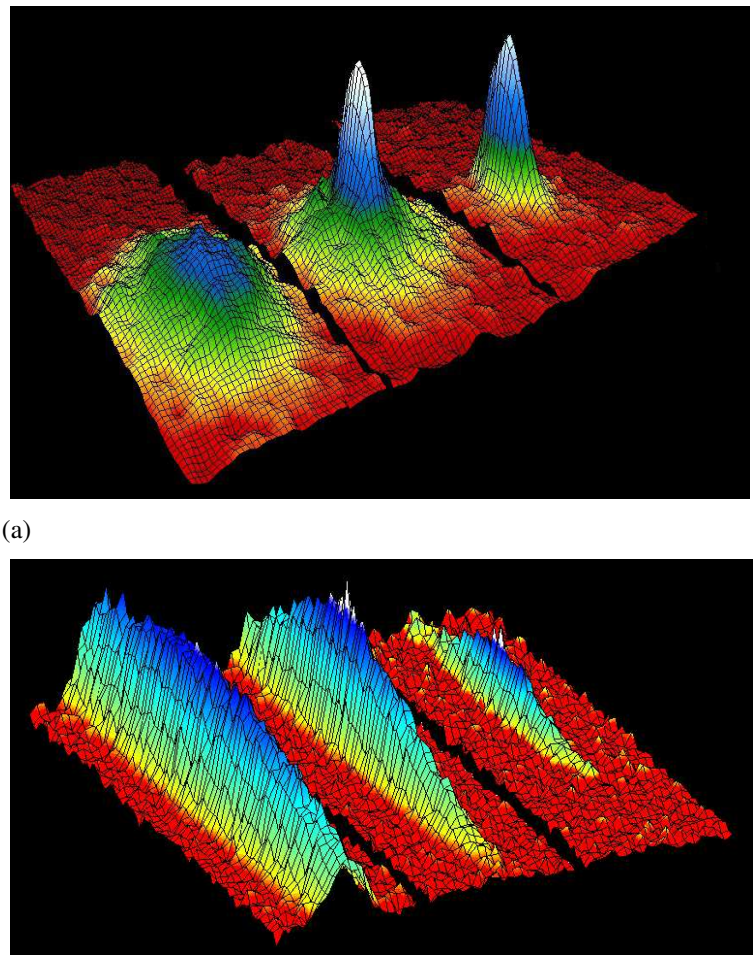

(a)

(b)

Figure 1.1: Surface plots comparing (a) conventional and (b) frustrated BEC. In each image set the left atom cloud is above, the center just below, and the right well below T_c. The (x, y) positions in each image represent pixels in a 2D CCD array. The height and color at each pixel represent the atom absorption. (a) ^{87}Rb, repulsive, undergoing conventional BEC in an isotropic trap. Above T_c (left) the density has a single gaussian thermal mode. Just under T_c (center) atoms begin macroscopically occupying the ground state, appearing as the second mode centered on top of the thermal atoms. Cooling below T_c (right) occurs by further populating the ground state. Photo Credit: Mike Matthews [1]. (b) ^{7}Li, attractive, undergoing frustrated BEC in a quasi-1D trap. Unlike (a), the color map here transitions from blue to white at the top of the best fit thermal cloud, making the white indicate BEC. Like in (a), above T_c (left) the cloud density is a single gaussian thermal mode, though cigar-shaped because of the trap. At T_c (center) BEC initiates as predicted, appearing in white on top of the thermal gaussian. Not predicted, however, cooling well below T_c (right) depletes the thermal background without increasing the size of the just visible BEC.

The theoretical groundedness and historical agreement between BEC theory and experiment make our result, directly cooling attractively interacting bosons in a quasi-1D harmonic potential well below T_c and observing the onset of BEC followed instead by its subsequent frustration, shown in Fig. 1.1(b), novel. To a cold atom physicist, this is like putting water in a round ice cube tray and then in the freezer, cooling it below 0° C, and seeing it form ice, then putting the same water in a long skinny ice cube tray and back in the freezer, again cooling it below 0° C, and seeing it not form ice but some other phase of matter, say clumping up into slushy beads. As discussed briefly below, quantified in Sec. 2.3.3, and investigated at length theoretically in Ch. 3, we believe it is the specific combination of an anisotropic quasi-1D trap potential and attractive interactions that causes this.

1.1.3 Establishing an experimental beachhead

Finally, the 1995 discovery of BEC in dilute atomic gases has proved important because it firmly established that creating coherent matter-waves in the laboratory is possible. This experimental beachhead has opened the door to hundreds of promising avenues of research, and this dissertation is about the one of these hundreds that we have taken.

1.2 Our work: quasi-1D anisotropic trap and attractive interactions

With the existence proof of laboratory BECs completed, the relevant research questions become, "What can one use BECs for?" and, "How can one make BECs more easily?" Answering these has led to two differences separating our work from the Nobel prize winning 1995 BEC research. In terms of application, the overarching focus of our research group is demonstrating the use of cold atom precision sensors and improving their precision. To explore the range of possibility, our experiments aim toward observing macroscopic tunneling events of the sort that might lead to NOON state atom interferometry and its associated N_a^1 scaling in signal to noise ratio compared to the $N_a^{1/2}$ scaling for ensemble single-particle interferometry [14]. Two properties of ^{7}Li assist in this, which is why we follow the lead of [3] in using it. The low mass increases the probability that tunneling will occur, and the

attractive interactions of the $|2S_{1/2}, F = 2, m_F = +2>$ state increase the probability that such tunneling could be macroscopic, e.g. the entire cloud reflecting from or transmitting through a barrier collectively. Attractive interactions have the additional benefit of potentially enabling extended interrogation time interferometry because such atom clouds do not disperse like repulsively or non-interacting clouds. However, both of these properties negatively impact imaging, the lower mass by reducing the average number of photons scattered by each atom by $3 - 10\times$ before Doppler shifting out of resonance with the imaging light, and the attractive interactions because the associated N_c is two or more orders of magnitude smaller than the N_a achievable in BECs of repulsively interacting atoms [1, 2].

A natural path to achieving easier BEC is to raise T_c so that one does not have to cool as low to observe quantum phenomena. This is done with tighter harmonic traps, having higher ω, as in Eg. 1.7. However it is technically difficult to achieve tight confinement in all three dimensions and have sufficient optical access to enable imaging, so a reasonable compromise that allows imaging optical access is to have two tightly confining dimensions and a third loosely confining dimension. This produces a long, skinny, cigar-shaped trap, which in our case has $\omega_r = 2\pi \times 3.5\,\mathrm{kHz}$ and $\omega_z = 2\pi \times 50\,\mathrm{Hz}$.

We believe it is the unique combination of attractive interactions and a quasi-1D trapping potential that enables the novel frustration of conventional BEC formation in our apparatus. Instead the clouds we produce appear to have multiple macroscopically occupied modes which indicates a reduced coherence length from that of a pure BEC. Returning to the laser analogy, these matter-waves have coherence properties akin to the optical waves produced by superluminescent diodes (SLDs). Moreover, as commercial atom interferometers become more feasible, such matter-wave sources may similarly offer signal to noise ratio benefits over thermal or pure BEC sources.

1.3 Organization of this thesis

The following is a brief description of the organization of this thesis. Ch. 2, Experiment, explains the experiment we have performed: cooling a cloud of attractively interacting ^{7}Li in a quasi-1D harmonic potential to quantum degeneracy, $T < T_c$, but not observing conventional BEC as predicted by BE statistics and the GPE. The data collection was performed

in collaboration with Michael Minar, Olaf Mandel, Mingchang Liu, and Mark Kasevich, and additionally exists as a manuscript we are preparing for submission. Ch. 3, Theory, describes the theoretical work Michael Minar, Mark Kasevich, and I have performed seeking to understand why BE statistics and the GPE fail to predict frustrated condensation in our system. It too exists as a manuscript we are preparing for submission. Ch. 4, Outlook, discusses the outlook for our experimental campaign toward observing macroscopic tunneling and ultimately harnessing it in advanced metrology applications. Ch. 5, Conclusion, formally summarizes our results. Appendix A derives the correction to the evaporation radio frequency due to gravitational sag. Appendix B is an internally used document written to clarify and record our image processing procedure at the time the data in Ch. 2 was taken.

Chapter 2

Experiment

We report our results for evaporatively cooling ^{7}Li in an anisotropic quasi-1D magnetic trap in the attractively interacting $\left|2S_{1/2}, F = 2, m_F = +2\right\rangle$ state, where $a = -27.6a_0$ and a_0 is the Bohr radius [15]. Notably, when evaporating directly under attractive interactions we are unable to produce the known Gross-Pitaevskii (GP) ground state, a single localized quantum soliton [10]. Rather, we create non-traditional Bose-Einstein condensates (BECs), with phase space densities (PSDs) well above the minimum required for quantum degeneracy but having axial spatial widths significantly greater than those of single solitons or even of BECs of non-interacting particles. Together these indicate that our coldest clouds have $N_{\mathrm{m}} = 14 \pm 4$ macroscopically occupied trap modes.

2.1 Procedure

The experimental apparatus for producing our quantum degenerate gas has been described in detail previously [16]. After loading $N_{\mathrm{a}} \approx 10^9$ atoms into a magneto-optical trap, the atoms are optically pumped into the $\left|2S_{1/2}, F = 2, m_F = +2\right\rangle$ trap state, loaded into a magnetic quadrupole trap, and transported into a final cigar-shaped Ioffe-Pritchard (IP) trap.

2.1.1 Magnetic trap: radial trapping frequency calculation

We use a higher IP bias coil current than in Ref. [16], increasing ω_r above its $2\pi \times 3\,\mathrm{kHz}$ value, and additionally use a more precise value of the ^{7}Li hyperfine splitting RF frequency, $\nu_{\mathrm{HFS}} = 803.534 \pm 0.077\,\mathrm{MHz}$ [17]. The associated change in the minimum magnetic field $B_0 = 0.4\,\mathrm{G}$, to $B_0 = 0.38\,\mathrm{G}$, is below their reported precision. Because

$$\frac{\partial^2 B}{\partial r^2} = \frac{1}{B_0}\left(\frac{\partial B}{\partial r}\right)^2 - \frac{1}{2}\frac{\partial^2 B}{\partial z^2}, \tag{2.1}$$

where

$$\begin{aligned} \frac{\partial^2 B}{\partial r^2} &= \frac{m\omega_r^2}{m_{\mathrm{f}} g_{\mathrm{f}} \mu_{\mathrm{B}}} \\ \frac{\partial^2 B}{\partial z^2} &= \frac{m\omega_z^2}{m_{\mathrm{f}} g_{\mathrm{f}} \mu_{\mathrm{B}}} \end{aligned} \tag{2.2}$$

are the magnetic field radial and axial curvatures [18], known from parametric heating measurements of ω_r and ω_z, $\partial B/\partial r$ is the magnetic field radial gradient, $m_{\mathrm{f}} = 2$ and $g_{\mathrm{f}} = 1/2$ are, respectively, the magnetic sublevel and Lande g-factor of our trap state, and μ_{B} is the Bohr magneton, this correspondingly changes their quoted $\partial B/\partial r = 420\,\mathrm{G/cm}$ to $\partial B/\partial r = 414\,\mathrm{G/cm}$.

The resonance condition for evaporating atoms via spin flips at magnetic field B occurs when the evaporation radio frequency (RF) ν satisfies

$$\mu_{\mathrm{B}} B \left(m_{\mathrm{f}} g_{\mathrm{f}} - m'_{\mathrm{f}} g'_{\mathrm{f}}\right) = h\left(\nu - \nu_{\mathrm{HFS}}\right), \tag{2.3}$$

where $h = 2\pi\hbar$ is Planck's constant, and $m'_{\mathrm{f}} = -1$ and $g'_{\mathrm{f}} = -1/2$ are, respectively, the magnetic sublevel and Lande g-factor of the anti-trapped $\left|2S_{1/2}, F = 1, m_F = +1\right\rangle$ state that the atoms are pumped into from the trap state. B_0, and the minimum evaporation RF, ν_0, occur at the trap center, and we use our measured $\nu_0 = 804.12\,\mathrm{MHz}$ with Eq. (2.3) to determine that the magnetic field in the trap center is $B_0 = 0.28\,\mathrm{G}$.

To leading order, ω_z and $\partial B/\partial r$ are independent of IP bias coil current, which fixes $\partial^2 B/\partial z^2$ via Eq. (2.2). With this, the slightly corrected $\partial B/\partial r$, and B_0, we determine

$\partial^2 B/\partial r^2$ using Eq. (2.1). Finally, using Eq. (2.2), we determine that, at our increased IP bias coil current, the final magnetic trap has tightened radially to $\omega_r = 2\pi \times 3.5\,\mathrm{kHz}$, with a corresponding aspect ratio increase to $\omega_r/\omega_z = 70$.

2.1.2 Evaporative cooling: effective RF correction for gravitational sag

In this trap, 32 s sequences of forced RF evaporative cooling ending as little as 14 kHz above ν_0, after correcting for gravitational sag, produce atom clouds with around 800 atoms and temperatures around 50 nK. Because our quasi-1D trap is oriented with the long, loosely confining dimension vertical, correcting for gravitational sag is significantly more important than if we had tight vertical confinement. The gravity corrected effective differential RF, $\Delta\nu_{\mathrm{eff}} = \nu_{\mathrm{eff}} - \nu_0$, as a function of the set differential RF, $\Delta\nu_{\mathrm{set}} = \nu_{\mathrm{set}} - \nu_0$, is given by

$$\Delta\nu_{\mathrm{eff}} = \left(\sqrt{\Delta\nu_{\mathrm{set}} + \Delta\nu_{\mathrm{g}}} - \sqrt{\Delta\nu_{\mathrm{g}}} \right)^2, \tag{2.4}$$

where

$$\Delta\nu_{\mathrm{g}} = \frac{mg^2 \left(m_{\mathrm{f}} g_{\mathrm{f}} - m'_{\mathrm{f}} g'_{\mathrm{f}} \right)}{2h\omega_z^2} \tag{2.5}$$

is the change in B at the trap center caused by gravitational sag, expressed as a frequency according to Eq. (2.3), and g is the acceleration due to gravity. For our trap parameters, $\Delta\nu_{\mathrm{g}} = 12.8\,\mathrm{kHz}$. Because I could not find it published anywhere, the derivation of this formula is in Appendix A. Throughout this dissertation, stated and plotted values of ν_{f}, the final RF frequency in an evaporation sequence, and ν relative to ν_0 in general, have already been corrected for gravitational sag.

2.1.3 Imaging

At the conclusion of evaporation the clouds are prepared for imaging. An additional DC homogeneous magnetic field parallel to the imaging axis is enabled to preserve the spin polarization of the sample in the absence of the magnetic trap. Then the trapping potential is switched off and the atomic cloud ballistically expands for a brief time-of-flight (TOF)

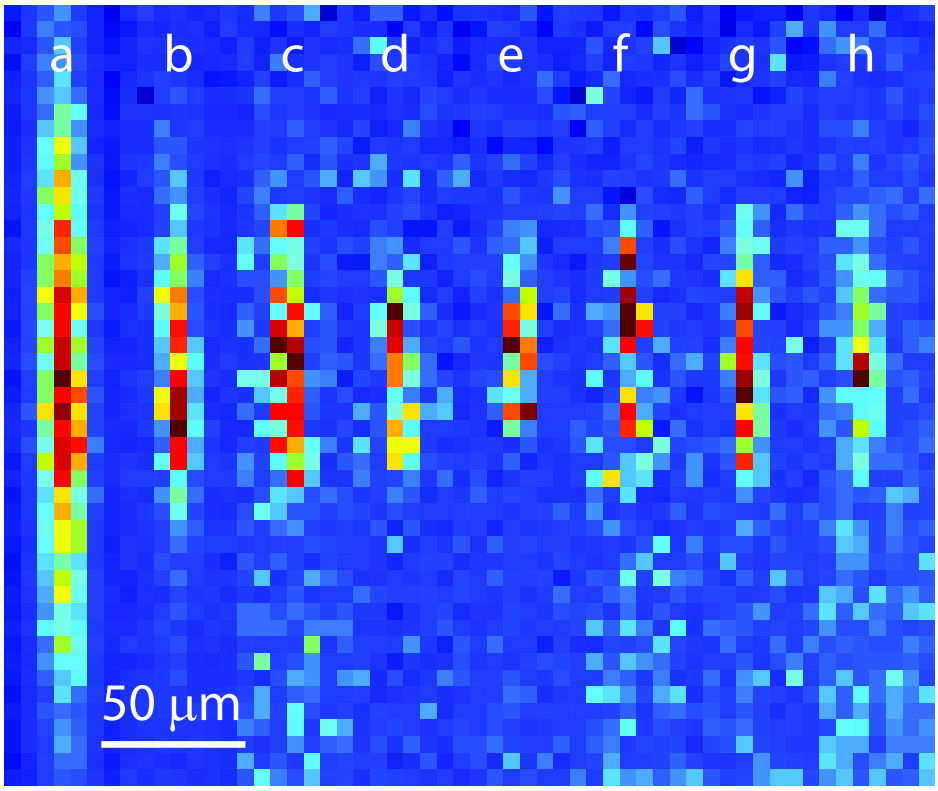

Figure 2.1: False color absorption images of evaporatively cooled ^{7}Li at various points in the forced RF evaporation sequence. The final RF evaporation frequency, ν_f, in each image is: (a) ν_0 + 183 kHz, (b) ν_0 + 30 kHz, (c) ν_0 + 19 kHz, (d-h) ν_0 + 14 kHz. Several images at the lowest RF are included to demonstrate the variation in final density distributions. The corresponding atom numbers are (a) 30300, (b) 4100, (c) 1500, (d) 1000, (e) 800, (f) 1000, (g) 1300, (h) 1300. 5.8 μm pixel size.

of t_{TOF} = 200 μs before it is illuminated with a 20 μs pulse of resonant, circularly polarized light. The atomic density distribution imprints an absorption profile onto this beam, which then is imaged with a magnification of $\approx$ 2.8 onto a CCD camera with 16 μm pixel size, producing pictures with a spatial resolution of 5.8 μm. Example absorption images at different points in the RF evaporation sequence are shown in Fig. 2.1.

2.2 Observables

2.2.1 Image analysis: extracting the peak OD, and axial and radial widths after free expansion

For each atomic cloud, we extract the relevant experimental data from its absorption image, $\mathcal{A}(x_i, z_j)$, where x_i and z_j label the horizontal (radial) and vertical (axial) pixel positions in the 2D array comprising our CCD camera. We we convert to optical depth, $O(x_i, z_j) = \alpha_0 \mathcal{A}(x_i, z_j)$, using the atom-light interaction cross section,

$$\alpha_0 = f_\mathrm{p} \frac{3\lambda^2}{2\pi}, \tag{2.6}$$

where $\lambda = 670.97\,\mathrm{nm}$ [19] is the atomic transition wavelength and $f_\mathrm{p} = 0.7$ is a dimensionless constant determined from the steady state solution of the population distribution of atoms amongst the ground state hyperfine levels for the light field polarization, detuning, and intensity, and DC magnetic field strength during imaging. For example, if all the atoms begin in the imaging cycling transition ground state and the imaging light is perfectly resonant and polarized then $f_\mathrm{p} = 1$, unpolarized resonant light would have $f_\mathrm{p} = 1/3$ [18, 20].

In absence of a density profile model that better includes attractive atom-atom correlations, the atom cloud density profiles are fitted to the form

$$\rho(x, y, z) = \frac{N_\mathrm{a}}{\pi^{3/2}\sigma_x\sigma_y\sigma_z} \exp\left(-\frac{(x-x_c)^2}{\sigma_x^2} - \frac{(y-y_c)^2}{\sigma_y^2} - \frac{(z-z_c)^2}{\sigma_z^2}\right), \tag{2.7}$$

where $\sigma_x = \sigma_y = \sigma_r$ is the radial cloud e^{-1} density radius, σ_z is the axial cloud e^{-1} radius, and (x_c, y_c, z_c) is the cloud center. Imaging projects this distribution along one of the radial dimensions to produce a 2D absorption density profile,

$$\mathcal{A}(x, z) = \mathcal{A}_\mathrm{pk} \exp\left(-\frac{(x-x_c)^2}{\sigma_r^2} - \frac{(z-z_c)^2}{\sigma_z^2}\right), \tag{2.8}$$

which has a corresponding $\mathcal{O}$ profile,

$$\mathcal{O}(x,z) = \mathcal{O}_{\rm pk} \exp\left(-\frac{(x-x_c)^2}{\sigma_r^2} - \frac{(z-z_c)^2}{\sigma_z^2}\right), \tag{2.9}$$

where $\mathcal{O}_{\rm pk}$ and $\mathcal{A}_{\rm pk}$, the peak $\mathcal{O}$ and $\mathcal{A}$, respectively, are found by evaluating the integrals in Eqs. (2.7,2.8,2.9):

$$\mathcal{O}_{\rm pk} = \alpha_0 \mathcal{A}_{\rm pk} = \alpha_0 N_{\rm a}/(\pi\sigma_r\sigma_z). \tag{2.10}$$

We specifically extract $\mathcal{O}_{\rm pk}$ and $\sigma_{z,TOF}$ from the central axial cross section, labeled by x_{ic}, by minimizing the discrepancy between $\mathcal{O}(x_{ic}, z_j)$ and $\mathcal{O}(x,z)$ at those points using a least squares fit. We find $\sigma_{r,TOF}$ by fitting the average of all central rows, $\mathcal{O}(x_i, z_{jc+u})$, whose integrated atom signal is $> 10\%$ of that for $\mathcal{O}(x_i, z_{jc})$, where u spans ± 10. This is necessary because in each single radial cross section there are too few pixels with atom signal well above the noise floor to yield highly repeatable results. Technically speaking, the absorption images include a background offset and slope which we calculate and subtract off during fitting. To estimate the systematic errors associated with our fitting algorithm, we fit a subset of the clouds with true 2D Gaussians having 9 free parameters including slopes offset and clocking and found that on average this produces $\mathcal{O}_{\rm pk}$ values $10 \pm 20\%$ greater and $\sigma_{z,TOF}$ values $3 \pm 6\%$ greater, while leaving $\sigma_{r,TOF}$ systematically unchanged at $0 \pm 4\%$, where the uncertainties here are standard deviations. These systematic errors are too small to substantively affect the essential physics of the result we are reporting. Appendix B, written for internal documentation and use, describes the image processing from the raw absorption images through the fitting algorithm to the $N_{\rm a}$ calculation in much greater detail.

2.2.2 Atom number, and in-trap axial and radial widths

Directly from these fitted values and Eq. (2.10) we calculate the total number of atoms,

$$N_{\rm a} = \frac{\mathcal{O}_{\rm pk}}{\alpha_0} \pi \sigma_{r,TOF} \sigma_{z,TOF}. \tag{2.11}$$

When comparing this quantity to the sum over pixels of the atom numbers corresponding to the absorption at each pixel, we find that they agree within measurement uncertainty.

We calculate the *in-situ* axial and radial cloud widths immediately prior to release from the trap, σ_z and σ_r, respectively, from the widths measured after ballistic expansion, using the measured ballistic expansion time, t_{TOF}, and the measured imaging system point spread function (PSF) e^{-1} radius, $\sigma_m athrmPSF$,

$$\sigma_i = \sqrt{\frac{\sigma_{i,TOF}^2 - \sigma_m athrmPSF^2}{1 + \omega_i^2 t_{\mathrm{TOF}}^2}} \tag{2.12}$$

where $i \in \{r, z\}$. t_{TOF} and $\sigma_m athrmPSF$ in turn are determined as the values that simultaneously produce the correct *in-situ* aspect ratio for the hottest clouds, $\omega_r/\omega_z = 70$, and correct *in-situ* radial width for the coldest clouds, $\sigma_r = \sigma_{r,0}$, where $\sigma_{i,0} = \sqrt{\hbar/(m\omega_i)}$ is the characteristic length for oscillator $i \in \{r, z\}$ and m is the mass of ^{7}Li. More concretely, for the hot cloud constraint, we average all of the $\nu_{\mathrm{f}} = \nu_0 + 347\,\mathrm{kHz}$ cloud $\sigma_{r,TOF}$ and $\sigma_{z,TOF}$ values, then calculate both *in-situ* widths and take their ratio to get the hot cloud *in-situ* aspect ratio as a function of t_{TOF} and $\sigma_m athrmPSF$. For the cold cloud constraint, we average all of the $\nu_{\mathrm{f}} = \nu_0 + 14\,\mathrm{kHz}$ cloud $\sigma_{r,TOF}$ values, then calculate the *in-situ* radial width as a function of t_{TOF} and $\sigma_m athrmPSF$. Simultaneously solving these two equations we get $t_{\mathrm{TOF}} = 208\,\mu\mathrm{s}$ and $\sigma_m athrmPSF = 4.8 \pm 0.5\,\mu\mathrm{m}$. t_{TOF} measured this way should equal the set time of ballistic expansion, $200\,\mu\mathrm{s}$, plus one half of the $20\,\mu\mathrm{s}$ imaging time, minus the time it takes for the magnetic trap to ring down, placing the observed value in good agreement. Our first principles calculation of the imaging system $\sigma_m athrmPSF$, done by convolving the lens system Airy function PSF with the pixel rectangular PSF, is within a factor of two of the measurement, with the difference probably due to using non-diffraction limited imaging optics in our experiment.

2.2.3 Peak density, non-interacting, interacting, and total energy per particle

From the atom number, *in-situ* axial and radial widths, final evaporation RF values, and trapping frequencies, we derive all remaining experimental observables of interest. We calculate the non-interacting energy per particle by summing the per particle mean kinetic

and trap potential energies,

$$\begin{aligned}\mu_0 &= \frac{1}{2}m\left(2\omega_r^2\sigma_r^2 + \omega_z^2\sigma_z^2\right) \\ &= \frac{3}{2}m\omega_z^2\sigma_z^2, \end{aligned} \tag{2.13}$$

where the second equality holds for clouds in thermal equilibrium. The *in-situ* peak number density,

$$\rho_{\rm pk} = \rho(0,0,0) = \frac{N_{\rm a}}{\pi^{3/2}\sigma_r^2\sigma_z}, \tag{2.14}$$

Eq. (2.7), is used to calculate the peak interaction energy per particle,

$$\begin{aligned}|\mu_{\rm int}| &= \frac{1}{2}|g_{\rm 3D}|g^{(2)}(0)\rho_{\rm pk} \\ &= \frac{1}{2}\frac{4\pi\hbar^2|a|}{m}g^{(2)}(0)\rho_{\rm pk} \\ &= \frac{2g^{(2)}(0)\hbar^2 N_{\rm a}|a|}{\pi^{1/2}m\sigma_r^2\sigma_z}, \end{aligned} \tag{2.15}$$

where $g_{\rm 3D} = 4\pi\hbar^2 a/m$ is the 3D interaction coupling coefficient and $g^{(2)}(0)$ is the two-body correlation function evaluated at zero separation. We use $g^{(2)}(0) = 2$, the value for a thermal cloud, for evaluating $|\mu_{\rm int}|$ for our data points, which we believe are not in a pure state. However, we use $g^{(2)}(0) = 1$, the value for a pure state, [21, 22] in evaluating the quasi-1D collapse criterion [10] recast in terms of energy, $|\mu_{\rm int}| < |\mu_{\rm int,c}|$ where

$$\begin{aligned}\frac{|\mu_{\rm int,c}|}{\hbar\omega_r} &\equiv \frac{2g^{(2)}(0)\hbar N_{\rm c}|a|}{\pi^{1/2}m\omega_r\sigma_r^2\sigma_z} \\ &= \frac{2g^{(2)}(0)}{\pi^{1/2}}\frac{\sigma_{r,0}^3}{\sigma_r^2\sigma_z}\frac{N_{\rm a}|a|}{\sigma_{r,0}} \\ &\approx 1.95, \end{aligned} \tag{2.16}$$

because this theory applies to a singly occupied orbital. The approximate equality in Eq. (2.16) comes from the quasi-1D system stability criteria [10], $N_{\rm a}|a|/\sigma_{r,0} < 3^{-1/4}$, Eq. (1.9), and simultaneously $\sigma_z/\sigma_{r,0}, \sigma_r/\sigma_{r,0} > 3^{-1/4}$. The average total energy per particle

for $a < 0$ is

$$\mu_{\text{tot}} = \mu_0 + \frac{1}{2}|\mu_{\text{int}}|2^{-3/2}, \tag{2.17}$$

where the $+1/2$ leading $|\mu_{\text{int}}|$ is a consequence of the virial theorem [23] and the $2^{-3/2}$ converts from peak to average interaction energy per particle in 3D, according to the assumed gaussian density distribution.

When $\sigma_{r,TOF} \sim \sigma_m athrm PS F$, small measurement variations make the σ_r calculations noisy, making it potentially helpful to decompose these per particle energies into axial-only versions that are independent of σ_r. The axial-only non-interacting energy per particle is

$$\mu_{0,\text{z}} = \frac{1}{2}m\omega_z^2\sigma_z^2. \tag{2.18}$$

The axial linear peak density is

$$\rho_{\text{pk,z}} = \frac{N_{\text{a}}}{\pi^{1/2}\sigma_z}, \tag{2.19}$$

making the axial-only peak interaction energy per particle,

$$\begin{aligned} |\mu_{\text{int,z}}| &= \frac{1}{2}|g_{1\text{D}}|g^{(2)}(0)\rho_{\text{pk,z}} \\ &= \frac{g^{(2)}(0)\hbar\omega_r N_{\text{a}}|a|}{\pi^{1/2}\sigma_z}, \end{aligned} \tag{2.20}$$

where $g_{1\text{D}} = 2\hbar\omega_r|a|$ is the quasi-1D interaction coupling coefficient. The axial-only total energy per particle, for $a < 0$, is

$$\mu_{\text{tot,z}} = \mu_{0,\text{z}} - \frac{1}{2}|\mu_{\text{int,z}}|2^{-1/2}, \tag{2.21}$$

where the $-1/2$ is from the virial theorem applied to the axial dimension only [23] and the $2^{-1/2}$ converts from peak to average interaction energy per particle in 1D, according to the assumed gaussian density distribution.

2.2.4 Temperature

Paired with N_{a} the other most important observable in BEC experiments is temperature, T. For an interactionless ideal gas in a 3D harmonic potential this is extracted from $\mu_{\text{tot}} = \mu_0$

using

$$k_{\mathrm{B}}\tilde{T} = \frac{\mu_0}{3} = \frac{m\omega_z^2\sigma_z^2}{2}, \tag{2.22}$$

or alternatively,

$$k_{\mathrm{B}}\tilde{T}_{\mathrm{z}} = \mu_{0,\mathrm{z}} = \frac{m\omega_z^2\sigma_z^2}{2}, \tag{2.23}$$

where the tilde is used to indicate that these formulae pertain explicitly to non-interacting particles, $a = 0$. This tilde convention will be conserved throughout this dissertation to refer to measurements and formulae that pertain explicitly to non-interacting particles.

Because we lack a theoretical model for the density of states for attractively interacting particles, strictly speaking, we cannot calculate the true cloud T from μ_{tot} in this way when the interactions become significant, $|\mu_{\mathrm{int}}| \gtrsim \mu_0$. One approach for including interactions is to use

$$\begin{aligned} k_{\mathrm{B}}T_{\mathrm{GP}} = \frac{\mu_{\mathrm{tot}}}{3} &= \frac{m\omega_z^2\sigma_z^2}{2} + \frac{\hbar^2 N_{\mathrm{a}}|a|}{3\pi^{1/2}2^{3/2}m\sigma_r^2\sigma_z} \\ k_{\mathrm{B}}T_{\mathrm{GP,z}} = \mu_{\mathrm{tot,z}} &= \frac{m\omega_z^2\sigma_z^2}{2} - \frac{\hbar\omega_r N_{\mathrm{a}}|a|}{2^{3/2}\pi^{1/2}\sigma_z}, \end{aligned} \tag{2.24}$$

the GP-equivalent 3D and 1D temperature proxies, respectively, [23] which include the interaction energy in a mean-field sense, where we have used the pure state value $g^{(2)}(0) = 1$. However, because we suspect that $1 < g^{(2)}(0) < 2$ but do not know the precise value, Sec. 2.2.3, for simplicity in this dissertation we will use $\tilde{T}$, the $a = 0$ non-interacting particle temperature, as the temperature proxy. Similarly, as figures of merit for degeneracy we use the PSD, Eq. (1.4), explicitly defined for non-interacting particles, $a = 0$,

$$\tilde{\zeta} = \rho_{\mathrm{pk}}\tilde{\lambda_{\mathrm{dB}}}^3, \tag{2.25}$$

and the fractional non-interacting PSD, $\tilde{\zeta}/N_{\mathrm{a}}$, where $\tilde{\lambda_{\mathrm{dB}}} = \sqrt{\frac{2\pi\hbar^2}{mk_{\mathrm{B}}\tilde{T}}}$ is the thermal de Broglie wavelength, Eq. (1.5), explicitly defined for non-interacting particles.

2.3 Results

2.3.1 Experiment probes well into the BEC regime

These data indicate our evaporation sequences consistently produce clouds whose atom numbers and temperatures place them in the regime where condensation is predicted by standard BEC theory [24]; however the behavior of our attractively interacting particle clouds differs dramatically. Shown visually in Fig. 1.1, this gets quantified in Fig. 2.2, where cloud N_a and $\tilde{T}$ are plotted; the dotted and dashed lines demarcate the 3D and 1D condensation thresholds, respectively, predicted for finite numbered non-interacting particles confined at our trapping frequencies. With sufficient evaporation we reliably form clouds with $\tilde{T}$ below the condensation temperature criterion for a given N_a. Correspondingly, as the 3D condensation threshold is crossed $\tilde{\zeta}$ rises from 1.2 ± 0.1 at $\nu_f = \nu_0 + 183\,\mathrm{kHz}$ (□), to 4.3 ± 0.5 at $\nu_f = \nu_0 + 106\,\mathrm{kHz}$ (▲), and goes above 10 for $k_B\tilde{T} < 100\hbar\omega_z$, indicating that BEC formation has initiated.

However the conventional BEC formation process, whereby any cooling after its onset is achieved by increasing the number of atoms in the single-particle ground state, appears to quench: the normalized axial width data (top axis) manifestly reveals that multiple trap modes must be occupied. Specifically, the σ_z decrease toward but almost exclusively stay above $\sigma_{z,0}$. In fact at the lowest $\nu_f = \nu_0 + 14\,\mathrm{kHz}$ (○), the average axial width is $\sigma_z/\sigma_{z,0} = 6.0 \pm 0.6$. The combination of these large widths with the $\tilde{\zeta}$ data immediately below $\tilde{T}_c$ indicating quantum degeneracy directly lead to our conclusion that we produce atomic ensembles exhibiting macroscopic occupation of multiple trap modes.

The validity of the temperature measurements at this point is also established in Fig. 2.2(a). The dash-dotted line marks $k_B\tilde{T} = |\mu_{int,c}|$, where the non-interacting per particle energy is the same energy as the maximum attainable interaction energy per particle in our trap, which a cloud could attain only if its entirety verged on collapse. This places an upper bound on when $T = \tilde{T}$ might break down. For $k_B\tilde{T} \gg |\mu_{int,c}|$, $T = \tilde{T}$ is certainly well-defined, and for $k_B\tilde{T} \gtrsim |\mu_{int,c}|$, it should remain valid because typically only a few positions in the cloud have density high enough for $|\mu_{int}| \approx |\mu_{int,c}|$, where it applies only locally to those particular density fluctuations, leaving the remainder of the cloud with $k_B\tilde{T} \gg |\mu_{int,c}|$.

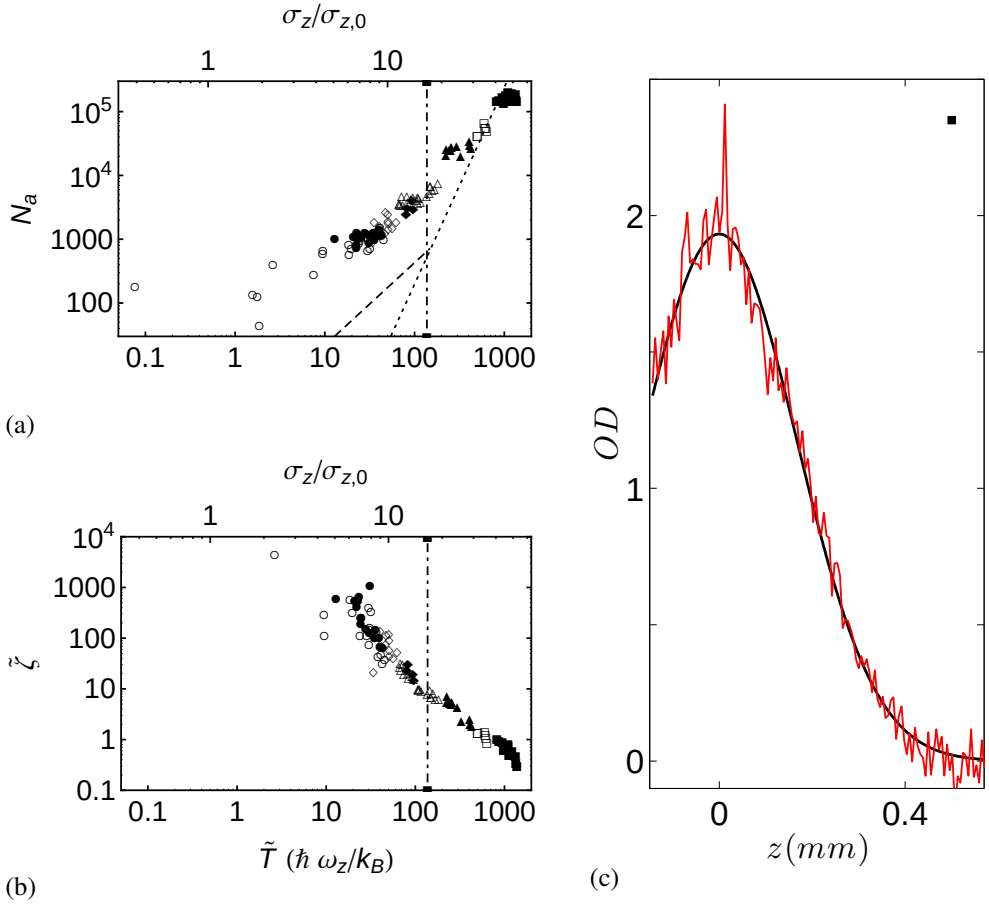

Figure 2.2: (a) Atom number, N_a, as a function of non-interacting particle temperature, $\tilde{T}$, compared with the BEC transition temperatures, $\tilde{T}_c$, for the 3D (dashed line) and 1D (dotted line) regimes, and $k_B\tilde{T} \equiv |\mu_{int,c}|$ (dash-dotted line), which places an upper bound on where $T = \tilde{T}$ becomes a poor approximation. (b) PSD as a function of non-interacting particle temperature, compared with $k_B\tilde{T} \equiv |\mu_{int,c}|$ (dash-dotted line). During evaporative cooling, a typical atom cloud progresses from the upper right to the lower left as distinguished by the symbols encoding the data points' final RF evaporation frequencies: ν_0 + 347 kHz (■), ν_0 + 183 kHz (□), ν_0 + 106 kHz (▲), ν_0 + 37 kHz (△), ν_0 + 30 kHz (◆), ν_0 + 25 kHz (◇), ν_0 + 19 kHz (●), ν_0 + 14 kHz (○). For all but the hottest clouds, $\tilde{T}$ is demonstrably below both the predicted 3D and 1D BEC transition temperatures where we conventionally would expect bimodal density distributions. Much of this data lies above $k_B\tilde{T} \equiv |\mu_{int,c}|$, meaning our $\tilde{T}$ and $\tilde{\zeta}$ measurements are valid to well below $\tilde{T}_c$. (c) Example axial cross-section near the 3D condensation threshold. The red line indicates the optical depth at each pixel; the black line shows the cross section of the best fit 2D thermal background gaussian. In particular, as the condensation threshold is crossed, density spikes like the one near this cloud's center become statistically more prevalent, as quantified in Fig. 2.3.

Made clear in the figure, our evaporation sequences produce clouds that cross the condensation threshold at $\tilde{T} = \tilde{T}_c$ between a half and a full order of magnitude above $k_B\tilde{T} = |\mu_{int,c}|$, where $T = \tilde{T}$ remains a good approximation. This substantiates our claim to have cooled to and below $\tilde{T}_c$, or equivalently that the $\tilde{\zeta}$ measurements accurately reflect rising above the minimum needed to achieve quantum degeneracy.

While we are technically unable to ascribe a cardinal temperature around and below $k_B\tilde{T} = |\mu_{int,c}|$, we observe that additional evaporation reduces the axial cloud widths to 1/6 their $\tilde{T}_c$ value and note that for non-interacting particles this would correspond to $\tilde{T} \approx \tilde{T}_c/30$, implying that, at least in an ordinal sense, our search for bimodal density distributions and conventional BEC extends significantly below $\tilde{T}_c$.

The cloud cross-sections show further evidence for the onset of condensation in the increase in the degree of irregularity in the density profile above the thermal gaussian background as ν_f decreases. One explanation for these density spikes is they are "Bosenova" remnants or precursors [25], but regardless of cause such incongruity occurs mostly near the thermal cloud center, and we quantify it by summing the net atoms exceeding the thermal background gaussian, pixel by pixel, within each thermal cloud's $e^{-1/8}$ density radius. Normalizing by N_a produces the fraction of condensed atoms, n_c, which is plotted in Fig. 2.3 where it clearly rises as the BEC threshold is crossed, supporting our claim that $\tilde{T} = \tilde{T}_c$ genuinely corresponds to $T = T_c$.

2.3.2 BEC initiates, then quenches

At this point, however, conventional condensation appears to quench. One notable way that we have investigated this quenching is to look for a spike in the specific heat, C, upon crossing the BEC threshold. Conventionally, specific heat is a measure of the amount of heat ΔQ needed to change a material's temperature by ΔT per amount of that material. Spikes in C occur when crossing thermodynamic phase transitions generally because starting from just above the transition a relatively large amount of heat must be removed to freeze out one or more degrees of freedom, and yields only a small change in temperature. If no work is done on or by the system during this process, then $\Delta Q = \Delta E_{tot}$ is the change in the total energy of the system, which equals $N_a\Delta\mu_{tot}$ according to the GP formalism, Eg. 2.17. For

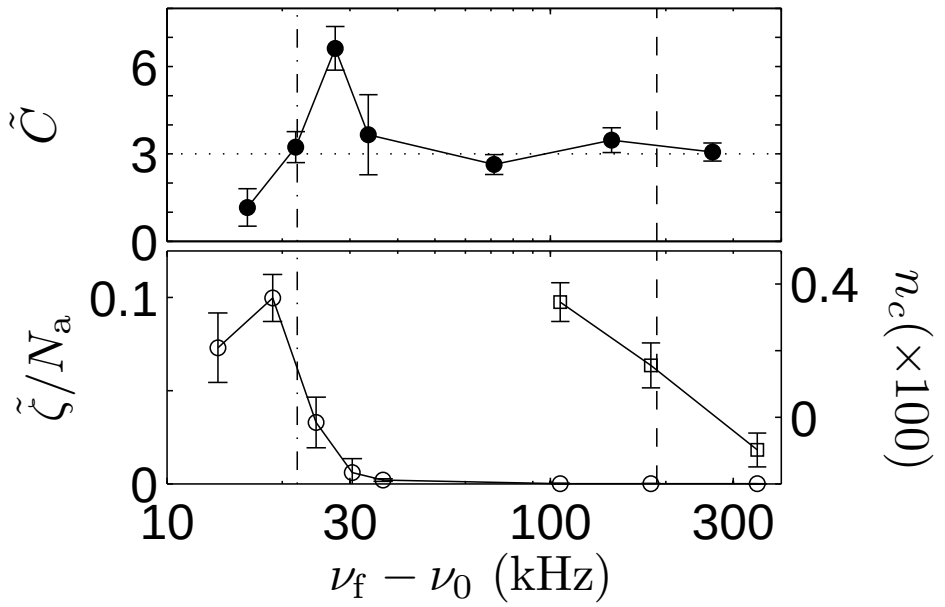

Figure 2.3: Normalized non-interacting particle specific heat, $\tilde{C}$ (•), fractional non-interacting particle phase-space density, $\tilde{\zeta}/N_a$ (○), and fraction of condensed atoms, n_c (□), as a function of the final RF evaporation frequency, ν_f. The spike in $\tilde{C}$ at $\nu_f \approx \nu_0 + 27\,\mathrm{kHz}$, indicates a phase transition. It occurs at $\nu_f - \nu_0$ nearly an order of magnitude below the theoretical 3D condensation threshold crossing in our apparatus (dashed vertical line), which is experimentally validated by the rise in n_c at that point. The spike coincides with the jump in $\tilde{\zeta}/N_a$ and with the dash-dotted vertical line marking $k_B\tilde{T} = \hbar\omega_r$, not with the jump in n_c, indicating the transition should be associated with the system going quasi-1D and heavily populating some few states rather than with crossing the condensation threshold. Above the transition, $\tilde{C}$ is approximately the value for an ideal monoatomic gas in a 3D harmonic potential, 3, shown by the dotted horizontal line. We do not report n_c for lower ν_f because as the density irregularities grow and the thermal backgrounds shrink our fitting algorithm cannot reliably differentiate between them.

our quantum system the substance amount that makes sense is each particle, so we would like to measure

$$C = \frac{\Delta\mu_{\rm tot}}{k_{\rm B}\Delta T}, \tag{2.26}$$

where to make C dimensionless we have additionally divided by $k_{\rm B}$. As discussed, without the interacting particle density of states we are unable to properly quantify T. Instead, we again use the non-interacting particle temperature, but here derive it from the final RF evaporation frequency relative to that at trap bottom, $\nu_{\rm f} - \nu_0$. For hot clouds $k_{\rm B}T = k_{\rm B}\tilde{T} = h(\nu_{\rm f} - \nu_0)/\eta$, where $\eta = 6.4 \pm 0.2$ is experimentally determined as the average of $h(\nu_{\rm f} - \nu_0)/(k_{\rm B}\tilde{T})$ calculated for every cloud at $\nu_{\rm f} = \nu_0 + 347$ kHz and $\nu_0 + 183$ kHz in our data set. At lower $\nu_{\rm f}$ this ratio increases. Putting everything together using Eq. (2.26), and recognizing its limitations when applied to interacting particles, we calculate the normalized non-interacting specific heat, $\tilde{C}$, by subtracting the average $\mu_{\rm tot}$ values corresponding with successive $\nu_{\rm f}$ values and then dividing this by the difference between the successive $\nu_{\rm f}$ values,

$$\tilde{C} = \frac{\eta\Delta\mu_{\rm tot}}{h\Delta\nu_{\rm f}}. \tag{2.27}$$

As seen in Fig. 2.3, there is a spike in $\tilde{C}$ and, unlike the case for non-interacting particles in extreme quasi-1D potentials [26], there is nearly an order of magnitude difference in $\nu_{\rm f} - \nu_0$ between it and crossing the 3D condensation threshold, indicated by the vertical dash-dotted line. It is not until this point, near $\mu_{\rm tot}/3 = 70\hbar\omega_z = 1.0\hbar\omega_r$, that we observe a large fraction of the atoms populating only a few quantum states, as indicated by the rise in $\tilde{\zeta}/N_{\rm a}$.

The normalized specific heat for an ideal monoatomic gas in a 3D harmonic potential is 3, indicated by the horizontal dashed line in Fig. 2.3, which agrees with our measured value above the phase transition. Furthermore, $\tilde{\zeta}/N_{\rm a}$ saturates near 10% indicating that a pure state is not formed. The atom cloud becomes quantum degenerate but remains distributed amongst a manifold of axial states, numbering approximately $N_{\rm m} = N_{\rm a}/\tilde{\zeta} = 14 \pm 4$ at our coldest $\nu_{\rm f}$.

The rise in $\tilde{\zeta}/N_{\rm a}$ appears to coincide with the cloud going 1D, and direct measurement of the radial widths corroborates this, as shown in Fig. 2.4. Though the average $\sigma_r/\sigma_{r,0}$ for the lowest $\nu_{\rm f}$ (•) is constrained to equal 1 in order to solve for $\sigma_m athrm PS F$, Sec. 2.2.2,

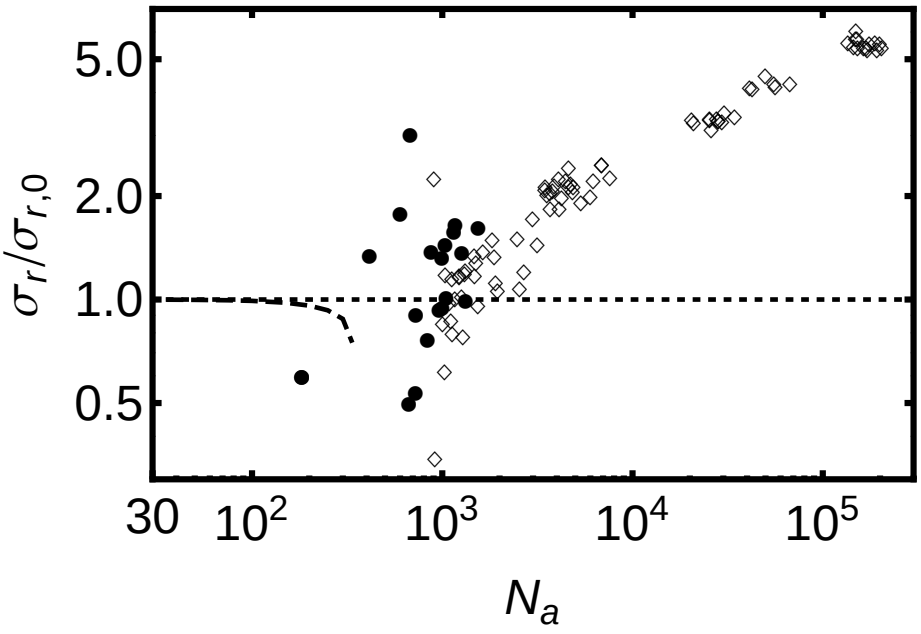

Figure 2.4: Radial width normalized to its non-interacting ground state size as a function of atom number. The horizontal dotted line at 1 indicates the expected radial ground state width for non-interacting particles. By design the coldest, $\nu_f = \nu_0 + 14\,\mathrm{kHz}$, data points (•) have average value 1, which was one of the two constraints in solving for t_{TOF} and $\sigma_m athrmPSF$. At higher ν_f (⋄), the low N_a points are also centered on 1, indicating that radial freeze out occurs above $\nu_f = \nu_0 + 14\,\mathrm{kHz}$. At these interaction energies we expect some clouds to be at or below the non-interacting radial width, $\sigma_{r,0} = 0.64\,\mu\mathrm{m}$, though above the dashed line indicating the mean-field GP predicted radial ground state width for $N_a < N_c$ [10]. We largely attribute the σ_r spread at low N_a to photon and atom shot noise which our measurements become increasingly sensitive to as σ_r approaches $\sigma_m athrmPSF$.

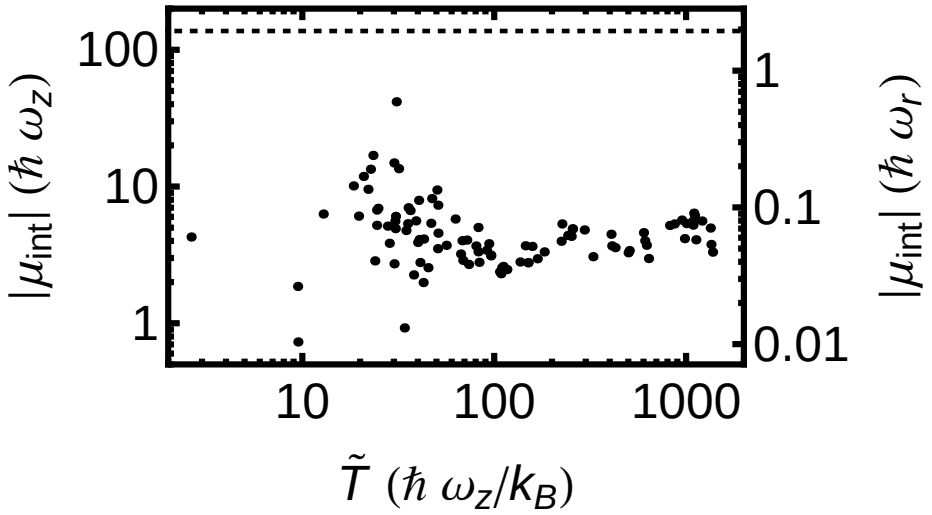

Figure 2.5: Peak interaction energy per particle, normalized to both the axial and radial mode spacings, as a function of normalized $\tilde{T}$. The horizontal dotted line at $|\mu_{\rm int}|/\hbar\omega_r = |\mu_{\rm int,c}|/\hbar\omega_r = 1.95$ indicates the collapse threshold. This data demonstrates that throughout our cooling evaporation sequence the peak interaction energy per particle is significantly greater than the axial mode spacing while remaining suitably below the radial mode spacing so that the clouds remain stable against collapse.

the overlapping higher $\nu_{\rm f}$ clouds have similar values and spread, indicating radial freeze out occurs above $\nu_{\rm f}$.

2.3.3 Potential cause: trap anisotropy plus attractive interactions

We note that trap anisotropy and the non-interacting particle two-step condensation model cannot explain these results [26]. Clearly in Fig. 2.2, our data avoid the two-step condensation regime for non-interacting particles by passing well above the intersection of the 3D and 1D condensation threshold curves. Rather, we speculate that trap anisotropy places us in a regime where particle interactions are important in determining the condensation dynamics. As indicated in Fig. 2.5, we produce clouds wherein the peak interaction energy per particle lies between the energy splitting of the weakly and tightly confining dimensions, axial and radial, respectively. Thus, we observe clouds with $|\mu_{\rm int}| \approx 5\hbar\omega_z = \hbar\omega_r/14$, so

that throughout evaporation the interactions are several times stronger than the axial mode splitting energy while simultaneously satisfying the BEC stability criterion, $|\mu_{\rm int}| < |\mu_{\rm int,c}| = 1.95\hbar\omega_r$ (dotted line), Eq. (2.16) [10]. Furthermore, as discussed below, the expected low energy states are multiple solitons with widths smaller than we can reliably resolve with our imaging system. Thus our $|\mu_{\rm int}|$ measurements provide a lower bound on the true values of $|\mu_{\rm int}|$, where the local interaction strengths for these solitons are predicted to go much higher, up to $|\mu_{\rm int,c}| = 140\hbar\omega_z$ in our trap [10]. In any case, clearly the trap cannot dominate the interaction dynamics in the axial dimension, and the normal mechanism for enforcing single state occupation could be frustrated.

2.3.4 Comparison with the exact 1D solution

This makes the clouds produced here prime examples of a strongly attractively interacting quasi-1D Bose gas. Though no exact solution has been found for the specific case of harmonic axial confinement, true 1D systems with attractive two-body δ-function interactions and longitudinal freedom are exactly solved [27]. The exact spectrum and many-body eigenstates, so called string states, are derived in [22], where the spectrum is characterized by one or more bound states, or strings, each having a well-defined atom number and real momentum. Though within strings the atoms are tightly bound, the strings do not interact with each other, as can be understood from the energy eigenvalue equation for these many-body states,

$$E = \sum_{\ell=1}^{\ell_{Tot}} n_\ell \frac{\hbar^2 k_\ell^2}{2m} - \frac{1}{24}\frac{m {g_{\rm 1D}}'^2}{\hbar^2} n_\ell (n_\ell^2 - 1), \tag{2.28}$$

where ℓ indexes the strings, n_ℓ and k_ℓ are, respectively, the number of atoms and single-particle momentum of string ℓ, and ${g_{\rm 1D}}'$ is the true 1D atom-atom coupling constant. For every string ℓ, the first term is the center of mass kinetic energy and the second term is the binding energy; no string-string interaction energy term exists [22]. The ground state, a single momentumless string containing all $N_{\rm a}$ atoms and existing in a linear superposition at every point in the 1D space, is the exactly-solved analog of the atomic soliton ground state solution predicted by the mean-field GP equation [28, 22, 29, 30]. That we do not produce this ground state even at our coldest $\nu_{\rm f}$ data, if not clear from the absorption images,

Fig. 2.2(a)(d-h), is clear in the $\sigma_r \sim {N_a}^{0.7}$ dependence shown in Fig. 2.2, versus $\sigma_r \sim {N_a}^{-1}$ for the exact ground state, and in the $\rho_{pk} \sim {N_a}^{-0.2}$ dependence, versus the exact ground state's $\rho_{pk} \sim {N_a}^{2}$.

Accounting for finite transverse confinement modifies the exact result only slightly. Two colliding strings will pass through one another provided the peak density during their overlap does not exceed the critical density where collapse occurs [31]. Another important correction due to the finite radial cloud size is the breaking of integrability of the effective 1D Hamiltonian. Equal mass particles with delta-function interactions in true 1D do not thermalize [32]; however, our system is quasi-1D. The strong but finite transverse confinement sufficiently stabilizes the formation of multiple string states and perhaps frustrates conventional BEC but is insufficient to prevent thermalization and additional cooling after the transition to quasi-1D [33].

2.3.5 Multiple macroscopically occupied modes

A lower bound on each cloud's soliton number can be calculated using the collapse criterion for our trap parameters, $N_c \approx 330$ [10]. Specifically, $N_{m,min} = N_a/N_c = 2.3 \pm 0.3$ for our lowest ν_f. A more reasonable estimate of the number of occupied modes may be the reciprocal of the fractional non-interacting phase space density, $N_m = N_a/\tilde{\zeta} = 14 \pm 4$. Because the ten to twenty pixels these clouds generally span is of the same order, individual solitons or discrete groups of solitons should be resolved for only a fraction of images at our coldest RF cuts, as in Fig. 2.1(d-h).

In terms of technology development, this effect, driven we believe by trap geometry and particle interaction, could make possible the robust production of bright, short coherence length, matter-waves. The occupation of multiple states will reduce the coherence length of atoms outcoupled from the cloud by a factor of ${N_m}^{-1/2}$ [34]. Such sources represent the matter-wave analog of optical superluminescent diodes, whose short coherence lengths facilitate increased precision in fiber optic ring gyroscopes. Applications of atomic superluminescent sources, as well as of the follow-on matter-wave sources we next would like to create, are discussed in Ch. 4.

2.4 Potential error sources: inequilibrium and heating

Finally, these excited states with multiple solitons appear to be the limit one can reach in our trap. Though we empirically optimized our evaporation sequence to maximize $\tilde{\zeta}$ at each point in time, we cannot exclude the possibility that the loss mechanisms present in our trap prevent us from ramping sufficiently slowly to reach equilibrium. Additionally, the small axial mode spacing increases our sensitivity to heating and technical noise. To quantify the atom loss and heating rates, we evaporated down to $\nu_\mathrm{f} = \nu_0 + 14\,\mathrm{kHz}$, then held the atoms for a variable time in the IP trap with the evaporation RF turned off, up to 7 s, and measured N_a and $\tilde{T}$, see Fig. 2.6. Though we lack a solid understanding of the initially observed cooling, the heating between 5 and 7 s places an upper bound on the heating rate at $4.3\,\mathrm{nK/s} \approx 2(\hbar\omega_z/k_\mathrm{B})\,/\mathrm{s}$. The atom lifetime of 0.8 s indicates a loss process is present, most likely three-body collisions. Lastly, because $|\mu_{int}| > \hbar\omega_z$, instead of a single well resolved ground state, the many-body energy landscape of the system could exhibit a manifold of nearly degenerate metastable states, and once the atoms enter into one of these they become kinetically trapped for the finite time of the experiment. This hypothesis is next investigated theoretically.

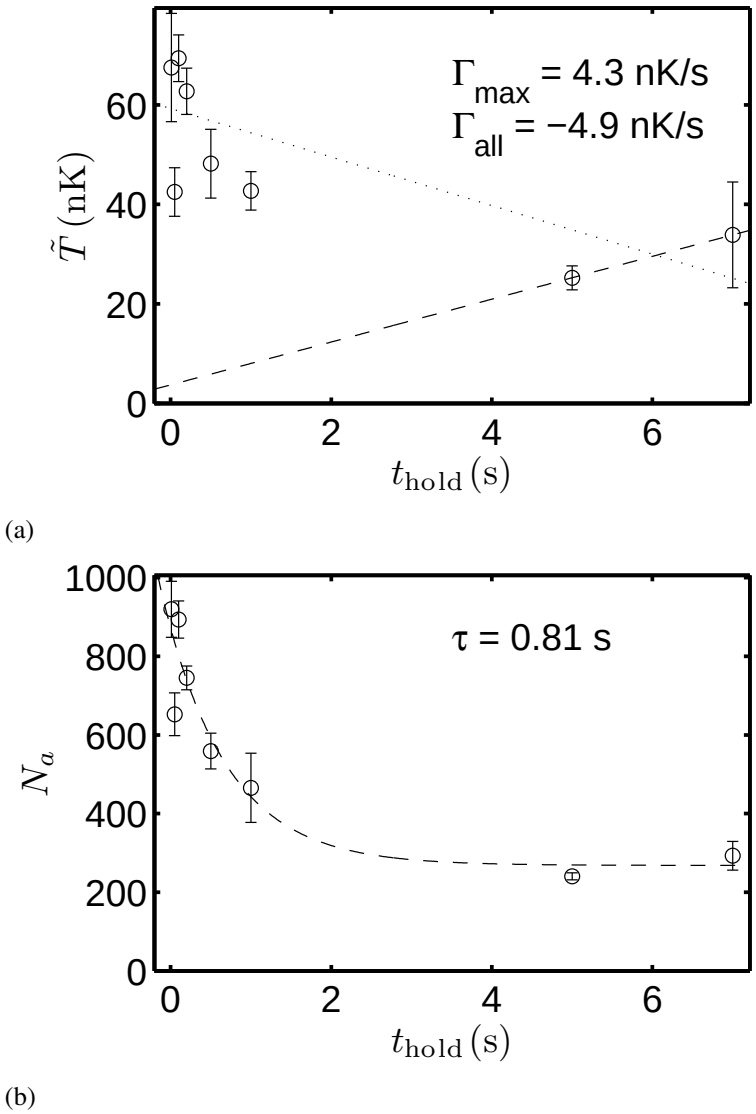

Figure 2.6: Heating rate and atom loss rate after evaporating to $\nu_f = \nu_0 + 13\,\mathrm{kHz}$, then turning the RF off. (a) Non-interacting particle temperature as a function of hold time. The best linear fit to all the points (dotted line) indicates that overall cooling is observed. The dashed line connecting the final two hold times has a slope of $4.3\,\mathrm{nK/s} \approx 2(\hbar\omega_z)/\mathrm{s}$, which upper bounds the heating rate. The initial cooling is not well understood. (b) Atom number as a function of hold time. The best fit double exponential (dashed line) predicts a fast loss rate of $\tau = 0.8\,\mathrm{s}$ and a very long second decay rate, corresponding to single exponential decay to a non-zero constant. The fast rate indicates a loss mechanism, most likely three-body collisions.

Chapter 3

Theory

3.1 Background

Whether sufficiently cooled attractively interacting, $a < 0$, boson ensembles will form Bose-Einstein condensates (BECs) that are pure, having a single macroscopically occupied state, or fragmented, having more than one macroscopically occupied state, has been debated by theorists since long before their initial experimental realization in dilute atomic ^{7}Li vapor [3], simultaneous with the creation of repulsively interacting BECs [1, 2]. The more specific follow-up question of whether the atom clouds in our system, with finite N_a, attractive interactions, a quasi-1D harmonic potential, non-zero temperature, and $N_\mathrm{m} \approx 10$ occupied single-particle states, correspond to pure or fragmented many-body states remains an unresolved theoretical challenge.

To date, progress has been made only by relaxing one or more these constraints, beginning with considering homogeneous systems in free space in the thermodynamic limit. Under these conditions, repulsively interacting particles energetically prefer forming a pure condensate. Attractively interacting particles would energetically prefer forming a fragmented condensate, except that self-collapse overcomes the formation of any condensates, pure or fragmented [35, 36]. However, adding three-dimensional (3D) isotropic harmonic confinement and finite atom number, N_a, it was shown that metastable pure BECs can exist so long as N_a lies below a critical value, N_c [8, 9, 10], a prediction matched by experimental data [3, 13]. In this potential, allowing for scattering amongst $N_\mathrm{m} = 2$ single-particle states

predicts that any stable condensates in such traps are pure, because fragmentation occurs only for $N_a > N_c$ [37]. Switching from exact diagonalization to an energy functional approach, and allowing the two single-particle states to have independent variational widths has shown the existence of metastable states with $N_a < N_c$ when macroscopic occupation of both single particle states is strictly enforced [38]. However the cause of such macroscopic occupation has not been adequately explained. This methodology has also been extended to one-dimensional (1D) systems with and without longitudinal freedom [39, 40].

One goal of our theory effort then, is to develop a model of attractively interacting bosons in a 1D harmonic potential that predicts a many-body ground state having multiply macroscopically occupied single-particle states. Perhaps more relevant to the experimental results reported in Ch. 2 is to determine the degree of degeneracy of the many-body states in our system. Our approach is to use exact diagonalization over a truncated Hilbert space of N_a atoms scattering between $N_m = 2$ single-particle states, as in [37], and allow for independent variational mode widths, as in [38], where useful.

However before invoking models, a succinct high level explanation of why fragmentation might be favorable for attractively interacting bosons at zero temperature in quasi-1D harmonic potentials but not in isotropic potentials can be understood by considering the system energetics. Fundamentally, the criterion for stability against collapse of an attractive BEC depends on the atom-atom interaction energy per particle being roughly less than the mode spacing of the potential's tightest confining dimension [8, 9, 10, 37]. Conversely, the criterion for fragmentation depends on the atom-atom interaction energy per particle being roughly greater than the mode spacing of the potential's loosest confining dimension. For an isotropic trap these mode spacings are equivalent and both criteria cannot be simultaneously met [37]. However, for anisotropic traps with sufficiently high aspect ratio both criteria can be satisfied simultaneously, allowing stable and robust fragmented states to form. Though our theory formalizes this idea more mathematically, such interplay between attractive interaction strength and trap anisotropy lies at the heart of our discussion of fragmentation.

3.1.1 The two-body interaction Hamiltonian

The basis of our theory, and common to all analyses discussed in this chapter, is the two-body interaction Hamiltonian:

$$\hat{H} = \sum_i \langle i|\hat{t} + \hat{u}|i\rangle \hat{a}_i^\dagger \hat{a}_i + \frac{1}{2}\sum_{ijkl} V_{ijkl}\hat{a}_i^\dagger \hat{a}_j^\dagger \hat{a}_k \hat{a}_l, \tag{3.1}$$

where i, j, k, and l index the single-particle states, $|i\rangle$, having wavefunctions $\phi_i(\vec{r})$. $\hat{t}$ and $\hat{u}$ are the single-particle kinetic and trap potential energy operators, respectively, such that $(\hat{t} + \hat{u})\,|i\rangle = E_{0,i}\,|i\rangle$, where $E_{0,i}$ is the energy of $|i\rangle$. $\hat{a}_i^\dagger$ and $\hat{a}_i$ are the respective bosonic creation and annihilation operators for particles in $|i\rangle$. $\hat{a}_i^\dagger \hat{a}_i = \hat{n}_i$ is the corresponding number operator and $\hat{a}_i^\dagger \hat{a}_i^\dagger \hat{a}_i \hat{a}_i = \hat{n}_i\,(\hat{n}_i - 1)$. Including the sum over all single-particle states i, the first term represents the many-body Hamiltonian for interactionless particles:

$$\hat{H}_0 = \sum_i E_{0,i}\hat{n}_i. \tag{3.2}$$

This non-interacting many-body Hamiltonian is diagonalized by many-body states $|\Psi\rangle$ having defined occupation numbers for each single-particle state, $|\Psi\rangle = \left|n_0, n_1, \ldots, n_{N_\mathrm{m}-1}\right\rangle$, where n_i is the number of particles in mode $|i\rangle$ and N_m is the total number of modes available to the particles.

The second sum in the full Hamiltonian represents the interactions between the particles. Each $\{i, j, k, l\}$ term represents two particles scattering from modes k and l into modes i and j, where V_{ijkl} quantifies the probability of this scattering event occurring and is given by the overlap integral of the single-particle states involved and the nature of the interactions. For general isotropic interactions,

$$V_{ijkl} = \frac{4\pi\hbar^2}{m}\int \mathrm{d}^3r'\mathrm{d}^3r\,\phi_i^*(\vec{r'})\phi_j^*(\vec{r'})u(|\vec{r} - \vec{r'}|)\phi_k(\vec{r})\phi_l(\vec{r}), \tag{3.3}$$

where $u(|\vec{r} - \vec{r'}|)$ describes the interaction potential. In cold atom experiments, hard sphere s-wave scattering is typically considered, corresponding to the pseudopotential $u(|\vec{r} - \vec{r'}|) = a\delta^3(|\vec{r} - \vec{r'}|)$, where a is the s-wave scattering length and is positive for repulsive interactions

and negative for attractive interactions. Integrating over $\mathrm{d}^3 r'$ simplifies V_{ijkl} to

$$V_{ijkl} = g_{3\mathrm{D}} \int \mathrm{d}^3 r \, \phi_i^*(\vec{r}) \phi_j^*(\vec{r}) \phi_k(\vec{r}) \phi_l(\vec{r}), \tag{3.4}$$

where $g_{3\mathrm{D}} = 4\pi\hbar^2 a/m$ is the interaction coupling coefficient. Summing over all permutations of single-particle states $\{i, j, k, l\}$ accounts for all possible 2-body interactions within the parameters of the model.

Taken together both terms complete the many-body Hamiltonian with 2-body interactions, $\hat{H}$. In general no longer diagonalizable with single non-interacting many-body states $\left|n_0, n_1, \ldots, n_{N_\mathrm{m}-1}\right\rangle$, eigenstates of $\hat{H}$ are formed from superpositions of such states,

$$|\Psi_i\rangle = \sum_{n_0, n_1, \ldots n_{N_\mathrm{m}-1}=0}^{N_a} C_{i;n_0,n_1,\ldots n_{N_\mathrm{m}-1}} |n_0, n_1, \ldots n_{N_\mathrm{m}-1}\rangle, \tag{3.5}$$

such that $\hat{H}\,|\Psi_i\rangle = E_i\,|\Psi_i\rangle$ where E_i are the many-body eigenenergies.

As a concrete example, for a system of $N_\mathrm{a} = 3$ atoms amongst $N_\mathrm{m} = 2$ modes,

$$\left|\Psi_{i;N_\mathrm{a}=3,N_\mathrm{m}=2}\right\rangle = C_{i;3,0}|3,0\rangle + C_{i;2,1}|2,1\rangle + C_{i;1,2}|1,2\rangle + C_{i;0,3}|0,3\rangle$$

is defined by the $N_\mathrm{a} + 1 = 4$ complex numbers $\{C_{i;3,0}, C_{i;2,1}, C_{i;1,2}, C_{i;0,3}\}$, one associated with each Hilbert space basis state, where the first index labeling the Cs is the many-body state index, the second is n_0 and the third is n_1. n_0 and n_1 are the first and second basis state indices. Scaling up to $N_\mathrm{a} = 3$ particles amongst $N_\mathrm{m} = 3$ modes substantially increases the Hilbert space size,

$$\begin{aligned}
\left|\Psi_{i;N_\mathrm{a}=3,N_\mathrm{m}=3}\right\rangle &= C_{i;3,0,0}|3,0,0\rangle + C_{i;2,1,0}|2,1,0\rangle + C_{i;1,2,0}|1,2,0\rangle + C_{i;0,3,0}|0,3,0\rangle \\
&+ C_{i;2,0,1}|2,0,1\rangle + C_{i;1,1,1}|1,1,1\rangle + C_{i;0,2,1}|0,2,1\rangle \\
&+ C_{i;1,0,2}|1,0,2\rangle + C_{i;0,1,2}|0,1,2\rangle \\
&+ C_{i;0,0,3}|0,0,3\rangle,
\end{aligned}$$

which for general N_a and N_m is given by

$$N_{HS} = \frac{(N_a + N_m - 1)!}{(N_m - 1)!\, N_a!}. \tag{3.6}$$

This expression can be regrouped as

$$N_{HS} = \frac{1}{(N_m - 1)!} N_a^{N_m - 1} + O\left(N_a^{N_m - 2}\right), \tag{3.7}$$

where in the large N_a limit, $N_a \gg 1, N_m$, the second term can be neglected.

Exactly solving for the interacting many-body eigenstates and eigenenergies of such a system requires diagonalizing $\hat{H}$, in it's full form a matrix with $N_{\hat{H}} = N_{HS} \times N_{HS}$ elements. Tantalizingly, when we limit the interactions to two-body and no higher, the majority of these elements will be 0. An estimate of the number of non-zero elements in $\hat{H}$, $N_{nonzero}$, is $N_{HS} \times N_s$, where N_s is the the maximum number of final many-body basis states that an initial many-body basis state can scatter into:

$$N_s = 1 + 2N_m (N_m - 1). \tag{3.8}$$

In the large N_a limit, most basis states will have N_s basis states to scatter into, so $\hat{H}$ will have

$$N_{nonzero} \approx \frac{1 + 2N_m (N_m - 1)}{(N_m - 1)!} N_a^{N_m - 1}. \tag{3.9}$$

The exponential dependence of $N_{nonzero}$ on N_m reduces substantially from that of $N_{\hat{H}}$, by a factor of two, but remains an exponential dependence; solving real problems exactly remains computationally impracticable, merely to a lesser degree. In rough numbers, even at our lowest final evaporation frequency, $\nu_f = \nu_0 + 14\,\mathrm{kHz}$, producing our coldest and smallest clouds, our data indicate $N_a \gtrsim 10^2$ and $N_m \gtrsim 10$, requiring a computer capable of diagonalizing a sparse matrix with 10^{15} non-zero elements. Contextualizing this, a typical laptop today can diagonalize a fully represented matrix with $10^7 - 10^8$ elements. So even if more computationally efficient sparse matrix diagonalization algorithms are implemented and Moore's law continues to hold this, routinely solving this problem on a laptop is $\gtrsim$ 40 years away. The bigger question of how N_a attractively interacting atoms in an

infinitely sized complete orthonormal basis of single particle states will arrange themselves will require a different conceptualization of the problem.

Application: deriving the Gross-Pitaevskii equation

As a first step beyond single-particle quantum mechanics, a basic application of the two-body interaction Hamiltonian, Eq. (3.1) is to consider N_a interacting particles allowed to occupy only one state, $|\Psi\rangle = \left|\phi_0^{\otimes N_\mathrm{a}}\right\rangle = |N_\mathrm{a}, 0, 0, \ldots\rangle$. This constraint reduces the Hamiltonian to

$$\begin{aligned}\hat{H} &= \langle 0|\hat{t} + \hat{u}|0\rangle \hat{a}_0^\dagger \hat{a}_0 + \frac{1}{2} V_{0000} \hat{a}_0^\dagger \hat{a}_0^\dagger \hat{a}_0 \hat{a}_0 \\ &= \langle 0|\hat{t} + \hat{u}|0\rangle \hat{n}_0 + \frac{1}{2} V_{0000} \hat{n}_0 \left(\hat{n}_0 - 1\right) \end{aligned} \tag{3.10}$$

Writing out the integrals explicitly, integrating the first term by parts, and dividing by $n_0 = N_\mathrm{a}$ produces the Gross-Pitaevskii (GP) per particle energy functional [7], Eg. (1.8),

$$\frac{E[\phi_0^{\otimes N_\mathrm{a}}]}{N_\mathrm{a}} = \int \mathrm{d}^3 r \left[\frac{\hbar^2}{2m} |\vec{\nabla}\phi_0|^2 + V_{trap} |\phi_0|^2 + (N_\mathrm{a} - 1) \frac{1}{2} g_{3\mathrm{D}} |\phi_0|^4 \right].$$

Its importance and use are discussed in Sec. 1.1.2.

Application: interacting homogenous thermodynamic BEC in free space

Another illustrative application of the two-body interaction Hamiltonian is to consider an interacting but homogeneous BEC, $\hat{t} = 0$, in free space, $\hat{u} = 0$, following [35, 36]. The single-particle states that diagonalize the non-interacting free space Hamiltonian are plane waves with momentum k, $|k\rangle$; the many-body basis states have well-defined particle numbers for each k. The total Hamiltonian simplifies to

$$\begin{aligned}\hat{H} &= \frac{1}{2} \sum_{ijkl} V_{ijkl} \hat{a}_i^\dagger \hat{a}_j^\dagger \hat{a}_k \hat{a}_l \\ &= \frac{1}{2} \sum_{k,k',q} V_q \hat{a}_k^\dagger \hat{a}_{k'}^\dagger \hat{a}_{k'-q} \hat{a}_{k+q}, \end{aligned} \tag{3.11}$$

where the second equality incorporates conservation of momentum. The exclusive dependence of $V_{k,k',q} = V_q$ on exchange momentum, q, requires hard sphere interactions, $u(|\vec{r}-\vec{r'}|) = a\delta^3(|\vec{r}-\vec{r'}|)$. The energy of a pure state with N_a particles solely occupying $|0\rangle$ is

$$\begin{aligned} E_{0,\,\mathrm{pure}} &= \frac{1}{2}V_0\langle\hat{a}_0^\dagger\hat{a}_0^\dagger\hat{a}_0\hat{a}_0\rangle = \frac{1}{2}V_0 n_0(n_0-1) \\ &\approx \frac{1}{2}V_0 N_a^2. \end{aligned} \tag{3.12}$$

In contrast, the energy of a fragmented state with N_a particles occupying both $|0\rangle$ and $|q_1\rangle$, $n_0 + n_{q_1} = N_\mathrm{a}$, is

$$E_{0,\,\mathrm{q_1},\,\mathrm{frag}} \approx \frac{1}{2}V_0 N_a^2 + V_{|q_1|}n_0 n_{q_1}. \tag{3.13}$$

The energy difference $V_{|q_1|}n_0 n_{q_1}$ is proportional to $V_{|q_1|}$ which in turn is proportional to a. Thus, for repulsive interactions, $a > 0$, the pure state has lower energy so is favored; for attractive interactions, $a < 0$, the fragmented state is energetically favored. Finally, taking the thermodynamic limit, the per particle energy for attractive interactions runs away to negative infinity as more and more atoms pile into the same state, indicating such BECs are unstable against collapse.

3.1.2 Quantifying fragmentation: single-particle density matrix

Following on this example where fragmentation is energetically preferred in some cases, fragmentation is quantified using the single-particle density matrix (SPDM) formalism [41, 28]. To determine the degree of fragmentation, first the particle number, N_a, and the N_m single-particle basis states are chosen. $\hat{H}$ is created term by term, and diagonalized to yield the many-body energies, E_i, and eigenstates, $|\Psi_i\rangle$, each defined in the non-interacting many-body state representation by its set of N_HS C numbers, $\left\{C_{i;n_0,n_1,\ldots n_{N_\mathrm{m}-1}}\right\}$. For any given many-body state $|\Psi_i\rangle$, its SPDM, $\hat{\rho}$, is created from expectation values of single-particle

state creation and annihilation operator pairs taken with respect to $|\Psi_i\rangle$:

$$\hat{\rho} = \frac{1}{N_a} \begin{pmatrix} \langle \hat{a}_0^\dagger \hat{a}_0 \rangle & \langle \hat{a}_0^\dagger \hat{a}_1 \rangle & \dots & \langle \hat{a}_0^\dagger \hat{a}_{N_\mathrm{m}-1} \rangle \\ \langle \hat{a}_1^\dagger \hat{a}_0 \rangle & \langle \hat{a}_1^\dagger \hat{a}_1 \rangle & \dots & \langle \hat{a}_1^\dagger \hat{a}_{N_\mathrm{m}-1} \rangle \\ \vdots & \vdots & \ddots & \vdots \\ \langle \hat{a}_{N_\mathrm{m}-1}^\dagger \hat{a}_0 \rangle & \langle \hat{a}_{N_\mathrm{m}-1}^\dagger \hat{a}_1 \rangle & \dots & \langle \hat{a}_{N_\mathrm{m}-1}^\dagger \hat{a}_{N_\mathrm{m}-1} \rangle \end{pmatrix}. \tag{3.14}$$

Finally, $\hat{\rho}$ itself is diagonalized, with its eigenvalues, ε_i, determining the degree of fragmentation. Specifically, each ε_i corresponds to the fraction of particles in many-body state $|\varepsilon_i\rangle$. Consequently, if only one $\varepsilon_i \sim O(1)$, the many-body state is pure; if more than one $\varepsilon_i \sim O(1)$, the many-body state is fragmented, with the number of macroscopically occupied many-body states equal to the number of $\varepsilon_i \sim O(1)$. The components of each $|\varepsilon_i\rangle$ encode the decomposition of that many-body state amongst the single-particle states. Namely, of the N_m components of $|\varepsilon_i\rangle$, the jth is $\langle j|\varepsilon_i\rangle$, the projection of $|\varepsilon_i\rangle$ onto single particle state $|j\rangle$.

For typical trap potentials, there exists a threshold N_a value above which fragmentation occurs, N_f. As cursorily explained immediately before Sec. 3.1.1, N_f is roughly the N_a value where the interaction energy per particle becomes greater than the mode spacing of the loosest confining dimension. It is found with exact diagonalization by increasing N_a from 0 until more than one $\varepsilon_i \sim O(1)$.

3.1.3 Quantifying fragmentation: semiclassical approximation

For $N_\mathrm{a} \gg 1$, a semiclassical approach yields analytical solutions for E_0 and n_0 that are in close agreement with the exact solutions but require far less computation [37, 38, 39]. Additionally, when off-diagonal long range order can be neglected, as is the case for $N_\mathrm{m} = 2$ single-particle states with odd-relative parity but not for even-relative parity, it also quickly yields ε_0 and N_f. Essentially, one selects N_a and determines the N_m single-particle wavefunctions, $\{\phi_0, \phi_1, \dots, \phi_{N_\mathrm{m}-1}\}$, which can depend on variational parameters or not, then calculates the expectation value of $\hat{H}$ in the $N_\mathrm{a} \gg 1$ limit with respect to the many-body state $|\Psi\rangle = |N_\mathrm{a}, N_\mathrm{m}, \{\phi_i\}, \{f_i\}\rangle$, where $f_i = n_i/N_\mathrm{a}$ denotes the fractional occupation of ϕ_i. The resulting energy functional depends on the same variables, $E = E(N_\mathrm{a}, N_\mathrm{m}, \{\phi_i\}, \{f_i\})$. For

any N_a, the ground state properties are then given by the N_m basis state relative populations and, if present, the set of variationally optimized single-particle wavefunctions such as minimize the energy functional, $\{f_{i,0}\}$ and $\{\phi_{i,0}\}$, respectively. In this method the $f_{i,0}$ determine the degree of fragmentation, playing the same role that the ε_i play for exact diagonalization.

This approach loses the effects of finite N_a, e.g. it allows non-integer occupation numbers, and eliminates the ability to uniquely consider superpositions of non-interacting basis states, as explicitly allowed for in Eq. 3.5. This in turn effectively eliminates the influence of the off-diagonal elements in $\hat{H}$ which, as our theoretical work shows, end up playing an important role in attractively interacting 1D bosonic systems.

3.2 Methodology

3.2.1 Overview

Armed with the SPDM and semiclassical formalisms, we generally follow the approach that Elgarøy and Pethick take to predict that attractively interacting stable BECs in a 3D isotropic harmonic potential must be pure [37], and instead show that the same particles in a 1D harmonic potential form condensates that fragment for $N_a < N_c$. We demonstrate that the semiclassical approximation closely matches the exact solution for pairs of single-particle states having odd-relative parity, and then use it to show there are many energy-adjacent state pairs (odd-relative parity) that fragment for $N_f < N_c$ for our experimental parameters. Investigating the exact energy spectra, we show that for a given pair of states with finite N_f, for $N_a \gtrsim N_f$ every other many-body states' per particle excitation energy splitting converges to zero much faster than the $O\left(N_a^{-1}\right)$ typical of mean-field interactions. This indicates a substantial increase in the degree of degeneracy of the many-body states above N_f which is predicted to accompany fragmentation [28].

Also revealed is the importance of single-particle state pair relative parity on fragmentation in 1D harmonic potentials. Odd-relative parity single-particle state pairs tend toward fragmented ground states and high degenerate many-body eigenenergy fractions at high N_a. Even-relative parity single-particle state pairs have pure ground states and non-degenerate many-body eigenenergies for all N_a.

Finally, following Cederbaum, Streltsov, and Alon, we incorporate single-particle state pairs with independent variational widths and then create ground state energy and fragmentation landscapes in variational width space [38]. This captures an idea of the ground state spatial distribution and degree of fragmentation for $N_{\mathrm{m}} > 2$ modeling, which is computationally challenging. Applied to the ground and first excited states of a 3D isotropic harmonic potential, our model agrees with experiment [3] and conventionally accepted theory [37], predicting a purely condensed many-body ground state. Uniquely, application to a 1D harmonic trapping potential predicts a fragmented many-body ground state. Unlike in [38], however, these states are energetically stable to variations in widths *and* in occupation number. The overall many-body ground state small variational widths and the sensitivity to single-particle state pair relative parity inidcate that $N_{\mathrm{m}} = 2$ models, like the $N_{\mathrm{m}} = 1$ GP model, are inadequate for describing attractively interacting atoms in quasi-1D anisotropic potentials.

3.2.2 Exact diagonalization

Because of the aforementioned computational difficulty in solving $N_{\mathrm{m}} > 2$ models, throughout this dissertation the Hilbert space is truncated at $N_{\mathrm{m}} = 2$ single-particle states, initially labeled $|p\rangle$ and $|q\rangle$. Though we will eventually specialize, at the start these can be any two single-particle states in a potential: even or odd-relative parity, 1D or 3D, nominally or variationally-widthed. Truncating this way enforces the Fock or occupation number basis states take the form $\left|n_p, n_q\right\rangle$. N_{a} is fixed by further limiting to states of the form $\left|N_{\mathrm{a}} - n_q, n_q\right\rangle$ where n_q is an integer and $0 \leq n_q \leq N_{\mathrm{a}}$, creating a complete orthonormal basis for describing any many-body state, $|\Psi_i\rangle$, in the system with N_a particles and having $N_{\mathrm{HS}} = N_{\mathrm{a}} + 1$ elements:

$$|\Psi_i\rangle = \sum_{n_q=0}^{N_{\mathrm{a}}} C_{i;\,N_{\mathrm{a}}-n_q,n_q} \left|N_{\mathrm{a}} - n_q, n_q\right\rangle \equiv \sum_{n_q=0}^{N_{\mathrm{a}}} C_{i;\,n_q} \left|n_q\right\rangle . \tag{3.15}$$

The sums in $\hat{H}$ are similarly truncated to $\{i, j, k, l\} = p, q$:

$$\begin{aligned}
\hat{H} &= \sum_{i=p,q} \langle i|\hat{t} + \hat{u}|i\rangle \hat{a}_i^\dagger \hat{a}_i + \frac{1}{2} \sum_{ijkl=p,q} V_{ijkl} \hat{a}_i^\dagger \hat{a}_j^\dagger \hat{a}_k \hat{a}_l \\
&= \langle p|\,\hat{t} + \hat{u}\,|p\rangle\, \hat{a}_p^\dagger \hat{a}_p + \langle q|\,\hat{t} + \hat{u}\,|q\rangle\, \hat{a}_q^\dagger \hat{a}_q \\
&\quad - \frac{1}{2}|V_{pppp}| \hat{a}_p^\dagger \hat{a}_p^\dagger \hat{a}_p \hat{a}_p - \frac{1}{2}|V_{qqqq}| \hat{a}_q^\dagger \hat{a}_q^\dagger \hat{a}_q \hat{a}_q \\
&\quad - \frac{1}{2}|V_{ppqq}| \left(\hat{a}_p^\dagger \hat{a}_q^\dagger \hat{a}_p \hat{a}_q + \hat{a}_p^\dagger \hat{a}_q^\dagger \hat{a}_q \hat{a}_p + \hat{a}_q^\dagger \hat{a}_p^\dagger \hat{a}_p \hat{a}_q + \hat{a}_q^\dagger \hat{a}_p^\dagger \hat{a}_q \hat{a}_p \right) \\
&\quad - \frac{1}{2}|V_{ppqq}| \left(\hat{a}_p^\dagger \hat{a}_p^\dagger \hat{a}_q \hat{a}_q + \hat{a}_q^\dagger \hat{a}_q^\dagger \hat{a}_p \hat{a}_p \right) \\
&\quad - \frac{1}{2}|V_{pppq}| \left(\hat{a}_p^\dagger \hat{a}_p^\dagger \hat{a}_p \hat{a}_q + \hat{a}_p^\dagger \hat{a}_p^\dagger \hat{a}_q \hat{a}_p + \hat{a}_p^\dagger \hat{a}_q^\dagger \hat{a}_p \hat{a}_p + \hat{a}_q^\dagger \hat{a}_p^\dagger \hat{a}_p \hat{a}_p \right) \\
&\quad - \frac{1}{2}|V_{pqqq}| \left(\hat{a}_p^\dagger \hat{a}_q^\dagger \hat{a}_q \hat{a}_q + \hat{a}_q^\dagger \hat{a}_p^\dagger \hat{a}_q \hat{a}_q + \hat{a}_q^\dagger \hat{a}_q^\dagger \hat{a}_p \hat{a}_q + \hat{a}_q^\dagger \hat{a}_q^\dagger \hat{a}_q \hat{a}_p \right). \qquad (3.16)
\end{aligned}$$

This expression can be simplified using the commutation relations $\left[\hat{a}_i, \hat{a}_j\right] = 0$, $\left[\hat{a}_i^\dagger, \hat{a}_j^\dagger\right] = 0$, and $\left[\hat{a}_i, \hat{a}_j^\dagger\right] = \delta_{ij}$. The four $|V_p pqq|$ terms in the third line are equivalent, and in both the second to last and last lines, the first two terms are equivalent as are the second two terms. For odd-relative parity between the two single-particle states, terms V_{pppq} and V_{pqqq} integrate to zero, eliminating the bottom two lines. For even-relative parity this is not the case.

Using our two single-particle orbitals, define the kinetic and trap potential terms in $\hat{H}$ as

$$\begin{aligned}
h_{pp} &\equiv \langle p|\hat{t} + \hat{u}|p\rangle \\
h_{qq} &\equiv \langle q|\hat{t} + \hat{u}|q\rangle. \qquad (3.17)
\end{aligned}$$

Also define the scattering coefficients, Eq. (3.4),

$$\begin{aligned}
V_{pppp} &\equiv -|U_0| \\
V_{qqqq} &\equiv -\alpha|U_0| \\
V_{ppqq} &\equiv -\beta|U_0| \\
V_{pppq} + V_{pqqq} &\equiv -\gamma|U_0|. \qquad (3.18)
\end{aligned}$$

$\hat{H}$ is now expressible as

$$\begin{aligned}\hat{H} &= h_{pp}\hat{n}_p + h_{qq}\hat{n}_q \\ &\quad - \frac{1}{2}|U_0|\hat{n}_p\left(\hat{n}_p - 1\right) - \frac{1}{2}\alpha|U_0|\hat{n}_q\left(\hat{n}_q - 1\right) \\ &\quad - 2\beta|U_0|\hat{n}_p\hat{n}_q \\ &\quad - \frac{1}{2}\beta|U_0|\left(\hat{a}_p^\dagger\hat{a}_p^\dagger\hat{a}_q\hat{a}_q + \hat{a}_q^\dagger\hat{a}_q^\dagger\hat{a}_p\hat{a}_p\right) \\ &\quad - \gamma|U_0|\left(\hat{n}_p + \hat{n}_q - 1\right)\left(\hat{a}_p^\dagger\hat{a}_q + \hat{a}_q^\dagger\hat{a}_p\right). \end{aligned} \tag{3.19}$$

Though $\hat{H}$ is perhaps more elegantly represented using quasi-spin operators, as in the Lipkin model [42, 37] which lead to the semiclassical approximation equation, the above form makes it more straightforward to conceptualize the numerical exact solution achieved by constructing and diagonalizing $\hat{H}$ within the non-interacting occupation numbered many-body state basis representation. For any states $|p\rangle$ and $|q\rangle$, which may have associated variational parameter(s) λ_p and λ_q, calculate h_{pp}, h_{qq}, U_0, α, β, and γ. Each diagonal element of $\hat{H}$ is comprised of the first line of single-particle trap state energies, the second line of trap state self-interaction energies, and the third line containing the cross-term interaction energy, found by taking the expectation value of $\hat{H}$ with respect to the given occupation number basis state. The last two lines comprise the non-zero off-diagonal elements of $\hat{H}$. In the second to last line, the first term lowers the occupation number basis state by two elements in the truncated Hilbert space, corresponding to the diagonal of $\hat{H}$ two above the central diagonal. The second term raises the occupation number basis state by two elements in the truncated Hilbert space, corresponding to the diagonal of $\hat{H}$ two below the central diagonal. In the last line, the first term lowers the occupation number basis state by one element in the truncated Hilbert space, corresponding to the diagonal of $\hat{H}$ one above the central diagonal. The second term raises the occupation number basis state by one element in the truncated Hilbert space, corresponding to the diagonal of $\hat{H}$ one below the central diagonal. For odd-relative parity single-particle state pairs, $\gamma = 0$ so the last line vanishes. Either way, all off-diagonal matrix elements are calculated by taking the expectation value of $\hat{H}$ with respect to occupation number basis state pairs that are adjacent or next to adjacent. For $N_\mathrm{m} = 2$ these are the $N_\mathrm{s} = 5$ basis states that any initial basis state

may scatter into, Eg. (3.8). Correspondingly, when no higher than two-body interactions are considered, $\hat{H}$ will be a pentadiagonal, real-valued, hermitian matrix.

Diagonalizing $\hat{H}$ yields the many-body energy spectrum $\{E_i\}$ and eigenstates $\{|\Psi_i\rangle\}$, each represented in the occupation number basis as a set of projections $\left\{C_{i;\,n_q}\right\}$. We are also interested in whether the ground state, represented by $\left\{C_{0;\,n_q}\right\}$, is fragmented or not, which we determine by calculating the SPDM,

$$\hat{\rho} = \frac{1}{N_\mathrm{a}} \begin{pmatrix} \langle \hat{a}_p^\dagger \hat{a}_p \rangle & \langle \hat{a}_p^\dagger \hat{a}_q \rangle \\ \langle \hat{a}_q^\dagger \hat{a}_p \rangle & \langle \hat{a}_q^\dagger \hat{a}_q \rangle \end{pmatrix}, \tag{3.20}$$

with respect to the $\left\{C_{0;\,n_q}\right\}$ values and then diagonalize. The presence of fragmentation is determined by whether both $\varepsilon_i \sim O(1)$ or not.

3.2.3 Semiclassical approximation

In certain cases, the semiclassical approximation energy function can save considerable time computing N_f and the degree of fragmentation at a given N_a. One prescription for attaining it is to start with $\hat{H}$, Eq. (3.19), replace $\hat{n}_i$ with n_i, $\hat{a}_i$ and $\hat{a}_i^\dagger$ with $\sqrt{n_i}$, and $\hat{H}$ with E, then drop terms of order 1. Alternatively, we use quasi-spin operators, following the procedure of Ref. [37] but here considering a more generalized case. First define [1]

$$\begin{aligned} \epsilon &\equiv \left(h_{qq} + h_{pp}\right)/2 \\ \delta &\equiv \left(h_{qq} - h_{pp}\right)/2. \end{aligned} \tag{3.21}$$

[1] Note this is a different naming convention than in [37], necessitated because we allow for independent variational parameters for each single-particle state. To convert, δ here maps to $\epsilon/2$ in [37], and ϵ here maps to 2ϵ in [37].

Then define the particle number and quasi-spin operators

$$\begin{aligned}
\hat{N}_{\rm a} &= \hat{a}_p^\dagger \hat{a}_p + \hat{a}_q^\dagger \hat{a}_q \\
\hat{J}_z &= \frac{1}{2}(\hat{a}_q^\dagger \hat{a}_q - \hat{a}_p^\dagger \hat{a}_p) \\
\hat{J}_+ &= \hat{a}_q^\dagger \hat{a}_p \\
\hat{J}_- &= \hat{a}_p^\dagger \hat{a}_q \\
\hat{J}_x &= \frac{1}{2}(\hat{J}_+ + \hat{J}_-) \\
\hat{J}_y &= \frac{1}{2i}(\hat{J}_+ - \hat{J}_-)
\end{aligned}$$

and rewrite Eq. (3.19) again to obtain

$$\begin{aligned}
\hat{H} = {} & 2\delta \hat{J}_z + \epsilon \hat{N}_{\rm a} \\
& - \frac{1}{2}|U_0| \left[\frac{\hat{N}_{\rm a}}{2} \left(\frac{\hat{N}_{\rm a}}{2} - 1 \right) - (\hat{N}_{\rm a} - 1)\hat{J}_z + \hat{J}_z^2 \right] \\
& - \frac{1}{2}\alpha |U_0| \left[\frac{\hat{N}_{\rm a}}{2} \left(\frac{\hat{N}_{\rm a}}{2} - 1 \right) + (\hat{N}_{\rm a} - 1)\hat{J}_z + \hat{J}_z^2 \right] \\
& - 2\beta |U_0| (\hat{J}_x^2 + \hat{J}_y^2 - \frac{\hat{N}_{\rm a}}{2}) - \beta |U_0| (\hat{J}_x^2 - \hat{J}_y^2) \\
& - 2\gamma |U_0| \left(\hat{N}_{\rm a} - 1 \right) \hat{J}_x .
\end{aligned} \tag{3.22}$$

Next make the semiclassical approximation:

$$\begin{aligned}
N_{\rm a}, N_{\rm a}/2 &\gg 1, \\
J_x &= (N_{\rm a}/2) \sin\theta \cos\phi, \\
J_y &= (N_{\rm a}/2) \sin\theta \sin\phi, \\
J_z &= (N_{\rm a}/2) \cos\theta .
\end{aligned}$$

Substituting these into Eg. (3.22) produces the semiclassical expression for the total system energy:

$$\begin{aligned} E = {} & \delta N_{\mathrm{a}} \cos\theta + \epsilon N_{\mathrm{a}} \\ & - \frac{1}{2}|U_0|\left(\frac{N_{\mathrm{a}}^2}{4} - \frac{N_{\mathrm{a}}^2}{2}\cos\theta + \frac{N_{\mathrm{a}}^2}{4}\cos^2\theta\right) \\ & - \frac{1}{2}\alpha|U_0|\left(\frac{N_{\mathrm{a}}^2}{4} + \frac{N_{\mathrm{a}}^2}{2}\cos\theta + \frac{N_{\mathrm{a}}^2}{4}\cos^2\theta\right) \\ & - 2\beta|U_0|\left(\frac{N_{\mathrm{a}}^2}{4}\sin^2\theta - \frac{N_{\mathrm{a}}}{2}\right) - \beta|U_0|\frac{N_{\mathrm{a}}^2}{4}\sin^2\theta\cos 2\phi \\ & - \gamma|U_0|N_{\mathrm{a}}^2\sin\theta\cos\phi. \end{aligned} \tag{3.23}$$

Beyond this point the not odd-relative parity solution, though solvable for example using Mathematica, becomes much more complicated algebraically than the odd-relativity case. Moreover, it calculates $\left\langle \hat{n}_p/\hat{N}_{\mathrm{a}} \right\rangle$ which in the even-relative parity case is not equal to ε_p anyway, because of the off-diagonal long range order appearing in $\hat{\rho}$. For these reasons and because the odd-relative parity formulation will be used extensively in our results, Sec. 3.3, we next specialize to $|p\rangle$, $|q\rangle$ having odd-relative parity.

Odd-relative parity

When $|p\rangle$ and $|q\rangle$ have odd-relative parity, $\gamma = 0$ so that E is minimized when $\cos 2\phi = 1$. Define $\eta = \cos\theta$ and divide by N_{a} to get the energy per particle of the system: [2]

$$\begin{aligned} \frac{E}{N_{\mathrm{a}}} = {} & \eta^2\frac{N_{\mathrm{a}}|U_0|\,(6\beta - \alpha - 1)}{8} \\ & + \eta\frac{N_{\mathrm{a}}|U_0|(1-\alpha) + 4\delta}{4} \\ & + \frac{N_{\mathrm{a}}|U_0|\,(6\beta + \alpha + 1)}{8} + \epsilon + \beta|U_0|. \end{aligned} \tag{3.24}$$

[2] This result differs from [37], Eq. (38), and I believe their form is incorrect: the $2 + 2\alpha$ in their second to last term should be changed to $1/2 + \alpha/2$. If one plugs in $\alpha = 3/4$ and $\beta = 1/2$, the values for the nominally-widthed 0th and 1st harmonic oscillator states, Eq. (3.18), and makes the substitutions described in footnote 1, my formulation reduces correctly to [37], Eq. (21); their uncorrected form does not. Footnote 3 has a similar critique of [37], Eq. (39), and discusses the ramifications for their central conclusions.

Whereas for arbitrary odd-relative parity $|p\rangle$ and $|q\rangle$ there exists one, two, or infinite $\eta = \eta_0 \in [-1, 1]$ that minimize E/N_a, fragmentation only occurs when η_0 is centered well enough that both $\left\langle \hat{n}_p/\hat{N}_\mathrm{a} \right\rangle = 1/2 - \eta_0/2$ and $\left\langle \hat{n}_q/\hat{N}_\mathrm{a} \right\rangle = 1/2 + \eta_0/2$ are $\sim O(1)$ rather than one being $\sim O(1)$ and one being $\sim O(1/N_\mathrm{a})$. This requires E/N_a have positive curvature, $6\beta - \alpha - 1 > 0$, so that η_e, the value of η that extremizes E/N_a, exists and is found at a minima. Mathematically, $\eta_e \in \mathbb{R}$, but fragmentation additionally requires that $|\eta_e| < 1$.

η_e is found by taking the derivative of (3.24) with respect to η, setting it equal to 0, and solving:

$$\eta_e = -\frac{D_1}{2D_2} = -\frac{1 - \alpha + \frac{4\delta}{N_\mathrm{a}|U_0|}}{6\beta - \alpha - 1}, \tag{3.25}$$

where

$$D_2 = \frac{N_\mathrm{a}|U_0|\,(6\beta - \alpha - 1)}{8},$$
$$D_1 = \frac{N_\mathrm{a}|U_0|(1 - \alpha) + 4\delta}{4},$$

are the η^2 and η^1 coefficients of E/N_a, respectively. The fragmentation requirement is that

$$|\eta_e| = \left| -\frac{1 - \alpha + \frac{4\delta}{N_\mathrm{a}|U_0|}}{6\beta - \alpha - 1} \right| < 1. \tag{3.26}$$

The initial minus sign can be dropped, and the denominator can pulled out of the absolute value because the curvature requirement enforces it be positive:

$$\left| 1 - \alpha + \frac{4\delta}{N_\mathrm{a}|U_0|} \right| < 6\beta - \alpha - 1. \tag{3.27}$$

This can be broken into two cases, simplified to:

$$\frac{2\delta}{N_\mathrm{a}|U_0|} < 3\beta - 1, \qquad \text{if} \quad \tfrac{2\delta}{N_\mathrm{a}|U_0|} \geq \tfrac{\alpha - 1}{2},$$
$$\frac{2\delta}{N_\mathrm{a}|U_0|} > \alpha - 3\beta, \qquad \text{if} \quad \tfrac{2\delta}{N_\mathrm{a}|U_0|} < \tfrac{\alpha - 1}{2}.$$

It makes intuitive sense that whether a BEC fragments or remains pure depends on the ratio $N_\mathrm{a}|U_0|/(2\delta)$. The numerator $N_\mathrm{a}|U_0|$ is proportional to the interaction energy per

particle, and specifically equals the per particle interaction energy if all atoms occupied ϕ_p. The denominator $2\delta = h_{qq} - h_{pp}$ is the per particle energy penalty paid for fragmentation. The weighted differences of α, β, and 1 account for the details of the scattering allowed under the specific model. Changing these into equalities defines N_{f}, the atom number below which the ground state is pure and above which the ground state is fragmented:

$$\begin{aligned} N_{\mathrm{f}} &= \frac{2\delta}{|U_0|\,(3\beta - 1)}, \qquad \text{if} \qquad \frac{4\delta}{N_{\mathrm{f}}|U_0|} \geq \alpha - 1, \\ N_{\mathrm{f}} &= \frac{2\delta}{|U_0|\,(\alpha - 3\beta)}, \qquad \text{if} \qquad \frac{4\delta}{N_{\mathrm{f}}|U_0|} < \alpha - 1. \end{aligned} \tag{3.28}$$

In general, the top condition applies when $\delta > 0$, which for example more or less holds for nominally-ordered harmonic oscillator states when the variational widths both are on the same order of magnitude, including the nominal width case. We will use this throughout our results, Sec. 3.3. The bottom condition generally applies when $\delta < 0$, for harmonic trap states typically either because the variational parameters are of widely different orders of magnitude or because the labeling of the states has been switched from nominal.

For completeness, when fragmentation is energetically unpreferred, η_0 equals whichever of ± 1 minimizes E/N_{a}. In the special case where $6\beta - \alpha - 1, D_2 < 0$ and $\eta_e = D_1 = 0$, $\eta_0 = \pm 1$ are equally energetically preferred. When $D_2 = 0$ and $D_1 = 0$, E/N_{a} lacks η dependence entirely so all values in $[-1, +1]$ are equally energetically favorable. This is summarized as

$$\eta_0 = \begin{cases} \eta_e, & D_2 > 0 \,\&\, |\eta_e| \leq 1, \\ -1, & (D_2 > 0 \,\&\, \eta_e < -1) \text{ or } (D_2 \leq 0 \,\&\, D_1 > 0), \\ +1, & (D_2 > 0 \,\&\, \eta_e > +1) \text{ or } (D_2 \leq 0 \,\&\, D_1 < 0), \\ \text{both of } \{-1, +1\}, & D_2 < 0 \,\&\, D_1 = 0, \\ \text{any of } [-1, +1], & D_2 = 0 \,\&\, D_1 = 0, \end{cases} \tag{3.29}$$

with many-body ground state fractional occupation given by [3]

$$\frac{n_p}{N_\mathrm{a}} = \begin{cases} \frac{3\beta-\alpha}{6\beta-\alpha-1} + \frac{2\delta}{(6\beta-\alpha-1)N_\mathrm{a}|U_0|}, & D_2 > 0 \,\&\, |\eta_e| \leq 1, \\ 1, & (D_2 > 0 \,\&\, \eta_e < -1) \text{ or } (D_2 \leq 0 \,\&\, D_1 > 0), \\ 0, & (D_2 > 0 \,\&\, \eta_e > +1) \text{ or } (D_2 \leq 0 \,\&\, D_1 < 0), \\ \text{both of } \{0,1\}, & D_2 < 0 \,\&\, D_1 = 0, \\ \text{any of } [0,1], & D_2 = 0 \,\&\, D_1 = 0. \end{cases} \tag{3.30}$$

Here, specifically because the odd-relative parity between the single-particle states empirically eliminates the off-diagonal elements in the SPDM, $\varepsilon_p = \left\langle \hat{n}_p/\hat{N}_\mathrm{a} \right\rangle$ and $\varepsilon_q = \left\langle \hat{n}_q/\hat{N}_\mathrm{a} \right\rangle$, which in the semiclassical approximation are equal to n_p/N_a and n_q/N_a, respectively. Though we haven't rigorously proven it, for even-relative parity in every case we have examined with our model the off-diagonal SPDM elements are non-zero so that $\varepsilon_i \neq \left\langle \hat{n}_i/\hat{N}_\mathrm{a} \right\rangle$ and the relationship between ε_i and η differs. When n_p/N_a equals one of $\{0, 1\}$, the many-body ground state is pure: $n_p/N_\mathrm{a} = 1$ means $|p\rangle$ is occupied, $n_q/N_\mathrm{a} = 0$ means $|q\rangle$ is occupied.

[3] Similarly to footnote 2 for Eq. 3.24, this result differs from [37], Eq. (39), and I believe their form is incorrect: the β in the numerator of their last term should be changed to a 1. If one plugs in $\alpha = 3/4$ and $\beta = 1/2$, the values for the nominally-widthed 0th and 1st harmonic oscillator states, Eq. (3.18), and makes the substitutions described in footnote 1, my formulation reduces correctly to [37], Eq. (24); their uncorrected form does not. If I am correct, this may impact one of their central conclusions, that fragmentation is not possible in an arbitrary but practical potential.

That said, even before the algebraic correction is applied I think this claim might be overstated. Specifically, consider a potential designed to have orbitals with $\alpha = 3\beta - \Delta$, where $\Delta \ll 1$ such that $\alpha = 3\beta - \Delta \geq 2\beta - 1$, satisfying the inequality stated below [37], Eq. (40). In this case the first term of [37], Eq. (39), will be proportional to Δ so can be made negligibly small. Then, barring additional undescribed constraints on the orbitals that may exist that I have not accounted for, for $N_\mathrm{a}|U_0|/\epsilon \sim 1$ significant fragmentation will be observed, independent of the value of β. Finally, the algebraic correction I suggest further reduces n_0/N_a for $\beta \gg 1$ such that fragmentation is easier to achieve if the correction stands.

It may turn out this is an academic discussion only. I can conceive of orbital pairs that satisfy $\alpha \approx 3\beta$, and think potentials that enable them are theoretically possible, though am not sure if they are practically achievable.

The corresponding equilibrium energy is

$$\frac{E_0}{N_\mathrm{a}} = \epsilon + \beta|U_0| - \begin{cases} \frac{N_\mathrm{a}|U_0|(9\beta^2-\alpha)+2\delta(1-\alpha)+4\frac{\delta^2}{N_\mathrm{a}|U_0|}}{2(6\beta-\alpha-1)}, & D_2 > 0 \,\&\, |\eta_e| \leq 1, \\ \left(\frac{N_\mathrm{a}|U_0|}{2}+\delta\right), & (D_2 > 0 \,\&\, \eta_e < -1) \text{ or } (D_2 \leq 0 \,\&\, D_1 > 0), \\ \left(\frac{N_\mathrm{a}|U_0|\alpha}{2}-\delta\right), & (D_2 > 0 \,\&\, \eta_e > +1) \text{ or } (D_2 \leq 0 \,\&\, D_1 < 0), \\ \frac{N_\mathrm{a}|U_0|3\beta}{2}, & D_2 \leq 0 \,\&\, D_1 = 0, \end{cases} \tag{3.31}$$

where the top case describes the fragmented state.

3.2.4 1D harmonic potential

Our vertically aligned, long, skinny cigar-shaped magnetic trap is harmonic with axial and radial trapping frequencies $\omega_z = 2\pi\times 50\,\mathrm{Hz}$ and $\omega_r = 2\pi\times 3.5\,\mathrm{kHz}$, respectively, producing an aspect ratio of $\omega_r/\omega_z = 70$. As outlined in Sec. 2.1.1, our change in B_0 before collecting the data in Ch. 2 changed ω_r from the $2\pi\times 3.0\,\mathrm{kHz}$ value it had during the data collection for Ref. [16]. Because we started our theory this way and because the exact value does not affect the essential physics our model seeks to illustrate, all of the theory in this chapter describing our system is carried out with $\omega_r = 2\pi\times 3.0\,\mathrm{kHz}$, which sets the aspect ratio to 60 and N_c to 360, different from the experimental values in Ch. 2: 70 and 330, respectively.

ω_r plays a small role because, as a simplification, the theory we have developed to apply to our system is truly 1D, rather than quasi-1D: We integrate the radial degrees of freedom out of the two-body interaction Hamiltonian, Eq. (3.1). First we separate $\phi(\vec{r}) = \phi(x,y,z)$ into $\phi_r(x,y)\phi(z)$, where

$$\phi_r(x,y) = \frac{1}{\pi^{1/2}\sigma_{r,0}^2}\exp\left(-\frac{x^2}{2\sigma_{r,0}^2}-\frac{y^2}{2\sigma_{r,0}^2}\right) \tag{3.32}$$

is the ground state of the radial harmonic oscillator, normalized to have $\int \mathrm{d}x\mathrm{d}y\,|\phi_r(x,y)|^2 = 1$, and $\sigma_{x,0} = \sigma_{y,0} = \sigma_{r,0}$. Integrating $\hat{H}$ over the radial coordinates x and y and dropping the resulting constant $\hbar\omega_r$ term because it does not affect the dynamics leaves the 1D $\hat{H}$ with the same written form as in the 3D case.

Now, however, only scattering between axial modes is considered, so $\{i, j, k, l\}$ explicitly

label the axial single-particle states only. In the position representation, the single-particle kinetic and trap potential operators become

$$\hat{t} = -\frac{\hbar^2}{2m}\frac{\partial^2}{\partial z^2} \tag{3.33}$$

and

$$\hat{u} = \frac{1}{2}m\omega_z^2 z^2. \tag{3.34}$$

The interaction terms, Eq. (3.4), are modified slightly to

$$V_{ijkl} = g_{1\mathrm{D}} \int \mathrm{d}z\, \phi_i^*(z)\phi_j^*(z)\phi_k(z)\phi_l(z), \tag{3.35}$$

where $g_{1\mathrm{D}} = 2\hbar\omega_r a$ is the quasi-1D interaction coupling coefficient. Because ours is a true 1D theory, the only role of ω_r is scaling $g_{1\mathrm{D}}$. A direct consequence is that the collapse criterion, $N_\mathrm{c} \approx 0.76\sigma_{r,0}/|a| \approx 330$, Eq. (1.9), is not derivable from our model and requires an independent quasi-1D calculation [10].

As a concrete example to begin the analysis, consider the two single-particle modes

$$\phi_0(z) = \frac{1}{\pi^{1/4}(\lambda_0\sigma_{z,0})^{1/2}} \exp\left(-\frac{z^2}{2(\lambda_0\sigma_{z,0})^2}\right) \tag{3.36}$$

$$\phi_1(z) = \frac{2^{1/2}z}{\pi^{1/4}(\lambda_1\sigma_{z,0})^{3/2}} \exp\left(-\frac{z^2}{2(\lambda_1\sigma_{z,0})^2}\right), \tag{3.37}$$

the harmonic potential ground and first excited states: $p = 0$ and $q = 1$, respectively. Here $\sigma_{z,0} = (\hbar/m\omega_z)^{1/2} \approx 6\,\mu$m is the axial oscillator length, and λ_i is a dimensionless variational parameter scaling the width of ϕ_i. $\lambda_i = 1$ sets ϕ_i to its nominal width, which will hold for Secs. 3.3.1, 3.3.2, and 3.3.3. However, because this constraint will be dropped in Sec. 3.3.4 when we calculate energy landscapes within variational width space, we continue carrying the λ_is in the analytic expressions. The corresponding many-body states are

$$|\Psi_i\rangle = \sum_{n_1=0}^{N_\mathrm{a}} C_{i;n_1} |n_1\rangle\,. \tag{3.38}$$

Using ϕ_0 and ϕ_1 to construct $\hat{H}$, the kinetic and trap potential terms, Eq. (3.17), evaluate

to

$$\begin{aligned} h_{00} = \langle 0|\hat{t} + \hat{u}|0\rangle &= \frac{1}{4}\hbar\omega_z(\lambda_0^2 + \lambda_0^{-2}) \\ h_{11} = \langle 1|\hat{t} + \hat{u}|1\rangle &= \frac{3}{4}\hbar\omega_z(\lambda_1^2 + \lambda_1^{-2}). \end{aligned} \tag{3.39}$$

The scattering coefficients are

$$\begin{aligned} V_{0000} \equiv -|U_0| &= -\hbar\omega_r\sqrt{\frac{2}{\pi}}\frac{|a|}{\sigma_{z,0}}\frac{1}{\lambda_0} \\ V_{1111} \equiv -\alpha|U_0| &= -\frac{3\lambda_0}{4\lambda_1}|U_0| \\ V_{0011} \equiv -\beta|U_0| &= -\frac{2^{1/2}}{\left(1+\left(\frac{\lambda_1}{\lambda_0}\right)^2\right)^{3/2}}|U_0| \\ V_{0001} = V_{0111} = \gamma &= 0. \end{aligned} \tag{3.40}$$

This makes $\hat{H}$ is expressible as

$$\begin{aligned} \hat{H} &= h_{00}\hat{n}_0 + h_{11}\hat{n}_1 \\ &\quad - \frac{1}{2}|U_0|\hat{n}_0\left(\hat{n}_0 - 1\right) - \frac{1}{2}\alpha|U_0|\hat{n}_1\left(\hat{n}_1 - 1\right) \\ &\quad - 2\beta|U_0|\hat{n}_0\hat{n}_1 \\ &\quad - \frac{1}{2}\beta|U_0|\left(\hat{a}_0^\dagger\hat{a}_0^\dagger\hat{a}_1\hat{a}_1 + \hat{a}_1^\dagger\hat{a}_1^\dagger\hat{a}_0\hat{a}_0\right). \end{aligned} \tag{3.41}$$

Diagonalizing $\hat{H}$ yields the many-body energy spectrum $\{E_i\}$ and eigenstates $\{|\Psi_i\rangle\}$, each represented by its $\{C_{i;n_1}\}$. Examples of these representations, for the many-body ground states with our system parameters and $N_\mathrm{a} = N_\mathrm{f}/2$, N_f, and $2N_\mathrm{f}$ are displayed in Fig. 3.1. $\{C_{0;n_1}\}$ is used to create the ground state SPDM, Eq. (3.20),

$$\hat{\rho} = \frac{1}{N_\mathrm{a}}\begin{pmatrix} \langle\hat{a}_0^\dagger\hat{a}_0\rangle & \langle\hat{a}_0^\dagger\hat{a}_1\rangle \\ \langle\hat{a}_1^\dagger\hat{a}_0\rangle & \langle\hat{a}_1^\dagger\hat{a}_1\rangle \end{pmatrix}, \tag{3.42}$$

which is diagonalized to determine the degree of fragmentation. If both $\varepsilon_i \sim O(1)$ then the ground state is fragmented, otherwise it is pure.

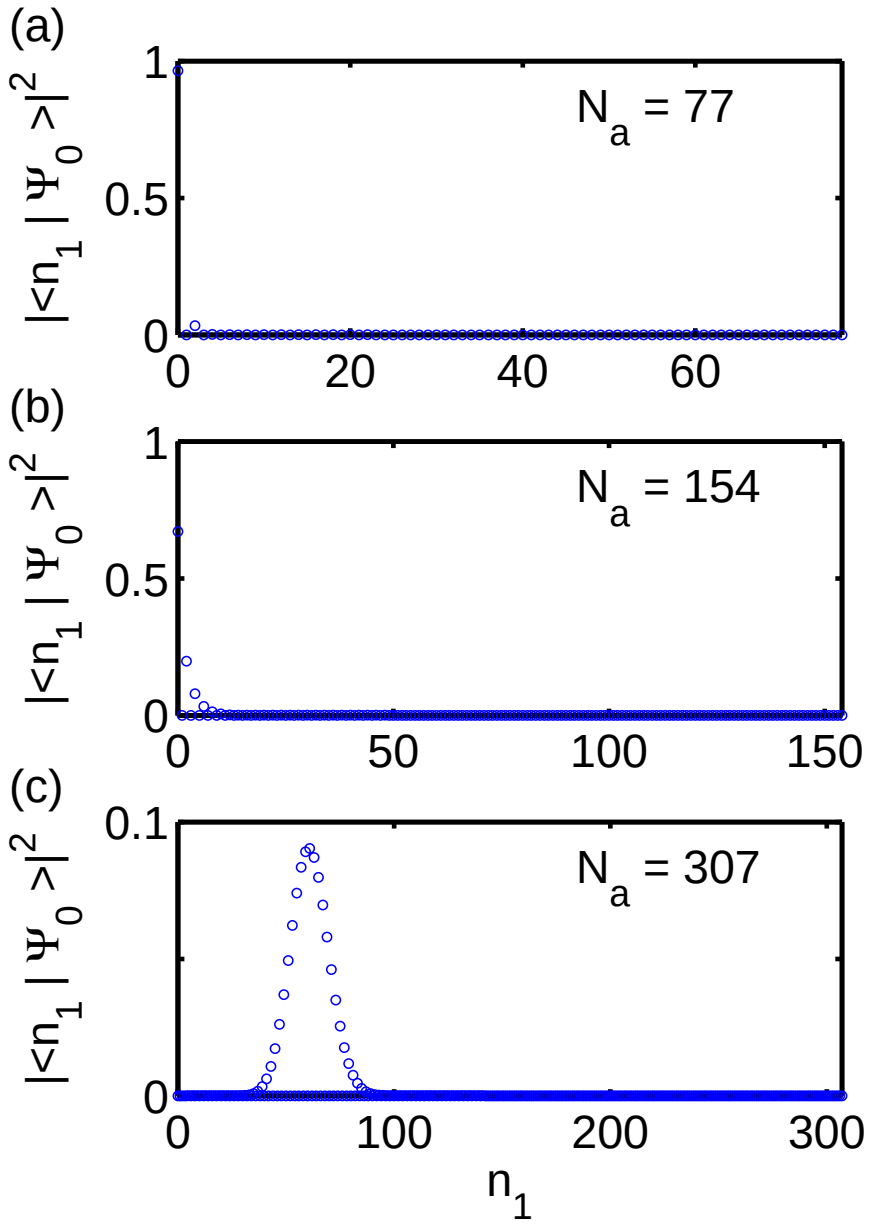

Figure 3.1: Many-body ground state decomposition $\{C_{0;n_1}\}$ when N_a atoms are allowed to scatter within single-particle harmonic trap states 0 and 1 at (a) $N_a = 77 \approx N_f/2$, (b) $N_a = 154 \approx N_f$, and (c) $N_a = 307 \approx 2N_f$, as a function of n_1, the occupation number basis state index. For $N_a \leq N_f$, (a) and (b), the atoms macroscopically occupy ϕ_0. As N_a increases above N_f, $\langle \hat{n}_1 \rangle$ begins to increase. Also note that within each plot, every other term has value 0.

Using Eq. (3.21), we get

$$\epsilon \equiv (h_{11} + h_{00})/2 = \frac{1}{8}\hbar\omega_z\left[3(\lambda_1^2 + \lambda_1^{-2}) + (\lambda_0^2 + \lambda_0^{-2})\right] \tag{3.43}$$

$$\delta \equiv (h_{11} - h_{00})/2 = \frac{1}{8}\hbar\omega_z\left[3(\lambda_1^2 + \lambda_1^{-2}) - (\lambda_0^2 + \lambda_0^{-2})\right], \tag{3.44}$$

which finishes defining the semiclassical approximate equations for E, Eq. (3.22); N_f, Eq. (3.28); $\varepsilon_0 = n_0/N_\mathrm{a}$, Eq. (3.30); and E_0/N_a, Eq. (3.23); for variationally-widthed ϕ_0 and ϕ_1. Nominal width results are found by setting $\lambda_0 = 1$ and $\lambda_1 = 1$.

Lastly, for $\lambda_i = 1$, we can recast N_a in terms of the per particle interaction energy, to which it is directly proportional:

$$N_\mathrm{a}|V_{0000}|_{\lambda_0=1} = N_\mathrm{a}2\hbar\omega_r|a|\int \mathrm{d}z\ |\phi_0(z)|^4\Big|_{\lambda_0=1} = \sqrt{\frac{2}{\pi}}\frac{\hbar\omega_r N_\mathrm{a}|a|}{\sigma_{z,0}}. \tag{3.45}$$

Ratioing this to the axial mode energy splitting further recasts N_a in terms of an effective coupling strength:

$$\chi_\mathrm{int} = \frac{N_\mathrm{a}|V_{0000}|_{\lambda_0=1}}{\hbar\omega_z} = \sqrt{\frac{2}{\pi}}\frac{\omega_r}{\omega_z}\frac{N_\mathrm{a}|a|}{\sigma_{z,0}} = \sqrt{\frac{2}{\pi}}\sqrt{\frac{\omega_r}{\omega_z}}\frac{N_\mathrm{a}|a|}{\sigma_{r,0}}. \tag{3.46}$$

χ_int is the nominal-width equivalent of $N_\mathrm{a}|U_0|/(2\delta)$ which defines whether two orbitals with odd-relative parity fragment or not, Eq. (3.28), with fragmentation generally expected for $\chi_\mathrm{int} \gtrsim 1$. As with N_c, if χ_int becomes too large the atomic ensemble will be unstable against collapse, which for our experimental parameters and ϕ_0 and ϕ_1 happens at $\chi_\mathrm{int,c} \approx 4.7$.

These tools laid out, we next describe our theory results.

3.3 Results

3.3.1 $N_\mathrm{f} < N_\mathrm{c}$ for 1D harmonic oscillator states 0 and 1

Our goal being to show that fragmentation is energetically likely for $N_\mathrm{a} < N_\mathrm{c}$, we begin by calculating the SPDM eigenvalues for our two single-particle states (3.36, 3.37), nominally-widthed so that $\lambda_0 = \lambda_1 = 1$, while we increase N_a from 1 to just over N_c. In this case

$h_{00} = \hbar\omega_z/2$, $h_{11} = \hbar\omega_z 3/2$, $\epsilon = \hbar\omega_z$, $\delta = \hbar\omega_z/2$, $\alpha = 3/4$, $\beta = 1/2$, $\gamma = 0$, and $|U_0| = \hbar\omega_r(2/\pi)^{1/2}(|a|/\sigma_{z,0}) \approx \hbar\omega_z\, 0.0153$. Plugging these into Eq. (3.41) for each N_a we construct $\hat{H}$, and then diagonalize it. Examples of the many-body ground state, represented in the occupation number basis state by $\{C_{0;n_1}\}$, are plotted in Fig. 3.1. From these plots it is visually clear that as N_a increases above N_f, $\left\langle \hat{n}_1/\hat{N}_\mathrm{a} \right\rangle$ begins near 0 (b), and increases to $\sim O(1)$ (c). Conversely $\left\langle \hat{n}_0/\hat{N}_\mathrm{a} \right\rangle = 1 - \left\langle \hat{n}_1/\hat{N}_\mathrm{a} \right\rangle$ begins near 1 and decreases but remains $\sim O(1)$.

Determining the degree of fragmentation for a system with two single-particle states requires the two additional SPDM terms, $\left\langle \hat{a}_0^\dagger \hat{a}_1 \right\rangle$ and $\left\langle \hat{a}_1^\dagger \hat{a}_0 \right\rangle$. However, looking closely at the $\{C_{0;n_1}\}$ at all three values of N_a, every other term equals 0. Mathematically, this causes the off-diagonal SPDM terms to be identically 0 so that the system does not exhibit off-diagonal long range order and $\varepsilon_0 = n_0/N_\mathrm{a}$ and $\varepsilon_1 = n_1/N_\mathrm{a}$. We empirically observe this when the single-particle state pairs have odd-relative parity.

Fig. 3.2 shows both the exact fragmentation parameters, ε_0 and ε_1, and the semiclassically approximated values, n_0/N_a and n_1/N_a, plotted as N_a rises from 0 to greater than N_c. Also shown are N_c [10] and the semiclassically approximated N_f, the vertical blue dashed and red dashed lines, respectively. Two important conclusions should be drawn from this figure. First, a fragmented ground state exists for $N_\mathrm{f} < N_\mathrm{a} < N_\mathrm{c}$. Such fragmented condensates in our 1D harmonic potential are metastable against collapse, unlike those in the 3D harmonic potential [37]; because they are ground states they are stable against variations in occupation number, unlike those in [38]. Second, the semiclassical approximation does a fine job predicting the SPDM eigenvalues and N_f, the atom number above which $\varepsilon_0, \varepsilon_1 \sim O(1)$. The slight discrepancy at $N_\mathrm{a} \sim N_\mathrm{f}$ is due to finite N_a smoothing out the transition from a pure to fragmented ground state in the exact solution [37].

3.3.2 N_f vs. N_c for harmonic oscillator states j and $j + \Delta j$ for odd Δj

Knowing that fragmentation is energetically favored in scattering between the 0 and 1 oscillator states for N_a stable against collapse, we next consider how many other trap state pairs satisfy this condition. Extending our model requires appropriately changing h_pp, h_qq, U_0, α, β, γ, δ, and ϵ, but otherwise the method is the same. Because the semiclassical

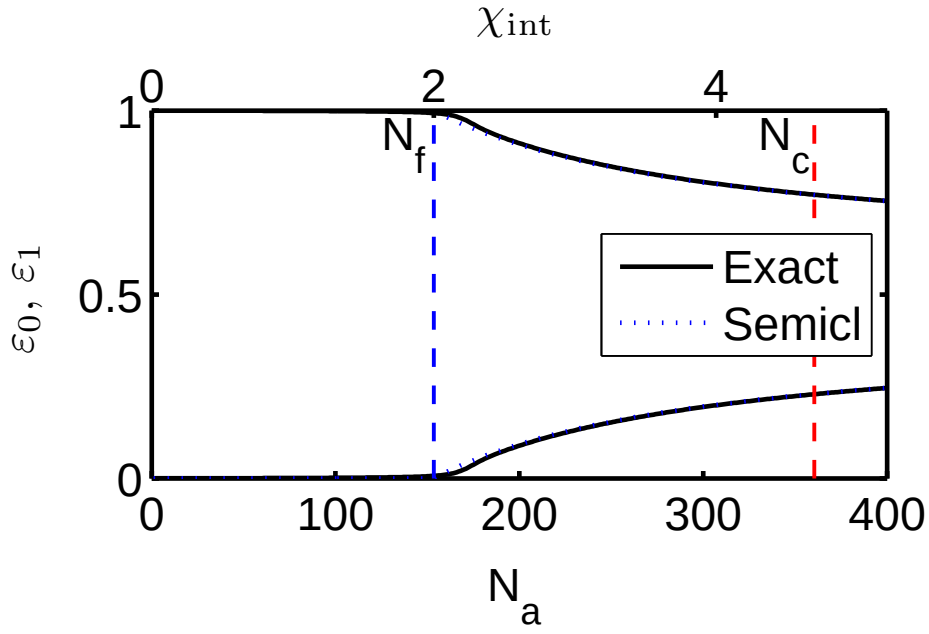

Figure 3.2: Many-body ground state SPDM eigenvalues for $1 \leq N_a \lesssim N_c$ when atoms are allowed to scatter amongst single-particle harmonic trap states 0 and 1, exact (solid black lines) and using the semiclassical approximation (dotted blue lines). The vertical dashed lines indicate N_c (red) and the semiclassically predicted N_f (blue). Fragmentation is clearly predicted for $N_a < N_c$, which means these condensates should be stable against collapse. The agreement between the exactly solved and semiclassically approximated lines demonstrates this is an excellent approximation for our purposes.

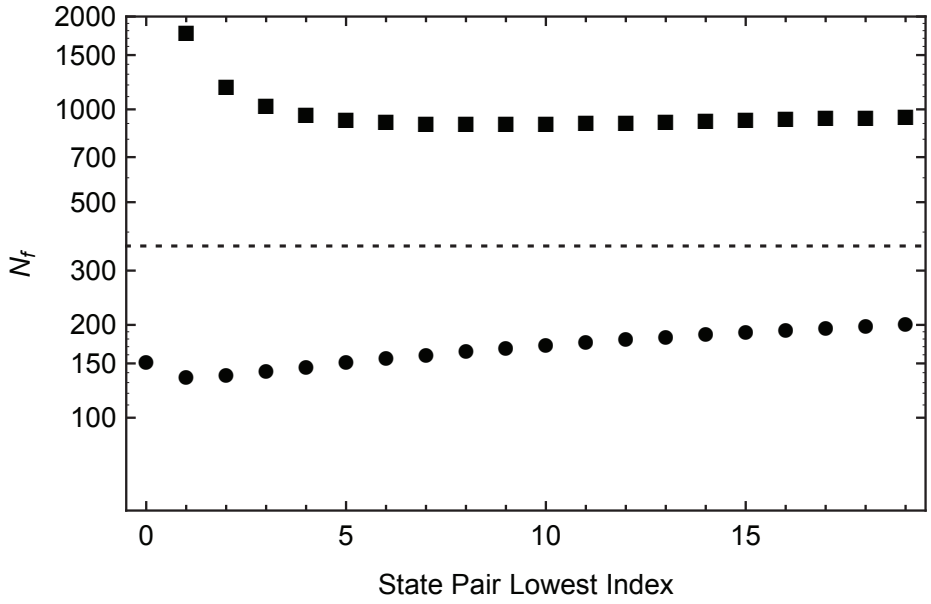

Figure 3.3: Semiclassically predicted N_f values for nominally-widthed one-apart single-particle state pairs, e.g. 0 and 1, 1 and 2, (•) and three-apart state pairs, e.g. 1 and 4, 2 and 5, (■) vs the lower index of the state pair. The horizontal dotted line indicates N_c for our system parameters. Many adjacent state pairs have $N_\mathrm{f} < N_\mathrm{c}$, so when the Hilbert space is limited only to them they have stable fragmented ground states. For our parameters, three-apart state pairs all have $N_\mathrm{f} > N_\mathrm{c}$ so should not fragment stably. Nominally-widthed single-particle states 0 and 3 overlap insufficiently for fragmentation to occur. Similar curves can be generated for higher odd state separations (odd-relative parity), but not between states with even state separation (even-relative parity) where fragmentation does not empirically occur.

approximation predicts N_f fairly accurately and additionally removes the arbitrariness required of the exact solution in selecting an appropriate threshold for ε_1 to rise above before being considered $\sim O(1)$, we use it in this calculation.

We categorize the state pairs according to the difference between their oscillator state index: one-apart (adjacent), e.g. 0 and 1, 1 and 2, three-apart, e.g. 0 and 3, 1 and 4, five-apart, and so on. Odd index separations correspond to odd-relative parity between the state pairs, even index separations correspond to even-relative parity. In Fig. 3.3 we plot N_f for our system parameters and different state combinations. The horizontal dotted line indicating N_c shows that all of the adjacent state pairs we plot have $N_\mathrm{f} < N_\mathrm{c}$ and that

all of the three-apart state pairs have $N_f > N_c$, except for 0 and 3 which do not overlap sufficiently to fragment, i.e. $\beta < 1/3$ see Eq. (3.28). We calculated N_f for five- and seven-apart state pairs and observe that the tendency continues toward finite but higher N_f, with lower indexed pairs overlapping insufficiently to fragment.

The even-relative parity state pair case is simpler: fragmentation does not occur between even-relative parity state pairs, at least not in any cases we modeled. The semiclassical approximation Eq. for n_0/N_a is solvable but with a significantly more complicated form. Even then it does not equal either of the SPDM eigenvalues because in general the off-diagonal SPDM terms are non-zero. The exact solution must be used which in all cases we analyzed predicts a pure ground state. A rigorous proof requires a closed form analytic solution for the overlap integrals in V_{ijkl} with arbitrary indices, which we lack [4].

3.3.3 Excitation energy spectra

At the heart of whether a bosonic sample fragments or has a conventional Bose-Einstein condensed ground state is the degree to which the ground state is degenerate with other states [28]. For understanding our experimental results which occur at $T > 0$ after evaporating directly under attractive interactions, at issue is the degree to which more generally all the many-body states abide with neighboring nearly degenerate states.

To probe this, we use our two single-particle state scattering model to solve for the complete many-body per particle excitation energy spectra. Specifically, for a given state pair, at each N_a we diagonalize $\hat{H}$ to get the entire set of $N_a + 1$ many-body eigenenergies, $\{E_i\}$. Subtracting off E_0 from each and dividing by N_a produces $\{\Delta\mu_{tot,i}\}$, the per particle excitation energy spectrum. We then track how the $\{\Delta\mu_{tot,i}\}$ depend on changing N_a.

As a first example, consider $\{\Delta\mu_{tot,i}\}$ for two-body scattering between single-particle trap states 0 and 1, the lowest energy 16 of which are shown in Fig. 3.4. As is characteristic for mean field interactions, the $\{\Delta\mu_{tot,i}\}$ decrease like $\sim O\left(N_a^{-1}\right)$ for $N_a \ll N_f$, where $N_a = N_f$ is indicated by the vertical dashed blue line. The $\{\Delta\mu_{tot,i}\}$ dependence on N_a disappears entirely for $N_a \gg N_f$. The most interesting feature of this figure is at $N_a \gtrsim N_f$ where adjacent pairs of excitation energies converge to numerical degeneracy at a rate much faster

[4] Solutions are offered in [43, 44] but ended up being too complicated to decipher and implement into code.

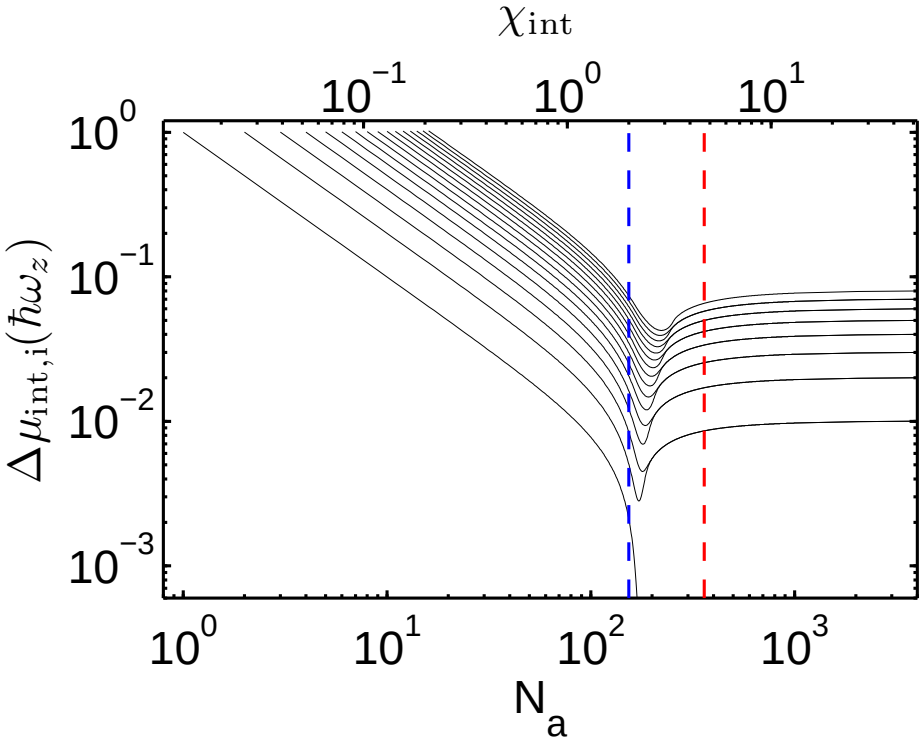

Figure 3.4: Per particle many-body excitation energy spectra dependence on $N_{\rm a}$ for scattering amongst single-particle 1D trap states 0 and 1. The 16 lowest energy many-body excited states are plotted. The vertical dashed lines indicate $N_{\rm c}$ (red) and the semiclassically predicted $N_{\rm f}$ (blue). For $N_{\rm a} \ll N_{\rm f}$, the $\{\Delta\mu_{tot,i}\}$ decrease like $\sim O\left(N_{\rm a}^{-1}\right)$, characteristic of mean field interactions. For $N_{\rm a} \gg N_{\rm f}$, the $\{\Delta\mu_{tot,i}\}$ become independent of $N_{\rm a}$. The most interesting feature of this figure is at $N_{\rm a} \gtrsim N_{\rm f}$ where adjacent pairs of excitation energies converge to numerical degeneracy at a rate much faster than $\sim O\left(N_{\rm a}^{-1}\right)$. The bottom line, $\Delta\mu_{tot,1}$, dropping rapidly off the graph as $\mu_{tot,1}$ approaches numerical degeneracy with $\mu_{tot,0}$, indicates the rate of convergence.

than $\sim O\left(N_{\mathrm{a}}^{-1}\right)$. The rate of convergence is indicated by the bottom line, $\Delta\mu_{tot,1}$ dropping rapidly off the graph as $\mu_{tot,1}$ approaches numerical degeneracy with $\mu_{tot,0}$. $N_{\mathrm{a}} = N_{\mathrm{c}}$ is indicated in each of these plots by the red vertical dashed line.

In contrast, state pairs that are not predicted to fragment semiclassically or exactly, whose SPDM eigenvalues remain 1 and 0 independent of N_{a}, this faster than $\sim O(N_{\mathrm{a}}^{-1})$ convergence to pairwise degeneracy feature does not appear. This is the case for two-body scattering between single-particle trap states with even-relative parity, as demonstrated graphically in Fig. 3.5 for states 0 and 2. It also occurs for state pairs with odd-relative parity if the overlap of the two single-particle orbitals is insufficient, $3\beta < 1, \alpha$ depending on the sign of δ as in Eqn. 3.28. This scenario is plotted in Fig. 3.6 for states 0 and 3.

Finally, to show that this degeneracy feature should be associated with fragmentation rather than collapse, indicated in each plot by the red vertical dashed line marking $N_{\mathrm{a}} = N_{\mathrm{c}}$, contrast Fig. 3.4 with Fig. 3.7 where the 16 lowest energy $\{\Delta\mu_{tot,i}\}$ are shown for two-body scattering instead between single-particle 1D trap states 1 and 4. The red dashed vertical line showing $N_{\mathrm{a}} = N_{\mathrm{c}}$ remains stationary, and both the faster than $\sim O(N_{\mathrm{a}}^{-1})$ convergence to pairwise degeneracy and the semiclassically calculated N_{f} (blue dashed vertical line) move together to higher N_{a}.

In both instances where the pairwise degeneracy occurs, it does not occur for all many-body state pairs at the same N_{a}. Rather it starts with the bottom two states and works its way up pair by pair as N_{a} increases. At sufficiently high N_{a}, the highest energy many-body states also become pairwise degenerate. For single-particle states 0 and 1, 6% of the many-body states have a degenerate partner at $N_{\mathrm{a}} = 256$, and by $N_{\mathrm{a}} = 4096$ the fraction of degenerate many-body states tops 45% and appears to be leveling off. This pairwise degeneracy for a significant fraction of the many-body states when $N_{\mathrm{a}} \gg N_{\mathrm{f}}$ directly bears on the question of whether the many-body states created in our experiment reside in energy space in relative isolation or as members of manifolds of nearly degenerate states: even in this truncated Hilbert space, at $N_{\mathrm{a}} \approx 10^3$ like the clouds at our coldest final RF evaporation frequency, 1/3 of the many-body states have a degenerate partner. Furthermore, we expect that such many-body state degeneracy at $N_{\mathrm{a}} \gg 1$ would be dramatically increased by including more than two single-particle states in the Hilbert space, because of the $N_{\mathrm{HS}} \sim N_{\mathrm{a}}^{N_{\mathrm{m}}-1}$ dependence.

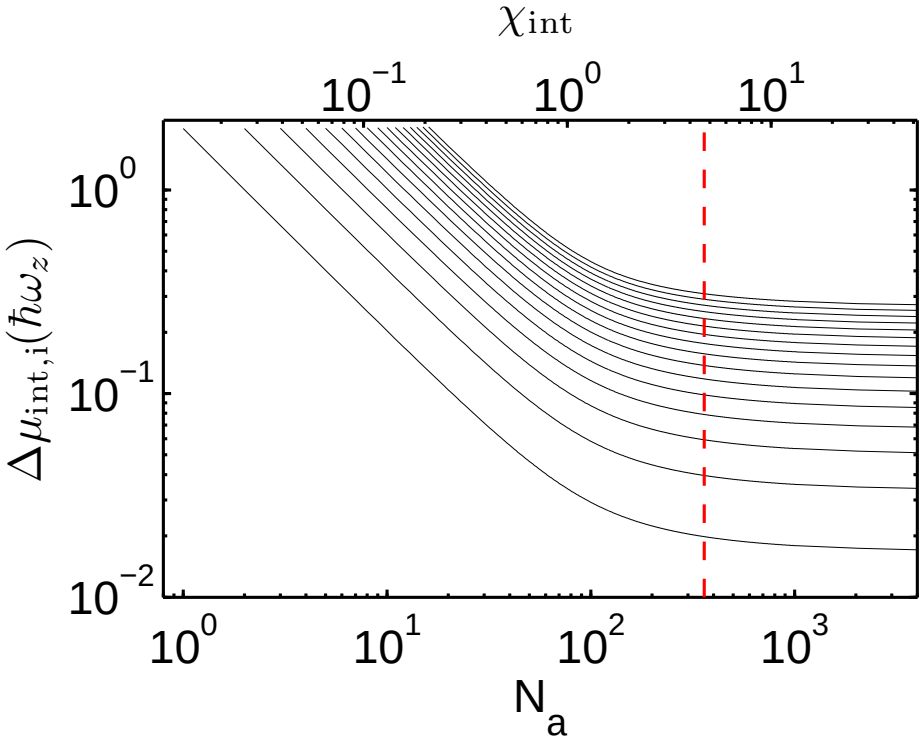

Figure 3.5: Per particle many-body excitation energy spectra as a function of $N_{\rm a}$ for scattering amongst single-particle 1D trap states 0 and 2. The 16 lowest energy many-body excited states are plotted. The vertical dashed red line indicates $N_{\rm c}$. The $\{\Delta\mu_{tot,i}\} \sim O\left(N_{\rm a}^{-1}\right)$ dependence for $N_{\rm a} \ll N_{\rm f}$, and independence, $O\left(N_{\rm a}^{0}\right)$, for $N_{\rm a} \gg N_{\rm f}$ are preserved. However in contrast with Fig. 3.4, the transition between them is smooth with the faster than $\sim O(N_{\rm a}^{-1})$ convergence to pairwise degeneracy feature not appearing. This is representative of single-particle state pairs with even-relative parity.

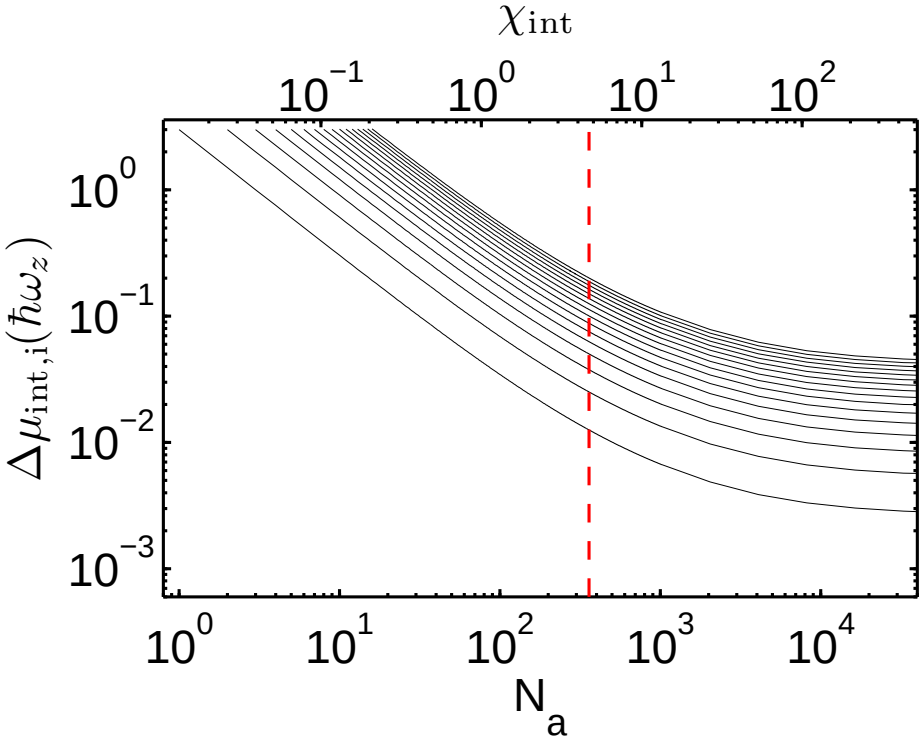

Figure 3.6: Per particle many-body excitation energy spectra dependence on $N_{\rm a}$ for scattering amongst single-particle 1D trap states 0 and 3. The 16 lowest energy many-body excited states are plotted. The vertical dashed red line indicates $N_{\rm c}$. The $\{\Delta\mu_{tot,i}\} \sim O\left(N_{\rm a}^{-1}\right)$ dependence for $N_{\rm a} \ll N_{\rm f}$, and independence, $O\left(N_{\rm a}^{0}\right)$, for $N_{\rm a} \gg N_{\rm f}$ are preserved. Like Fig. 3.5, the transition between them is smooth with the faster than $\sim O(N_{\rm a}^{-1})$ convergence to pairwise degeneracy feature not appearing. This is representative of single-particle state pairs with odd-relative parity whose overlap is insufficient for fragmentation to occur.

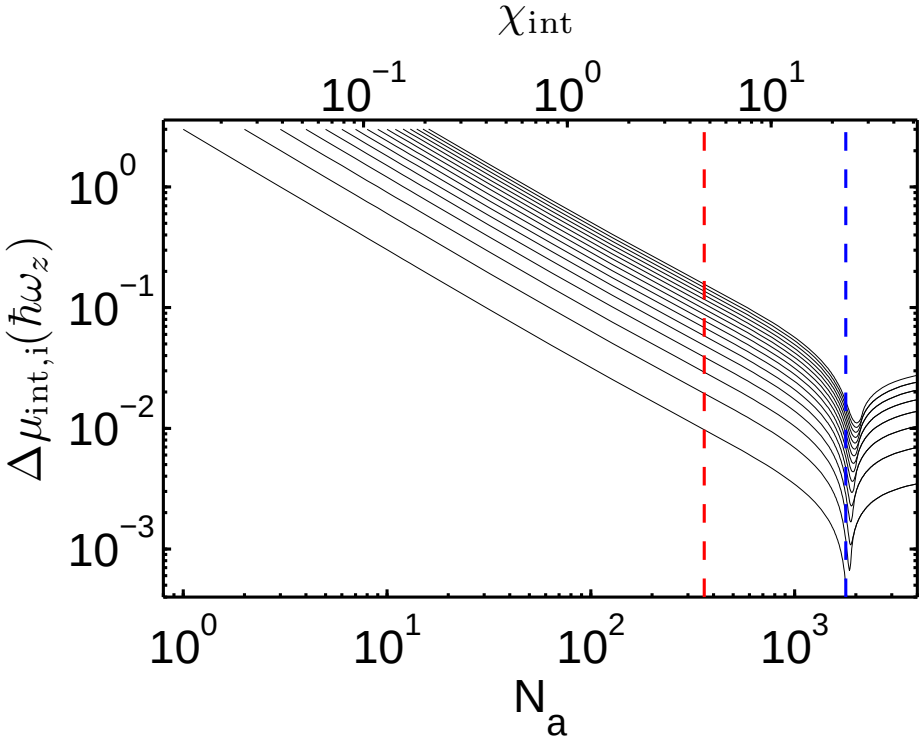

Figure 3.7: Per particle many-body excitation energy spectra dependence on $N_{\rm a}$ for scattering amongst single-particle 1D trap states 1 and 4. The 16 lowest energy many-body excited states are plotted. The vertical dashed lines indicate $N_{\rm c}$ (red) and the semiclassically predicted $N_{\rm f}$ (blue). Like Fig. 3.4, the $\{\Delta\mu_{tot,i}\} \sim O\left(N_{\rm a}^{-1}\right)$ dependence for $N_{\rm a} \ll N_{\rm f}$, independence, $O\left(N_{\rm a}^{0}\right)$, for $N_{\rm a} \gg N_{\rm f}$, and faster than $\sim O(N_{\rm a}^{-1})$ convergence to pairwise degeneracy feature are all preserved. Moreover, the mutual translation of the degeneracy feature and $N_{\rm f}$ indicate the degeneracy should be associated with fragmentation and not collapse.

3.3.4 Ground state energy landscapes with variationally-widthed single-particle states

As discussed in Sec. 3.1.1, extending our model to more than two single-particle states is computationally difficult at N_a relevant for our experiments. An alternative that captures a flavor of the many-body ground state that adding more single-particle states might produce is to follow [38]: use single-particle state pairs having independent variational widths to create energy landscapes in variational width space, then analyze the states formed at the local minima. However unlike [38], our use of exact diagonalization to find the ground state ensures its stability against variations in occupation number as well as orbital widths.

1D harmonic trap states 0 and 1

We initially apply this method to single-particle 1D harmonic trap states 0 and 1, having the same functional form as Eqs. (3.36) and (3.37) only now we let λ_0 and λ_1 vary instead of fixing them both at 1. For a given N_a and (λ_0, λ_1) pair, we follow our standard methodology: calculate h_{00}, h_{11}, U_0, α, β, δ, and ϵ; use them to construct the pentadiagonal $\hat{H}$; solve for E_0 and $|\Psi_0\rangle$ by diagonalizing $\hat{H}$; construct $\hat{\rho}$ with respect to $|\Psi_0\rangle$; diagonalize to get $\{\varepsilon_i\}$ to determine the degree of fragmentation and $\{|\varepsilon_i\rangle\}$ to get the spatial wavefunctions and density distributions of the many-body states. Rastering λ_0 and λ_1 and plotting E_0/N_a at each combination produces a ground state energy landscape for the fully interacting N_a-particle system. Local minima in this landscape correspond to Fock basis representations and (λ_0, λ_1) pairs that are energetically stable both with respect to occupation number fluctuations and orbital width fluctuations. Fig. 3.8(a) shows the energy landscape for our experimental conditions with $N_a = 307 = 2N_f = 0.85N_c$. The local minimum (white +) at $(\lambda_0, \lambda_1) = (0.30 \pm 0.01, 0.22 \pm 0.01)$ is stable against fluctuations in single-particle state widths and occupation numbers. That these both are $\ll 1$ indicates that modeling with $N_m > 2$ would significantly change the ground state description compared to using nominally-widthed single particle states. The three anomalously high points out of $\gtrsim 2000$ have non-anomalous semiclassically approximated values, so are probably erroneously caused by numerical rounding errors during matrix diagonalization. The fragmentation landscape in Fig. 3.8(b), ε_0 for the same parameters, shows that almost half of

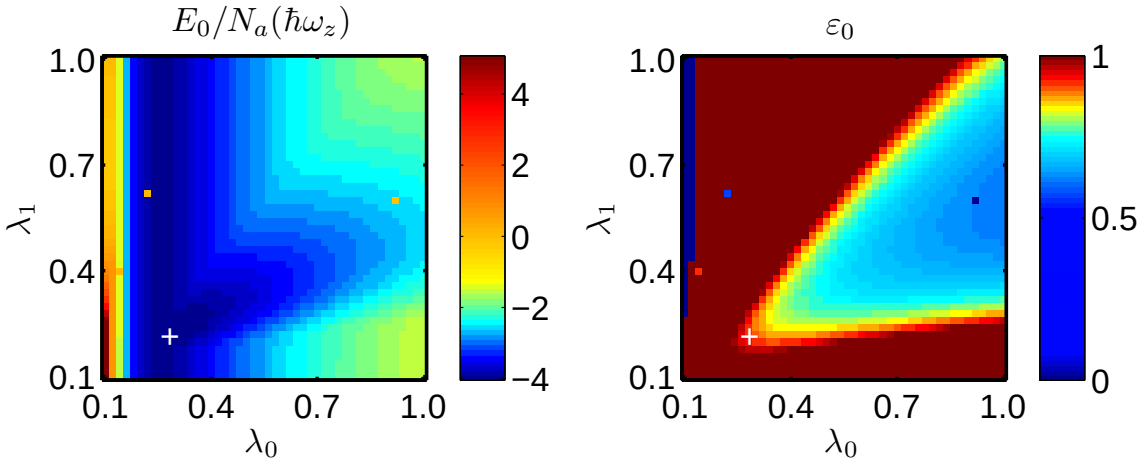

(a) (b)

Figure 3.8: Many-body ground state energy and fragmentation landscapes for $N_a = 307 = 0.85N_c$ atoms scattering amongst single-particle variationally-widthed 1D trap states 0 and 1, scaled by λ_0 and λ_1, respectively. (a) E_0/N_a vs (λ_0, λ_1). Local minima (white +) like at $(\lambda_0, \lambda_1) = (0.30 \pm 0.01, 0.22 \pm 0.01)$ where $E_0/N_a = -4.0\,\hbar\omega_z$, represent ground states that are stable against fluctuations in single-particle state widths and occupation number. For this N_a and trap state pair, the local minimum is actually the global minimum. $\lambda_0, \lambda_1 \ll 1$ indicates that increasing $N_m > 2$ would substantially change the nominal width ground state results. (b) ε_0 vs (λ_0, λ_1), overlaid with the energy minimum identified in (a). While the majority of the parameter space has a pure ground state, $\varepsilon_0 \sim O(1)$, $\varepsilon_1 = 1 - \varepsilon_0 \sim O(N_a^{-1})$ (dark red region) or $\varepsilon_1 \sim O(1)$, $\varepsilon_0 = 1 - \varepsilon_1 \sim O(N_a^{-1})$ (dark blue region), nearly half has a fragmented ground state, $\varepsilon_1 = 1 - \varepsilon_0 \sim O(1)$ (other colors), including the energy minimum (white +) where $\varepsilon_0 = 0.89$.

the parameter space exhibits some degree of fragmentation, $\varepsilon_1 = 1 - \varepsilon_0 \sim O(1)$. More intriguing, $\varepsilon_0 = 0.89$ at the energy minima found in Fig. 3.8(a) (white +), meaning the overall ground state for this system is fragmented.

3D isotropic harmonic trap states 0 and 1

As a check on our theoretical model, we use it to investigate the many body ground state for attractively interacting ^{7}Li in a 3D harmonic potential, where experiment [3] and previous theory [37] have shown that the BECs produced are pure. Using the experimental parameters given in [3], we ran the analysis for two different sets of 3D single-particle state pairs,

$$\phi_0(\vec{r}) = \frac{1}{\pi^{3/4}(\lambda_0\sigma)^{3/2}} \exp\left(-\frac{r^2}{2(\lambda_0\sigma)^2}\right), \tag{3.47}$$

$$\phi_{1a}(\vec{r}) = \frac{2^{1/2}z}{\pi^{3/4}\lambda_0\lambda_1^{3/2}\sigma^{5/2}} \exp\left(-\frac{x^2+y^2}{2(\lambda_0\sigma)^2} - \frac{z^2}{2(\lambda_1\sigma)^2}\right), \tag{3.48}$$

$$\phi_{1b}(\vec{r}) = \frac{2^{1/2}z}{\pi^{3/4}\lambda_1^{5/2}\sigma^{5/2}} \exp\left(-\frac{x^2+y^2+z^2}{2(\lambda_1\sigma)^2}\right). \tag{3.49}$$

In both analyses the single-particle ground state is the same; the excited states differ by which variational parameter scales the radial widths. This change does not substantially effect the result: [5] in both cases energetically stable fragmentation does not occur, agreeing with [3, 37].

In Figs. 3.9(a) and 3.9(b), we plot the energy and fragmentation landscape at $N_a = 950 = 0.96N_c$ using $\phi_0(\vec{r})$ and $\phi_{1a}(\vec{r})$. The energy landscape in Fig. 3.9(a) shows there are no (λ_0, λ_1) points that are local energy minima in both dimensions, a first clue that stable fragmented states do not form. Rather the white vertical dashed line marks an energy local

[5] The one notable difference between the $\phi_{1b}(\vec{r})$ and $\phi_{1a}(\vec{r})$ analyses is an additional collapse region for $\lambda_1 \to 0$ in the $\phi_{1b}(\vec{r})$ analysis. In the thermodynamic limit, taken by using the semiclassical approximation, for $\lambda_0 \gtrsim 0.38$, as $\lambda_1 \to 0$ the system undergoes a first order phase transition at $\lambda_1 \approx 0.1$, from favoring all the atoms in the single-particle trap state 0 to favoring all the atoms in the single-particle trap state 1, with no fragmented region in between. This new collapse region is caused by the increased inverse dependence of $\phi_{1b}(\vec{r})$ on λ_1 compared to that of $\phi_{1a}(\vec{r})$. That the collapse is first order and not accompanied by fragmentation is because this region has $|\eta_e| < 1$ and $D_2, 6\beta - \alpha - 1 < 0$, so that $\eta_0 = \pm 1$ are both locally energetically favored over the interceding fragmented states, Eq. (3.29). The central conclusion is not affected by this change: energetically stable fragmentation does not occur in 3D harmonic potentials for either model.

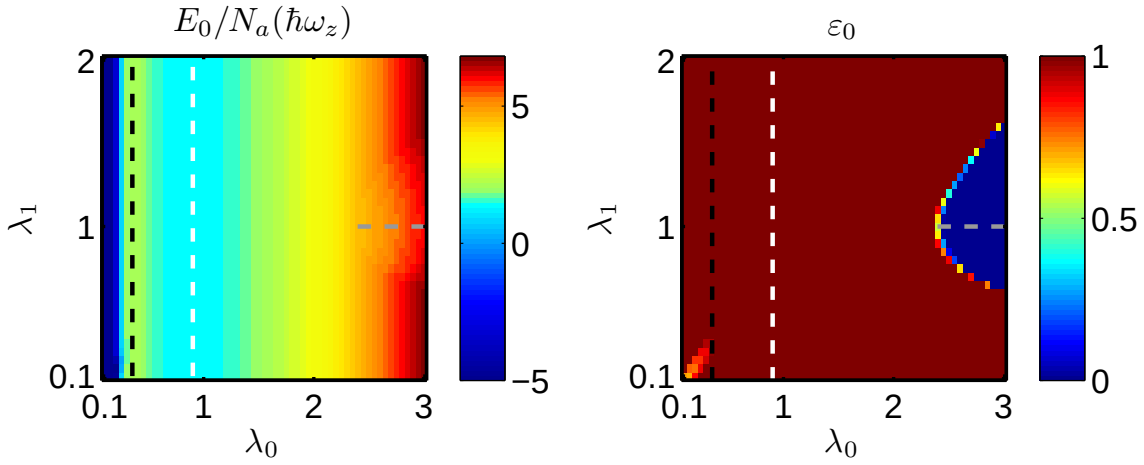

(a) (b)

Figure 3.9: Many-body ground state energy and fragmentation landscapes for $N_a = 950 = 0.96N_c$ atoms scattering amongst single-particle variationally-widthed 3D trap states 0 and 1, scaled by λ_0 and λ_1, respectively. (a) E_0/N_a vs (λ_0, λ_1). Unlike in 1D, Fig. 3.8(a), in 3D there are no points that are energy local minima with respect to both variational parameters simultaneously. Instead the energy local minimum at $\lambda_0 = 0.9 \pm 0.025$ where $E_0/N_a = 1.3\,\hbar\omega$, marked with a white vertical dashed line, is a minimum with respect to λ_0 only. It has no λ_1 dependence because in that region $\langle \hat{n}_1 \rangle = 0$. Likewise, the black vertical dashed line at $\lambda_0 = 0.35 \pm 0.025$ marks an energy local maximum that is similarly independent of λ_1. To the left the energy per particle rapidly diverges to negative infinity so that systems left of this line runaway further left, corresponding to collapse. Systems right of the maximum propagate right, into the white dashed line energy basin. The height of this maximum depends on N_a, shrinking with increasing N_a and disappearing entirely for $N_a \geq N_c$. The grey horizontal dashed line at $\lambda_1 = 1$ for $\lambda_0 \gtrsim 2.4$ marks where the energy is minimized with respect to λ_1 only; the λ_0 dependence here pushes such systems to the left. Unlike in Fig. 3.8(a), the minima occurring at $\lambda_0 \approx 1$ indicates that increasing N_m will not change this result by much. (b) ε_0 vs (λ_0, λ_1), overlaid with the energy minima and maxima identified in (a). Most of the parameter space has a pure ground state: the atoms macroscopically occupy only single-particle trap state 0 (dark red) or single-particle trap state 1 (dark blue), whichever has lower energy. In both regions where fragmentation occurs (other colors), it occurs unstably. Systems in the right fragmented region energetically favor moving left into the white dashed line energy basin. Fragmented systems in the lower left are left of the black vertical line energy maximum so energetically favor continuing left, corresponding to systems that fragment as they collapse. Therefore, stable fragmented ground states do not exist in 3D harmonic potentials for our model.

minimum with respect to λ_0 only. This is a true local minimum with no λ_1 dependence because in this region $\langle \hat{n}_1 \rangle = 0$. That it occurs at $\lambda_0 \approx 1$ indicates that increasing N_m will not substantially change this result. The gray horizontal dashed line marks where the energy is minimized with respect to λ_1 only, however the λ_0 dependence pushes systems here left toward the white dashed line local minimum. The black vertical dashed line marks a local energy maximum with respect to λ_0 only, again without λ_1 dependence because $\langle \hat{n}_1 \rangle = 0$. To its left the self-attraction is so strong that systems here propagate further left, corresponding to collapse. Systems to the right tend back toward the white dashed line energy minimum. The height of this maximum depends on N_a, shrinking with increasing N_a and disappearing entirely for $N_\mathrm{a} \geq N_\mathrm{c}$. The fragmentation landscape in Fig. 3.9(b) shows that the ground state is pure over most of the parameter space, with the N_a atoms macroscopically occupying only single-particle state 0 (dark red) or single-particle state 1 (dark blue), whichever has lower energy at the particular (λ_0, λ_1). There are two regions where this is not the case and fragmentation occurs (other colors). On the right, immediately between the dark red and dark blue regions, h_{00} and h_{11} so closely match that both become macroscopically occupied. However the energy dependence on λ_0 here forces these systems to propagate left toward the white dashed line minima, meaning this fragmentation is transitory. The fragmentation region in the lower left is left of the energy maximum and corresponds to collapsing systems that energetically favor fragmentation during collapse. In all cases our models predict that energetically stable fragmented states do not form in attractively interacting particles in 3D harmonic potentials.

1D harmonic trap states 0 and 2

Applying our two single-particle state model instead to the 1D ground and second excited trap states, which have even-relative parity, predicts a pure many-body ground state. Shown in Fig. 3.10(a), the ground state energy landscape of this system has two local minima, both of which correspond to pure states, as shown in Fig. 3.10(b), and both of which have lower energy per particle than the fragmented many-body ground state formed between the ground and first excited state pair. So when both are allowed, as in our experiment where the Hilbert space is not truncated, the pure ground state will be energetically preferred over the fragmented state. As in Fig. 3.8(a), both $\lambda_i \ll 1$ signifies that modeling with $N_\mathrm{m} > 2$

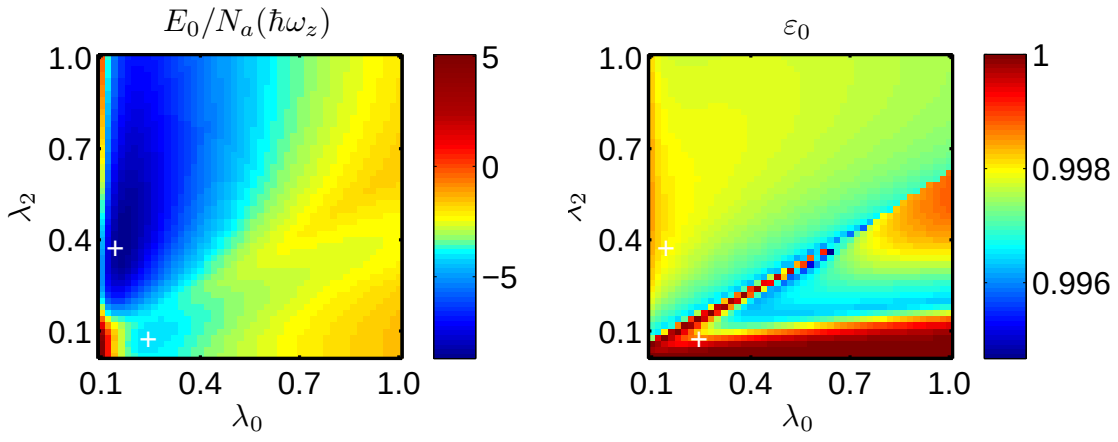

(a) (b)

Figure 3.10: Many-body ground state energy and fragmentation landscapes for $N_\mathrm{a} = 307 = 0.85N_\mathrm{c}$ atoms scattering amongst single-particle variationally-widthed 1D trap states 0 and 2, scaled by λ_0 and λ_2, respectively. (a) E_0/N_a vs (λ_0, λ_2). The local minima (white +) at $(\lambda_0, \lambda_2) = (0.16{\pm}0.01, 0.38{\pm}0.01)$ where $E_0/N_\mathrm{a} = -8.7\,\hbar\omega_z$, and at $(0.26{\pm}0.01, 0.08{\pm}0.01)$ where $E_0/N_\mathrm{a} = -4.2\,\hbar\omega_z$, represent ground states that are stable against small fluctuations in single-particle state widths and occupation number. The former is the global ground state for this N_a and trap state pair. Both have lower energy per particle than at the energy minimum for scattering between trap states 0 and 1, Fig. 3.8(a), the latter having slightly less and the former significantly less. Similar to Fig. 3.8(a), $\lambda_0, \lambda_2 \ll 1$ indicates that increasing $N_\mathrm{m} > 2$ would substantially change the nominal width ground state results. (b) ε_0 vs (λ_0, λ_2), overlaid with the energy minima identified in (a). Unlike scattering between 1D trap states 0 and 1, Fig. 3.8(b), this entire parameter space has a pure ground state, $\varepsilon_0 \sim O(1)$, $\varepsilon_1 = 1 - \varepsilon_0 \sim O(N_\mathrm{a}^{-1})$, including both minima.

would significantly improve the ground state results compared achieved using nominally-widthed single particle state modeling.

3.3.5 Role of state pair relative parity in 1D harmonic potentials

Each of these analyses reveals that for 1D systems within our model, where in general fragmentation can occur, the single-particle state pair relative parity plays a major role in determining whether fragmentation will occur at high N_a or not. Excepting odd-relative parity state pairs with insufficient overlap such that they do not fragment, odd-relative parity single-particle state pairs tend toward fragmented ground states at high N_a, and even-relative parity single-particle state pairs have pure ground states for all N_a. This appears directly in the SPDM eigenvalues of the nominally-widthed state pairs, which remain fixed at 0 and 1 for even-relative parity and converge between them for odd-relative parity of sufficient overlap, Sec. 3.3.1. It appears in the semiclassical N_f formula itself, Eg. (3.28), which has a relatively simple form for odd-relative parity because one energy dependency is trivially minimized in Eg. (3.23), but does not exist for any even-relative parity cases we considered. The signature in the excitation energies, Sec. 3.3.3, is an additional spectral feature of pairwise degeneracies for $N_a \gg 1$ in state pairs with odd-relative parity and sufficient overlap that is not present in even-relative parity state pairs. This also carried through into the variationally widthed ground states, with a fragmented ground state for scattering between variationally-widthed trap states 0 and 1 and a pure ground state for scattering between variationally-widthed trap states 0 and 2.

3.4 Summary

We theoretically explored a hypothesis that could potentially account for the irregular cold cloud density profiles and the frustration of conventional BEC that we observe experimentally. Namely, these might be explainable by our specific combination of attractive interactions and a quasi-1D trap creating a situation wherein the interactions dominate the axial curvature so that the many-body ground state is part of a manifold of nearly degenerate states. To investigate, we used the two-body interaction Hamiltonian to extend the

$N_m = 1$ many-body mean field GP formalism to allow for atom scattering between $N_m = 2$ single-particle trap modes.

With this model we found that many single-particle state energy-adjacent pairs undergo pairwise fragmentation of their many-body ground state for $N_a = N_f < N_c$ for our system parameters. 3-apart, 5-apart, etc. state pairs (odd-relative parity) generally also undergo fragmentation but at $N_f > N_c$ for our system parameters. States with even-relative parity, 2-apart, 4-apart, etc. remain pure at all N_a. This signature appears in the excitation energies as well. State pairs with fragmented ground states include a spectral feature wherein adjacent many-body states pair up and become degenerate much faster than the $\sim O(N_a^{-1})$ typical of mean-field interactions. We ascribed independent variational widths to our two single-particle states to probe what the many-body ground states might look like were we able to simulate with $N_m > 2$, and found that in the 1D cases the energetically favored variational widths were between 0.1 and 0.4, indicating that increasing N_m will change at least the ground state considerably from the $N_m = 2$ nominal width cases. As a check against experiment [3] and generally accepted theory [37], we applied our model to a 3D isotropic harmonic potential and found that it similarly predicted a pure ground state.

The sensitivity to state pair relativity calls into question the relevance of these models to experiments, which probably should be expected given that our data indicate $N_a \sim O(10) \gg 2$. Though less of a problem in our $N_m = 2$ model than in the $N_m = 1$ GP formalism, both are mean-field based, meaning that they neglect high order atom-atom correlation information. It is likely the case that for attractive atoms in a quasi-1D potential, where they can simultaneously have strong interactions relative to the axial confinement and be stable against collapse, that atom-atom correlations are essential to understanding the dynamics. The ability to simulate even $N_m = 4$ models at realistic N_a, so that the atoms could simultaneously scatter between two even parity and two odd parity single particle states, might produce a much different picture of the degeneracies in the excitation spectra, and point to how likely our result is due to the interconnection underlying interaction energy and trap anisotropy.

Chapter 4

Outlook

4.1 Controllable single bright atomic soliton source

With the new understanding of our experimental system enabled by our beyond Gross-Pitaevskii, multi-mode mean-field theory, we next intend to build a controllable robust bright atomic single soliton source. Though not feasible in our quasi-1D magnetic trap alone without Feshbach control, Ref. [3] and our simulations indicate that if we instead evaporated with attractive interactions into a spherical potential we would produce a pure BEC, with only one trap state macroscopically occupied. Adiabatically deforming this spherical potential to make it quasi-1D will change this pure BEC into the single soliton ground state of the quasi-1D trap, so long as the characteristic length of the final harmonic potential is much greater than the characteristic soliton length. $N_{\mathrm{a}} < N_{\mathrm{c}}$ for the 3D trap will ensure that it holds for the quasi-1D trap as long as ω_r does not change substantially. We intend to accomplish this by crossing our cigar shaped magnetic trap with a second cigar-shaped red-detuned optical dipole trap, which will add tight confinement to the axial dimension. For fixed focus size and detuning, the overall trap depth and axial frequency will be controlled by the optical trap power, see Fig. 4.1. We think we will be able to use this to control the number of atoms in the final soliton. Finally, the axial position of this optical trap will control where the soliton forms.

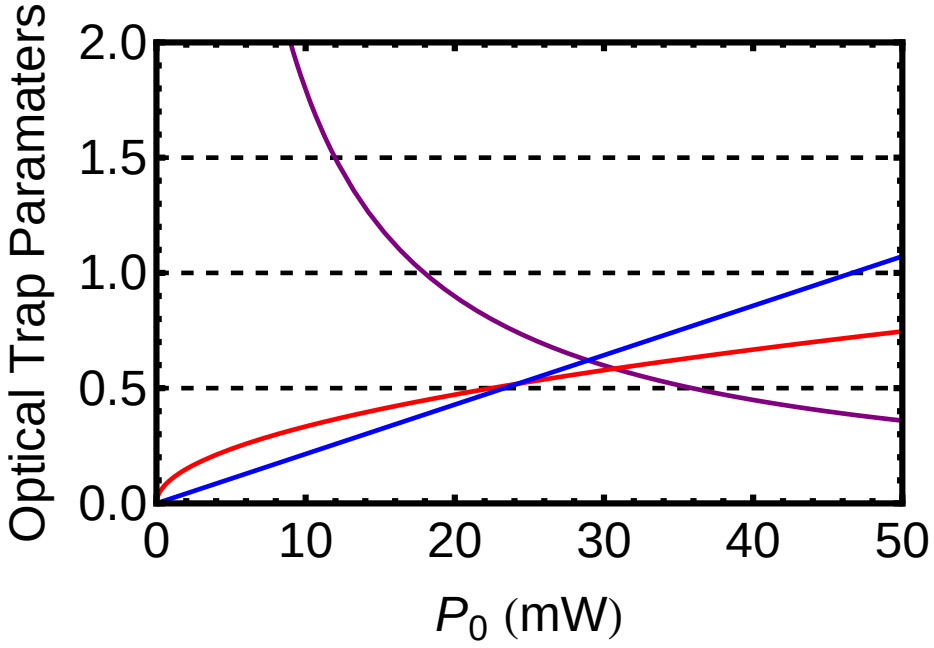

Figure 4.1: Normalized optical trap depth, frequency, and spontaneous emission atom lifetime as a function of total trapping power, for $\lambda = 852\,\text{nm}$ and $23\,\mu\text{m}$ focused spot size. The trap depth (blue line) is normalized to $10\,\mu\text{K}$, which is around the value we would like to achieve. Similarly the trapping frequency (red line) is normalized to $2\pi \times 3.5\,\text{kHz}$, and the optical trap spontaneous emission atom lifetime (purple line) is normalized to 200 s. It looks like we can reasonably simultaneously achieve just over 0.5 in all three normalized parameters. The 852 nm wavelength matches a laser system built up to supply the light for this optical trap. The $23\,\mu\text{m}$ focus size looks reasonable considering the mechanical constraints for optically accessing our vacuum chamber.

4.2 Controllable atomic soliton source experiments and applications

Single bright atomic solitons are well understood quantum mechanical states and with controllable position and N_a they will be ideal input states for many types of follow-on experiments, measurement protocols, and sensor applications. In searching for macroscopic tunneling, experiments we would like to perform are colliding such solitons with thin optical barriers, and raising a repulsive potential underneath such a soliton to observe whether it quantum evaporates off faster than a classical particle could roll off [10]. Both of these are potential routes toward creating a soliton beamsplitter which will enable the creation of soliton-massed Schrödinger's cat states as well as NOON state atom interferometry. Such cat states in our current trap could have $m_{sol} \gtrsim 2000$ amu, already larger than the current most massive object to display wave-particle duality, fluorofullerene $C_{60}F_{48}$ at $\lesssim 1700$ amu [45, 46]. Changing aspect ratio or scattering length may allow us to increase this further. A follow-on benefit to NOON state interferometry with solitons is that interrogation times can be extended until they are limited by three-body losses and background vapor pressure limits on trap lifetime, because for solitons wavepacket dispersion no longer provides this limit. While single bright atomic solitons are well understood, collisions between solitons are not. Creating two such controllable solitons and colliding them, varying N_a and relative momentum, will shed considerable light on the details of this process, and on how well this non-linearity can be harnessed for quantum measurement protocols.

4.3 Tunable coherence length matter-wave source

In optical interferometry the optimal coherence length is application specific and often depends on the noise channels. For example, the dynamic range of displacement measuring Michelson interferometers scales with coherence length, making longer better. Conversely, the vertical resolution of non-contact surface metrology Fizeau interferometers also scales with coherence length, making shorter better. More complicatedly, the signal to noise ratio of fiber optic gyroscope Sagnac interferometers requires an intermediate coherence length, one that optimally balances the competing requirements of low coherence length to

minimize coherent backscatter from waveguide imperfections, to minimize noise, with the long coherence length needed to couple a high flux of photons into the single mode fiber, to maximize the signal.

In analogy with optical interferometers, as commercial atom interferometers become more feasible, application specific optimal coherence properties may develop. At the long coherence length extreme lie pure BECs, analogous to lasers, and at the shortest coherence lengths lie hot thermal clouds, analogous to light bulbs. On the continuum in between, the matter-wave source we report on in Ch. 2 lies at a position analogous to superluminescent diodes (SLDs), with multiple modes macroscopically occupied. Perhaps just as fiber optic gyroscopes today utilize optical SLDs to optimize signal to noise, future portable on-chip atom-optic gyroscopes may similarly benefit from reduced waveguide backscatter by using a bright short coherence length matter-wave source like we have produced [47, 48]. Other applications may require more specific coherence properties, so that the ability to tune the coherence length would prove advantageous. Though our two single-particle state many-body theory is unable to predict anything beyond $N_{\mathrm{m}} = 2$ modes macroscopically occupied, we believe that the trap aspect ratio during evaporation will directly influence the N_{m} in the final quasi-1D density distribution. Because coherence length scales with $N_{\mathrm{m}}^{-1/2}$ [34], and because tuning the optical trap intensity and focused spot size controls the trap aspect ratio during evaporation, we believe this provides a means to create matter-waves with tunable coherence length. Verifying this experimentally will require further matter-wave interference measurements.

Chapter 5

Conclusion

On the road toward observing macroscopic tunneling and producing precision sensors that utilize it, this work has made significant progress toward quantifying and attempting to understand an experimental result in cold atom physics that does not agree with the conventionally accepted theory of Bose-Einstein condensation (BEC) occuring for non-interacting particles at $T < T_c$, the condensation temperature, with modifications to incorporate interparticle interactions given by the mean field Gross-Pitaevskii (GP) formalism. Because BEC is so fundamentally predicated, on statistical mechanics and symmetry under particle exchange, and because mean-field theories, including the GP formalism, in practice work extremely well, the process of BEC formation with and without interparticle interactions is inherently robust, so that our result is novel and unexpected. Specifically, we evaporatively cool attractively interacting bosonic ^{7}Li in a quasi-one dimensional (quasi-1D) trap to demonstrably colder than T_c for our system parameters, as indicated by the cloud widths, but do not observe conventional BEC. Normally, at and below T_c, single mode thermal fits to the density profiles become insufficient and must be replaced by bimodal distributions of the thermal background plus the BEC profile; further cooling is marked by the condensate mode growing while the thermal background mode shrinks, with interactions adjusting the BEC size according to their sign and strength. Instead, throughout cooling we observe nominally single-mode gaussian distributions that become significantly noisier as T decreases and at no point observe the formation of clear regular bimodal structures. At $T \approx T_c$, the cloud number density and phase space density rise above the minimum

required for quantum degeneracy. Also here, we begin observing density profile spikes, indicating that condensation is initiating where predicted, which in turn indicates our T and N_a measurements are probably correct. Though T becomes poorly defined when $|\mu_{int}|$, the absolute value of the interaction energy per particle, $\approx k_B T$, in our evaporation sequences the maximum attainable value of $|\mu_{int}|$ without collapse occurring, $\left|\mu_{int,c}\right|$, equals $k_B T$ at T between a half and a full order of magnitude below T_c. This and the mentioned onset of density spikes substantiate our claim to have cooled to and below T_c. While we are technically unable to ascribe a cardinal temperature around and below this, we observe additional evaporation reduces the axial cloud widths to 1/6 their value at T_c and note that for non-interacting particles this would correspond to $T \approx T_c/30$, implying that our search for bimodal density distributions and conventional BEC extends significantly below T_c.

Taken together, the large axial widths and densities at our coldest evaporation sequences imply the formation of clouds with multiple macroscopically occupied trap states, which appear to be the limit one can reach in our trap. However, though we empirically optimized our evaporation sequence to maximize the non-interacting phase space density at each point in time, we cannot exclude the possibility that the loss mechanisms present in our trap prevent us from evaporating sufficiently slowly to reach equilibrium. Also, the small axial mode spacing, $\hbar\omega_z$, increases our sensitivity to heating and technical noise, which we cannot rule out below $4\,\mathrm{nK/s} \approx 2(\hbar\omega_z/k_B)\,/\mathrm{s}$.

One mechanism that might explain the frustration of conventional BEC and the irregularity of our cold cloud density profiles is that throughout evaporation the measured $|\mu_{int}|$, averaged over each pixel, is several times larger than $\hbar\omega_z$. Moreover, were we able to sample with subpixel resolution axially in addition to radially, GP theory predicts that the maximum allowed value of $|\mu_{int}|$ is more than two orders of magnitude greater than $\hbar\omega_z$ [10]. Thus, the combination of attractive interactions and a quasi-1D trap could create a system wherein the interactions dominate the axial curvature such that the many-body ground state is part of a manifold of nearly degenerate states.

We explored this hypothesis theoretically using the two-body interaction Hamiltonian to extend the single-mode many-body mean field GP formalism to allow for atom scattering between $N_m = 2$ single-particle trap modes. Inputting our experimental parameters and allowing scattering amongst the 1D single-particle ground and first excited trap states,

we found that as N_a increases the many-body ground state smoothly transitions from pure to fragmented for $N_a < N_c$, the critical atom number at which attraction-induced collapse occurs. We demonstrated that the semiclassical approximation closely matches the exact solution for pairs of single-particle states having odd-relative parity, and then used it to show there are many energy-adjacent state pairs (odd-relative parity) that fragment for $N_f = N_a < N_c$ for our experimental parameters. Investigating the exact energy spectra, we showed that for a given single particle state pair with finite N_f, for $N_a \gtrsim N_f$ adjacent pairs of many-body states' per particle excitation energy splitting converges to zero much faster than the $O\left(N_a^{-1}\right)$ typical of mean-field interactions. This indicates a substantial increase in the degree of degeneracy in the many-body spectrum for N_a above N_f, which is predicted to accompany fragmentation [28] and supports our hypothesis for why conventional BECs might not form in our system.

Adding variational widths to our two single-particle states provided an idea of what higher N_m modeling, computationally impracticable at realistic N_a, would predict for the many-body ground state spatial profile and degree of fragmentation. Applied to the 1D harmonic trap ground and first excited state model, it continues to predict a fragmented many-body ground state for $N_a < N_c$, though less so than for nominally-widthed trap states. Applied to the 1D harmonic trap ground and second excited state model, it continues to predict a pure many-body ground state for $N_a < N_c$. In both of these cases $\lambda_i \ll 1$, indicating that higher N_m models will substantially modify the nominally-widthed simulation results. Also essential, for its agreement with experiment [3] and generally accepted theory [37], application to the ground and first excited states of a 3D isotropic harmonic trap predicts a pure (phase-coherent) many-body ground state for all $N_a < N_c$. Our understanding of the degree of degeneracy in the energy spectra for $N_m > 2$ models does not improve by using variational widths because the number of many-body basis states remains unchanged at $N_{HS} = N_a + 1$.

Deeper investigation of 1D $N_m = 2$ single-particle state models reveals their sensitivity to the state pair relative parity: empirically, odd-relative parity single-particle state pairs tend toward fragmented ground states at high N_a, even-relative parity single-particle state pairs have pure ground states for all N_a. Though this sensitivity calls into question their relevance to experiments, where Hilbert space is truncated only by temperature, interactions,

and trap potential, the degree to which such models can predict whether or not experimental quasi-1D system many-body states may reside within manifolds of nearly degenerate states highlights their potential for usefulness.

Finally, mechanism-independent, we will continue seeking to exploit the coherence properties of our current superluminescent bright matter-wave source, characterized by multiple macroscopically occupied modes, as well as those of the single soliton and tunable coherence length bright matter-wave sources that we intend to construct, for probing the boundary of classical and quantum mechanics and for improving atom interferometric sensors.

Appendix A

Gravitational Sag Correction for Evaporation Frequency

Because our quasi-1D Ioffe-Pritchard (IP) trap is oriented with the long, loosely confining dimension vertical, correcting for gravitational sag is more important than if we had tighter vertical confinement. The equations quantifying this effect, in the thesis body Eqs. (2.4) and (2.5), are

$$\Delta\nu_{\mathrm{eff}} = \left(\sqrt{\Delta\nu_{\mathrm{set}} + \Delta\nu_{\mathrm{g}}} - \sqrt{\Delta\nu_{\mathrm{g}}}\right) \tag{A.1}$$

and

$$\Delta\nu_{\mathrm{g}} \equiv \frac{mg^2\left(m_{\mathrm{f}}g_{\mathrm{f}} - m'_{\mathrm{f}}g'_{\mathrm{f}}\right)}{2h\omega_z^2}, \tag{A.2}$$

and are derived in this appendix.

Independent of the presence of gravity, at height z the magnetic field of our IP trap is given by

$$B(z) = B_0 + \frac{m\omega_z^2}{2\mu_{\mathrm{B}}}(z - z_{\mathrm{B0}})^2 \tag{A.3}$$

and the potential energy of a particle in the trap is given by

$$U(z) = \frac{m\omega_z^2}{2}(z - z_{\mathrm{T0}})^2 \tag{A.4}$$

where z_{B0} is the center of the magnetic field and z_{T0} is the center of the trap. In this

formulation, the equations are independent of the choice of $z = 0$.

Whereas without gravity, $z_{\mathrm{B0}} = z_{\mathrm{T0}}$, with gravity the trap center and atoms are displaced below the magnetic field center to $z_{\mathrm{T0}} = z_{\mathrm{B0}} - \Delta z_{\mathrm{g}}$, where

$$\Delta z_{\mathrm{g}} \equiv \frac{|g|}{\omega_z^2} \tag{A.5}$$

and g is the acceleration due to gravity. B at the trap center changes as well, to $B_{\mathrm{T0}} \equiv B(z_{\mathrm{T0}}) = B_0 + \Delta B_g$, where

$$\Delta B_g = \frac{mg^2}{2\mu_{\mathrm{B}}\omega_z^2}. \tag{A.6}$$

At the root of the gravitational sag correction to ν is that B_{T0}, and not B_0, is the magnetic field value that determines ν_0 when it is measured or set with gravity present. Namely,

$$h\left(\nu_0 - \nu_{\mathrm{HFS}}\right) \equiv \left(m_{\mathrm{f}} g_{\mathrm{f}} - m'_{\mathrm{f}} g'_{\mathrm{f}}\right) \mu_{\mathrm{B}} B_{\mathrm{T0}} \tag{A.7}$$

defines ν_0 and B_{T0}. In running the experiment we control $\nu_{\mathrm{set}} = \nu_0 + \Delta\nu_{\mathrm{set}}$ which determines $B_{\mathrm{set}} = B_{\mathrm{T0}} + \Delta B_{\mathrm{set}}$, the value of B at resonance when $\nu = \nu_{\mathrm{set}}$, which in turn determines the positions $z = z_{\mathrm{res}}$ where the resonance condition is met. Using the resonance condition at $\nu_{\mathrm{set}}, B_{\mathrm{set}}$ gives

$$h\left(\Delta\nu_{\mathrm{set}} + \nu_0 - \nu_{\mathrm{HFS}}\right) = \left(m_{\mathrm{f}} g_{\mathrm{f}} - m'_{\mathrm{f}} g'_{\mathrm{f}}\right) \mu_{\mathrm{B}} \left(\Delta B_{\mathrm{set}} + B_{\mathrm{T0}}\right) \tag{A.8}$$

which, using Eq. (A.7), simplifies to

$$h\Delta\nu_{\mathrm{set}} = \left(m_{\mathrm{f}} g_{\mathrm{f}} - m'_{\mathrm{f}} g'_{\mathrm{f}}\right) \mu_{\mathrm{B}} \Delta B_{\mathrm{set}}. \tag{A.9}$$

When we change $\Delta\nu_{\mathrm{set}}$ we physically change the resonant B by ΔB_{set} as given in Eq. (A.9), so that z_{res} is given by

$$\frac{h\Delta\nu_{\mathrm{set}}}{\mu_{\mathrm{B}}\left(m_{\mathrm{f}} g_{\mathrm{f}} - m'_{\mathrm{f}} g'_{\mathrm{f}}\right)} = \Delta B_{\mathrm{set}} = B(z_{\mathrm{res}}) - B_{\mathrm{T0}}. \tag{A.10}$$

Using Eq. (A.3) makes

$$\frac{h\Delta\nu_{\mathrm{set}}}{\mu_{\mathrm{B}}\left(m_{\mathrm{f}}g_{\mathrm{f}}-m'_{\mathrm{f}}g'_{\mathrm{f}}\right)}=\frac{m\omega_z^2}{2\mu_{\mathrm{B}}}\left(z_{\mathrm{res}}-z_{\mathrm{B0}}\right)^2-\frac{m\omega_z^2}{2\mu_{\mathrm{B}}}\left(z_{\mathrm{T0}}-z_{\mathrm{B0}}\right)^2. \tag{A.11}$$

We set $z_{\mathrm{T0}}=0$ so that $U(z_{\mathrm{res}})=m\omega_z^2 z_{\mathrm{res}}^2/2$, which will simplify extracting $\Delta\nu_{\mathrm{eff}}$. In this coordinate system $z_{\mathrm{B0}}=\Delta z_{\mathrm{g}}$, and Eq. (A.11) becomes

$$\frac{h\Delta\nu_{\mathrm{set}}}{\mu_{\mathrm{B}}\left(m_{\mathrm{f}}g_{\mathrm{f}}-m'_{\mathrm{f}}g'_{\mathrm{f}}\right)}=\frac{m\omega_z^2}{2\mu_{\mathrm{B}}}\left(z_{\mathrm{res}}-\Delta z_{\mathrm{g}}\right)^2-\frac{m\omega_z^2}{2\mu_{\mathrm{B}}}\left(0-\Delta z_{\mathrm{g}}\right)^2. \tag{A.12}$$

Solving for z_{res} gives

$$z_{\mathrm{res}}=\Delta z_{\mathrm{g}}-\sqrt{\frac{2h\Delta\nu_{\mathrm{set}}}{m\omega_z^2\left(m_{\mathrm{f}}g_{\mathrm{f}}-m'_{\mathrm{f}}g'_{\mathrm{f}}\right)}+\Delta z_{\mathrm{g}}^2}, \tag{A.13}$$

where we have taken the negative root of the quadratic because gravity makes the atoms preferentially evaporate from the bottom of the trap.

With this coordinate system choice, the atoms evaporating from z_{res} will have trap potential energy

$$U(z_{\mathrm{res}})=\frac{1}{2}m\omega_z^2\left(\Delta z_{\mathrm{g}}-\sqrt{\frac{2h\Delta\nu_{\mathrm{set}}}{m\omega_z^2\left(m_{\mathrm{f}}g_{\mathrm{f}}-m'_{\mathrm{f}}g'_{\mathrm{f}}\right)}+\Delta z_{\mathrm{g}}^2}\right)^2. \tag{A.14}$$

Finally, the effective differential RF relates to the trap potential energy as

$$\begin{aligned}\frac{h\Delta\nu_{\mathrm{eff}}}{\left(m_{\mathrm{f}}g_{\mathrm{f}}-m'_{\mathrm{f}}g'_{\mathrm{f}}\right)} &= U(z_{\mathrm{res}})\\ &= \frac{1}{2}m\omega_z^2\left(\Delta z_{\mathrm{g}}-\sqrt{\frac{2h\Delta\nu_{\mathrm{set}}}{m\omega_z^2\left(m_{\mathrm{f}}g_{\mathrm{f}}-m'_{\mathrm{f}}g'_{\mathrm{f}}\right)}+\Delta z_{\mathrm{g}}^2}\right)^2.\end{aligned} \tag{A.15}$$

Solving for $\Delta\nu_{\rm eff}$ gives

$$\begin{aligned}
\Delta\nu_{\rm eff} &= \frac{m\omega_z^2\left(m_{\rm f}g_{\rm f}-m'_{\rm f}g'_{\rm f}\right)}{2h}\left(\Delta z_{\rm g}-\sqrt{\frac{2h\Delta\nu_{\rm set}}{m\omega_z^2\left(m_{\rm f}g_{\rm f}-m'_{\rm f}g'_{\rm f}\right)}+\Delta z_{\rm g}^2}\right)^2 \\
&= \left(\Delta z_{\rm g}\sqrt{\frac{m\omega_z^2\left(m_{\rm f}g_{\rm f}-m'_{\rm f}g'_{\rm f}\right)}{2h}}-\sqrt{\Delta\nu_{\rm set}+\Delta z_{\rm g}^2\frac{m\omega_z^2\left(m_{\rm f}g_{\rm f}-m'_{\rm f}g'_{\rm f}\right)}{2h}}\right)^2 \\
&= \left(\sqrt{\frac{mg^2\left(m_{\rm f}g_{\rm f}-m'_{\rm f}g'_{\rm f}\right)}{2h\omega_z^2}}-\sqrt{\Delta\nu_{\rm set}+\frac{mg^2\left(m_{\rm f}g_{\rm f}-m'_{\rm f}g'_{\rm f}\right)}{2h\omega_z^2}}\right)^2
\end{aligned} \tag{A.16}$$

Subsituting in Eg. (A.2),

$$\begin{aligned}
\Delta\nu_{\rm eff} &= \left(\sqrt{\Delta\nu_{\rm g}}-\sqrt{\Delta\nu_{\rm set}+\Delta\nu_{\rm g}}\right)^2 \\
&= \left(\sqrt{\Delta\nu_{\rm set}+\Delta\nu_{\rm g}}-\sqrt{\Delta\nu_{\rm g}}\right)^2,
\end{aligned}$$

produces Eq. (A.1), the formula for gravity corrected effective differential RF, $\Delta\nu_{\rm eff}=\nu_{\rm eff}-\nu_0$, as a function of the control differential RF, $\Delta\nu_{\rm set}=\nu_{\rm set}-\nu_0$.

In the large $\Delta\nu_{\rm set}$ limit, where $\Delta\nu_{\rm set}\gg\Delta\nu_{\rm g}$, $f(x)=\left[(1+x)^{1/2}-x^{1/2}\right]^2$ can be Taylor expanded into $f(x)=1+x+O(x^3)$, so that $\Delta\nu_{\rm eff}$ can be expressed as

$$\begin{aligned}
\Delta\nu_{\rm eff} &= \Delta\nu_{\rm set}\left(\sqrt{1+\frac{\Delta\nu_{\rm g}}{\Delta\nu_{\rm set}}}-\sqrt{\frac{\Delta\nu_{\rm g}}{\Delta\nu_{\rm set}}}\right)^2 \\
&= \Delta\nu_{\rm set}\left(1+\frac{\Delta\nu_{\rm g}}{\Delta\nu_{\rm set}}+O\left(\frac{\Delta\nu_{\rm g}}{\Delta\nu_{\rm set}}\right)^3\right) \\
&\approx \Delta\nu_{\rm set}+\Delta\nu_{\rm g}.
\end{aligned} \tag{A.17}$$

In the small $\Delta\nu_{\rm set}$ limit, where $\Delta\nu_{\rm set}\ll\Delta\nu_{\rm g}$, $f(x)=\left[(1+x)^{1/2}-1\right]^2$ can be Taylor

expanded into $f(x) = x^2/4 + O(x^3)$, so that $\Delta\nu_{\rm eff}$ can be expressed as

$$\begin{aligned}
\Delta\nu_{\rm eff} &= \Delta\nu_{\rm g}\left(\sqrt{1+\frac{\Delta\nu_{\rm set}}{\Delta\nu_{\rm g}}}-1\right)^2 \\
&= \Delta\nu_{\rm g}\left(\frac{1}{4}\left(\frac{\Delta\nu_{\rm set}}{\Delta\nu_{\rm g}}\right)^2+O\left(\frac{\Delta\nu_{\rm set}}{\Delta\nu_{\rm g}}\right)^3\right) \\
&\approx \frac{\Delta\nu_{\rm set}^2}{4\Delta\nu_{\rm g}}. \qquad \text{(A.18)}
\end{aligned}$$

Appendix B

Image Processing and Atom Number Calculation

This document was originally titled 'Cold lithium experiment atom number calculation'. I originally wrote it on April 8, 2009, and made minor changes when including it in this thesis.

Much of this process was implemented before Mike and I became senior grad students on the experiment. Many parts can be done more efficiently, but here is how they were done when we originally took this data.

I. Get OD images (these, in false color, are the images we display in our data booklets) from raw images.

1. For each OD image we take 4 actual pictures, each of which is stored as a 2D array of counts occurring at each pixel:

(a) With atoms, imaging light on, starting after 200 us of the atom cloud expanding ballistically.

(b) Without atoms, imaging light on, taken 600 ms after (a).

(c) Without atoms, imaging light off, to get the dark counts on the camera near the time of images (a) and (b), taken 750 ms after (b).

(d) Without atoms, imaging light off, a second dark counts image, taken 600 ms after (c).

2. Subtract dark counts. All light is turned off for each of images (c) and (d), so we first average the counts and subtract the mean from each image

$$\begin{aligned} \text{withAtoms} &= (a) - \text{mean}(c), \\ \text{withoutAtoms} &= (b) - \text{mean}(d). \end{aligned} \tag{B.1}$$

3. Even after subtracting the dark counts, there remains a systematic difference in background average intensity between these pictures which we can see by looking where we expect there are no atoms (usually within a few percent, rarely above 5%). We calculate this value, intensityScalar, with a least squares fit on part of the image without atoms ("intens" refers to a subset of pixels where we expect no atoms to abide), such that we minimize

$$\text{intensityScalar} \times \text{withAtomsIntens} - \text{withoutAtomsIntens}. \tag{B.2}$$

4. Use intensityScalar to rescale the pixel counts of the image matrix with atoms, which we subtract from the image without atoms to get a map of pixel counts that each are proportional to the number of absorbed photons. The absorption image is created pixel by pixel by dividing the number of photons absorbed by the total number of photons counted when atoms were not present:

$$\text{absorption} = \frac{\text{withoutAtoms} - \text{intensityScalar} \times \text{withAtoms}}{\text{withoutAtoms}'}. \tag{B.3}$$

withoutAtoms′ is nearly the same as withoutAtoms, but to eliminate the problems caused by dividing by 0, or numbers close to it, any value that is less than or equal to 0 is changed to 0.01.

5. Absorption values above 0.999 are set to 0.999.

6. Convert to OD images. For historical reasons, the image analysis program that generated the images and derived values that we sent you, displays the OD*100.

$$\text{OD} = -100 \log(1 - \text{absorption}). \tag{B.4}$$

II. Calculate the atom number

We calculate the atom number by fitting a gaussian to the density profile and calculating the atom number associated with that gaussian. For this data set we did two 1D fits, one for the vertical profile and one for the horizontal profile. (Since the original analysis we have also implemented an algorithm to enable true 2D fits, but that was not used in this analysis).

1. Zoom OD image to region around atoms. We try to make the region large enough to allow us to determine the linear background slope, vertically and horizontally. Along the top we sometimes get fringing caused by the shutter that coarsely controls the imaging light, so we try to minimize this by cropping close to the cloud center when necessary.

2. Pick the center pixel. This pixel determines the column and the row of pixels' ODs that will be fitted.

3. We fit a gaussian to the column of pixels that contain the center pixel, of the form

$$\text{OD}(z) = \text{OD}_{\text{pk}} \exp\left(-\frac{(z - z_c)^2}{2\sigma_z^2}\right) + \text{OD}_{\text{offset}} + \text{OD}_{\text{slope}}(z - z_c), \tag{B.5}$$

where z is in units of mm ($z_\ell = \ell\Delta_{\text{pix}}$, where Δ_{pix} is the length or width of one pixel); σ_z, or "Ver size" in the data booklet pages, is the width (mm); OD_{pk}, or "Ver peak" in the data booklet pages, is the peak OD (*100); z_c, or "Ver Center" in the data booklet pages, is the center position (mm); $\text{OD}_{\text{offset}}$ is the offset (OD*100), not recorded in the data booklets;

and OD_{slope} is the slope (OD*100/mm), also not recorded in the data booklets. This is the axial fit.

To get the radial fit parameters, we fit a gaussian of the same form to an averaged horizontal row of pixels. This averaged pixel row includes the central row and all of the ±10 rows having integrated atom signal, summed pixel by pixel, 10% or higher than that of the central row. This is done to improve the signal to noise ratio because otherwise in any single radial cross section relatively few pixels have useful atom signal.

4. Calculate the atom number:

$$N_{\mathrm{a}} = \frac{\mathrm{OD}_{\mathrm{pk}}}{100\alpha_0} 2\pi\sigma_z\sigma_r, \tag{B.6}$$

where α_0 is the atom-light scattering cross-section.

$$\alpha_0 = 3f_p\frac{\lambda^2}{(2\pi)}, \tag{B.7}$$

where $\lambda = 671$ nm is the wavelength of resonant light, the 3 is for light that is perfectly σ_+ polarized relative to atoms in the $F = 2, m_F = 2$ hyperfine ground state level, and $f_{\mathrm{p}} = 0.7$ is a dimensionless number determined from the steady state solution of the population distribution of atoms amongst the ground state hyperfine levels for the light field polarization, detuning, and intensity, and DC magnetic field strength during imaging. We use $f_p = 0.7$ which we calculated by simulating the steady state hyperfine ground state populations under the magnetic and light fields during imaging. The important thing is that the maximum value it can have is 1, meaning that at worst this could cause our atom calculation to be too high by 50%. There is also a chance that 0.7 overestimates f_p and our reported atom number is actually low. This number is called "TOF Natom" in our cloud image data booklet pages.

In the atom number calculation we use the OD_{pk} taken from the vertical fit because it is determined from fitting over many more pixels than that for the horizontal fit. Most of the time both values are close but not always. One easy way for them to differ is if the pixel with highest OD is different from the selected center pixel. (The true 2D fits eliminate this

problem, but are not used here.)

The other major potential source of error is the length and width subtended by each pixel in the plane of the atoms. The size of the pixels is listed in the camera manufacturer's specification as $8\,\mu$m by $8\,\mu$m (Andor iXon DV885). We 2x2 bin using the camera software at the time the images are taken and the .sif image files are saved. This 2x2 binning is recorded in the image files at the time that they are created and gives us an effective pixel size of $16\,\mu$m by $16\,\mu$m. Finally, we get the magnification from the ratio of the manufacturer's specified focal lengths of the lenses of our imaging telescope 250 mm/90 mm, making the effective pixel length and width in the atom plane:

$$\Delta_{\text{pix}} = 16\,\mu\text{m} \times \frac{90\,\text{mm}}{250\,\text{mm}} \approx 5.8\,\mu\text{m}, \tag{B.8}$$

I verified the magnification this evening by comparing the size of a collimated gaussian beam before and after the imaging system at $\approx 2\,\text{mm}/6\,\text{mm} = 3$, which matches $25/9 \approx 2.8$ well within the uncertainty.

To check that the fit itself is not causing us problems, we instituted a sanity check whereby we sum up the atoms pixel by pixel for all pixels within the fitted exp(−2) density radius. To account for the $\approx 9\%$ of atoms outside this radius, we divide the sum by $\text{erf}(2^{1/2})$. This quantity is called "Ntotbypx" in the data booklets and can be compared with "TOF Natom". For images where the entire cloud is on the screen, "Ntotbypx" seems to normally be $5 - 10\%$ higher than "TOF Natom" which is probably because the algorithm rounds in such a way as to tend to include pixels that are borderline being within the exp(−2) density radius.

As a final sanity check on the numerics, I calculated OD_{pk} of 9_14_06_8042_1_1.sif by hand (averaged over the 8 central-most pixels) and got a value of 52.3, which closely matches "Ver peak" = 51.9. Then, using the fitted values of "Ver peak", "Ver size", "Hor size", and the calculated value of α_0, I calculated $N_{\text{a}} = 8491$, which closely matches "TOF Natom" = 8490.

Bibliography

[1] M. H. Anderson, J. R. Ensher, M. R. Matthews, C. E. Wieman, and E. A. Cornell. Observation of Bose-Einstein condensation in a dilute atomic vapor. *Science*, 269(0):198, July 1995.

[2] K. B. Davis, M.-O. Mewes, M. R. Andrews, N. J. van Druten, D. S. Durfee, D. M. Kurn, and W. Ketterle. Bose-Einstein condensation in a gas of sodium atoms. *Phys. Rev. Lett.*, 75(22):3969, November 1995.

[3] C. C. Bradley, C. A. Sackett, J. J. Tollett, and R. G. Hulet. Evidence of Bose-Einstein condensation in an atomic gas with attractive interactions. *Phys. Rev. Lett.*, 75(9):1687, August 1995. *ibid.* **79**, 1170 (1997).

[4] A. Einstein. Quantentheorie des einatomigen idealen Gases. Zweite Abhandlung. *Sitzungber. Preuss. Akad. Wiss.*, 1925:3, January 1925.

[5] Satyendra Bose. Plancks Gesetz und Lichtquantenhypothese. *Z. Phys.*, 26(3):178, 1924.

[6] F. Reif. *Fundamentals of Statistical and Thermal Physics*. McGraw Hill, 1965.

[7] C. J. Pethick and H. Smith. *Bose-Einstein Condensation in Dilute Gases*. Cambridge University Press, 2001.

[8] P. A. Ruprecht, M. J. Holland, K. Burnett, and Mark Edwards. Time-dependent solution of the nonlinear Schrödinger equation for Bose-condensed trapped neutral atoms. *Phys. Rev. A*, 51(6):4704, June 1995.

[9] M. Houbiers and H. T. C. Stoof. Stability of Bose condensed atomic ^{7}Li. *Phys. Rev. A*, 54(6):5055, December 1996.

[10] L. D. Carr and Y. Castin. Dynamics of a matter-wave bright soliton in an expulsive potential. *Phys. Rev. A*, 66(6):063602, December 2002.

[11] L. Khaykovich, F. Schreck, G. Ferrari, T. Bourdel, J. Cubizolles, L. D. Carr, Y. Castin, and C. Salomon. Formation of a matter-wave bright soliton. *Science*, 296(5571):1290, May 2002.

[12] Kevin E. Strecker, Guthrie B. Partridge, Andrew G. Truscott, and Randall G. Hulet. Formation and propagation of matter-wave soliton trains. *Nature*, 417:150, May 2002.

[13] S. L. Cornish, S. T. Thompson, and C. E Wieman. Formation of bright matter-wave solitons during the collapse of attractive bose-einstein condensates. *Phys. Rev. Lett.*, 96:170401, April 2006.

[14] J. Jacobson, G. Björk, I. Chuang, and Y. Yamamoto. Photonic de Broglie waves. *Phys. Rev. Lett.*, 74(24):4835–4838, 1995.

[15] E. R. I. Abraham, W. I. McAlexander, C. A. Sackett, and Randall G. Hulet. Spectroscopic determination of the s-wave scattering length of lithium. *Phys. Rev. Lett.*, 74(8):1315, February 1995.

[16] Ruquan Wang, Mingchang Liu, Francesco Minardi, and Mark Kasevich. Reaching ^{7}Li quantum degeneracy with a minitrap. *Phys. Rev. A*, 75:013610, January 2007.

[17] J. Walls, R. Ashby, JJ Clarke, B. Lu, and WA Van Wijngaarden. Measurement of isotope shifts, fine and hyperfine structure splittings of the lithium D lines. *Eur. Phys. J. D*, 22(2):159–162, 2003.

[18] W. Ketterle, DS Durfee, and DM Stamper-Kurn. Making, probing and understanding Bose-Einstein condensates. In *Proceedings of the International School of Physics-Enrico Fermi*, page 67, 1999.

[19] Peter Van der Straten Harold J. Metcalf. *Laser Cooling and Trapping*. Springer, 1999.

[20] A. E. Siegman. *Lasers*. University Science Books, 1986.

[21] M.-O. Mewes, M. R. Andrews, N. J. van Druten, D. M. Kurn, D. S. Durfee, and W. Ketterle. Bose-Einstein condensation in a tightly confining dc magnetic trap. *Phys. Rev. Lett.*, 77(3):416, July 1996.

[22] Y. Castin and C. Herzog. Bose–Einstein condensates in symmetry breaking states. *C. R. Hebd. Seances Acad. Sci., Ser. A B, Sci. Math. Sci. Phys.*, 2(3):419–443, 2001.

[23] Robert B. Laughlin. Atom Cloud Width Notes. NCC, 2010-07-21: Integrals $\langle V_2 \rangle$ and $\langle V_2 \rangle_{\|}$ each have an extra factor of 1/2, e.g. as compared to Ref. [10], perhaps due to a different mass definition, April 2009.

[24] Wolfgang Ketterle and N. J. van Druten. Bose-Einstein condensation of a finite number of particles trapped in one or three dimenstions. *Phys. Rev. A*, 54(1):656, July 1996.

[25] Elizabeth A. Donley, Neil R. Claussen, Simon L. Cornish, Jacob L. Roberts, Eric A. Cornell, and Carl E. Wieman. Dynamics of collapsing and exploding Bose-Einstein condensates. *Nature*, 412(6844):295, July 2001.

[26] N. J. van Druten and Wolfgang Ketterle. Two-step condensation of the ideal Bose gas in highly anisotropic traps. *Phys. Rev. Lett.*, 79(4):549, July 1997.

[27] J.B. McGuire. Study of exactly soluble one-dimensional n-body problems. *J Math Phys*, 5(5):622, May 1964.

[28] E.J. Mueller, T.L. Ho, M. Ueda, and G. Baym. Fragmentation of Bose-Einstein condensates. *Phys. Rev. A*, 74(3):33612, 2006.

[29] F. Calogero and A. Degasperis. Comparison between the exact and Hartree solutions of a one-dimensional many-body problem. *Phys. Rev. A*, 11(1):265–2699, 1975.

[30] L. Salasnich. Beyond mean-field theory for attractive bosons under transverse harmonic confinement. *J Phys B*, 39(7):1743–1750, 2006.

[31] L. Salasnich, A. Parola, and L. Reatto. Condensate bright solitons under transverse confinement. *Phys. Rev. A*, 66(4):043603, Oct 2002.

[32] V.A. Yurovsky, M. Olshanii, and D.S. Weiss. Collisions, correlations, and integrability in atom waveguides. *Adv. At. Mol. Opt Phys*, 55:61–138, 2008.

[33] Subhasis Sinha, Alexander Yu. Cherny, Dmitry Kovrizhin, and Joachim Brand. Friction and diffusion of matter-wave bright solitons. *Phys. Rev. Lett.*, 96(3):030406, Jan 2006.

[34] G.B. Jo, J.H. Choi, CA Christensen, Y.R. Lee, TA Pasquini, W. Ketterle, and DE Pritchard. Matter-wave interferometry with phase fluctuating Bose-Einstein condensates. *Phys. Rev. Lett.*, 99(24):240406, 2007.

[35] P. Nozières and D. Saint James. Particle vs. pair condensation in attractive Bose liquids. *J. Phys.*, 43(7):1133, July 1982.

[36] P. Noziéres. Some comments on Bose-Einstein condensation. In A. Griffin, DW Snoke, and S. Stringari, editors, *Bose-Einstein Condensation*, pages 15–30. Cambridge Univ Pr, 1996.

[37] Ø. Elgarøy and C. J. Pethick. Absence of fragmentation of the condensate in a model for bosons in a trap. *Phys. Rev. A*, 59:1711, February 1999.

[38] Lorenz S. Cederbaum, Alexej I. Streltsov, and Ofir E. Alon. Fragmented metastable states exist in an attractive Bose-Einstein condensate for atom numbers well above the critical number of the Gross-Pitaevskii theory. *Phys. Rev. Lett.*, 100:040402, January 2008.

[39] O.E. Alon and L.S. Cederbaum. Pathway from condensation via fragmentation to fermionization of cold bosonic systems. *Phys. Rev. Lett.*, 95(14):140402, 2005.

[40] A. I. Streltsov, O. E. Alon, and L. S. Cederbaum. Formation and dynamics of many-boson fragmented states in one-dimensional attractive ultracold gases. *Phys. Rev. Lett.*, 100:130401, April 2008.

[41] O. Penrose and L. Onsager. Bose-Einstein condensation and liquid helium. *Phys. Rev.*, 104:576, November 1956.

[42] H. J. Lipkin, N. Meshkov, and A. J. Glick. Validity of many-body approximation methods for a solvable model : (i). exact solutions and perturbation theory. *Nucl. Phys.*, 62(2):188 –198, 1965.

[43] E.C. Titchmarsh. Some integrals involving Hermite polynomials. *Journal London Math. Soc.*, 1(1):15, 1948.

[44] I.W. Busbridge. Some integrals involving Hermite polynomials. *Journal London Math. Soc.*, 1(2):135, 1948.

[45] L. Hackermüller, S. Uttenthaler, K. Hornberger, E. Reiger, B. Brezger, A. Zeilinger, and M. Arndt. Wave nature of biomolecules and fluorofullerenes. *Phys. Rev. Lett.*, 91(9):90408.

[46] K. Hornberger, S. Gerlich, H. Ulbricht, L. Hackermüller, S. Nimmrichter, I.V. Goldt, O. Boltalina, and M. Arndt. Theory and experimental verification of Kapitza–Dirac–Talbot–Lau interferometry. *New Journal of Physics*, 11:043032, 2009.

[47] H.C. Lefevre, R.A. Bergh, and H.J. Shaw. All-fiber gyroscope with inertial-navigation short-term sensitivity. *Opt. Lett.*, 7(9):454–456, 1982.

[48] AE Leanhardt, AP Chikkatur, D. Kielpinski, Y. Shin, TL Gustavson, W. Ketterle, and DE Pritchard. Propagation of Bose-Einstein condensates in a magnetic waveguide. *Phys. Rev. Lett.*, 89(4):40401, 2002.